MAGNETOLIPOSOMES:
Effect of nanoparticles spatial distribution

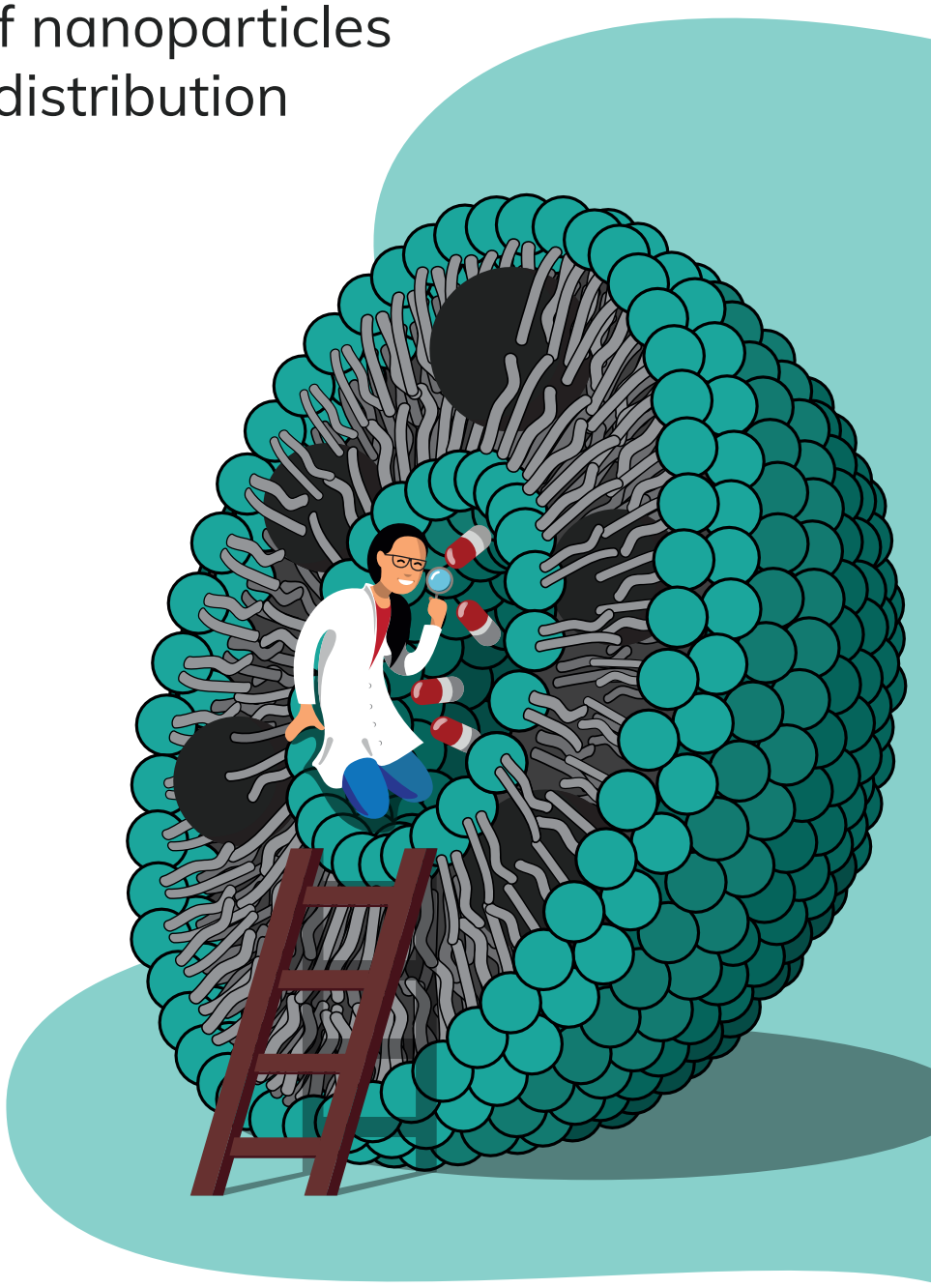

Maria Eugênia Fortes Brollo

Universidad Autónoma de Madrid

CSIC
Consejo Superior de Investigaciones Científicas

Magnetoliposomes: effect of nanoparticles spatial distribution

A thesis submitted for the degree of Doctor of Philosophy at the Universidad Autónoma de Madrid, within the doctoral program in condensed matter physics, nanoscience and biophysics

Maria Eugênia Fortes Brollo

Supervisor: María del Puerto Morales Herrero

Tutor: Pilar Herrasti González

Instituto de Ciencia de Materiales de Madrid

July 2019

"I would rather have questions that can't be answered than answers that can't be questioned." Richard P. Feynman

"Eventually even time will die." G. Franzmann

Acknowledgements

Quero agradecer primeiro aos meus pais que sempre fizeram de tudo para que eu tivesse o melhor. Obrigada mãe por se preocupar e insistir em sair do interior porque ali eu não teria como ir pra faculdade, mesmo que você ainda estivesse grávida. Pai obrigada pelas aulas de cálculo e integral quando eu ainda tinha 10 anos, certamente isso influenciou as minhas escolhas. Obrigada por todos os esforços e sacrificios, só me tornei a pessoa que sou hoje pelo exemplo que tive dentro de casa e por isso serei eternamente grata. Amo vocês.

Obrigada a minha familia que apesar de todos os pesares me ensinaram muito e sempre estiveram do meu lado, um dia espero que ainda possamos rir de todas essas brigas. Josi, obrigada por ter se unido a essa familia Buscapé.

Aos meus amigos que estão espalhados no mundo: saudades define! Mari, Guilherme, Luan, Juca, Gustavo, Iberê, Jéssica, Rennan, Bruno, Juan, Victor, vocês foram e são partes importantes de mim, queria um dia poder ter vocês pertinho novamente em algum cantinho desse mundo. Cada um sabe a importância que tem na minha vida e sem alguns de vocês eu não estaria aqui hoje. Não tenho palavras pra descrever o amor que eu sinto por vocês, espero que daqui 30 anos continuem do meu lado.

Muraca infinitas veces gracias! Aprendí tantas cosas de la vida, del universo y claro, de la ciencia contigo, tienes un sitio especial en mi

corazón, te admiro por la persona que eres.

Ao Marcelo, obrigada! Não estaria aqui em Madrid sem a tua ajuda, eres um dos cientistas mais influentes da minha carreira, admiro o teu caracter e a tua forma de ver a ciencia.

Héctor, eres una de las mejores personas que he conocido, te quiero mucho, me has enseñado tantas cosas que no puedo llegar a describir la importancia que has tenido en esos 3 años, Madrid y la tesis no hubieran sido las mismas sin ti. Gracias por tu compañia y por tu amor.

A la familia Pascual gracias por haber recibido con amor a una brasileña que no le gusta el marisco. Mi vida aqui no seria la misma, sois mi familia y os quiero mucho y ahora más con Julia!

Quiero agradecer a todas las personas que han pasado por mi vida en esos 3 años en España, sois los mejores! Yure y Helena mis mayores confidentes en el ICMM, Eva, Ana, Marzia, Rocio, Nieves, Maria Jesus, Francesca, Raquel, Ana, Belén, Sariña, Isabel, Virginia, Sandra, Cristina, Susel, sois mujeres fuertes y increíbles, he aprendido mucho con vosotras, gracias por poder compartir esos años con mujeres cientificas, saliendo del mundo de la física siempre comandado por tantos hombres. Claro que Juan, Mario, Hugo, Alfonso, Vicente, Oscar, Jose, Nico, Antonio, Alvaro y César también estáis en mi corazón, no os preocupéis chavales también os quiero.

Gracias a ese grupo de amigos de Héctor que me ha acojido en el inicio, habéis hecho que mis fines de semana fueran mejores y mas divertidos, gracias por todas las cenas, comidas, cervezas, vinos, karaokes y fiestas.

Mis amigos de Bilbao, gracias! Vosotros me habéis enseñado mucho de la cultura y del idioma. Llegué sin saber nada, sin conocer a nadie, me habéis acojido de primera y me hicieron sentir parte de una familia, os quiero mucho y tengo recuerdos muy tiernos de esos primeros meses. (Kétchup eso es para ti también).

Querría agradecer también a todos los integrantes del teatro IKKM

y a los del Coro Cantoblanco, que me hicieron sentir bienvenida desde el primer día, gracias a todas y todos.

Gracias a Marisa por todos los ratitos de charlas en el pasillo del ICMM, eres una parte muy importante de este instituto.

Agradecer también a todos los técnicos y personal de la administración del ICMM, sois parte de esta tesis.

Sabino, Lucia, Conchi, Serna, Teresita y Pilar, sin vosotros esta tesis no tendría sentido, aprendí lecciones importantísimas con vosotros y con todo el bagage de conocimiento que tenéis. Gracias por dejarme aprender tantas cosas a vuestro lado.

Tack så mycket Christher, Fredrik, Gert, Pontus, Christian! Thank you for sharing your time and knowledge with me, I have very nice memories of the short time I spent with you in Göteborg.

Gracias a todos los colaboradores que a lo largo de esos años han contribuido para que esta tesis se haga realidad: Xerardo, Vicente, Angeles, Andrea, Fernando, Juan, Marco, Paco, Domingo, Patricia, Christer, Fredrick, Conchi y Ana.

Claro, agradecer a la persona más importante de esta tesis, mi querida directora Puerto. Eres mi inspiración en la ciencia y como persona, me encanta la manera como ves el mundo. Me has enseñado tantas cosas que sólo leyendo la tesis se comprende el esfuerzo que has hecho por mi. Si la tengo escrita es en gran parte por ti y por el conocimiento compartido conmigo y por eso te la dedico. Gracias por fiarte de mi cuando llegué sin saber nada y hablando un español de pena, gracias por todas las veces que me has ayudado tanto en la vida personal como en la profesional. Eres una mujer increíble y te tendré como ejemplo en mi futuro. Gracias!

Obrigada ao CNPq e ao governo brasileiro pela financiação e a possibilidade de realizar essa tese de doutorado.

Contents

Summary

This thesis is focused on the design of nanocarries based on iron oxide nanoparticles and liposomes, that can be loaded with drugs for improving their targeting and efficiency. The combination of these two components represents a unique opportunity for achieving multiple therapeutic objectives.

First of all it was studied the preparation and characterization of uniform iron oxide nanoparticles obtained by microwave assisted synthesis and compared them to those obtained by coprecipitation and thermal decomposition techniques, achieving core sizes from 8 to 15 nm (chapter 4.1). Selected samples were encapsulated in liposomes resulting in different spatial distributions: attached to the liposome surface, inside the lipid bilayer or inside the aqueous volume. Structural and magnetic characterization were also performed (chapter 4.2).

The effect of the aggregation processes on magnetic properties have been analyzed in systems with different spatial distributions of the nanoparticles, as free nanoparticles, magnetoliposomes and cells incubated with nanoparticles (chapter 4.3). Finally, nanoparticles and magnetoliposomes are evaluated *in-vitro* to verify its limits of cytotoxicity in cells and then assessed as negative contrast agents for diagnosis with magnetic resonance imaging, for magnetic hyperthermia treatment and as carriers for doxorubicin, with controlled release by an applied alternate magnetic field in different cell lines (chapter 4.4).

Resumen

Esta tesis se centra en el diseño de nanoestructuras basado en nanopartículas de óxido de hierro y liposomas. Pueden transportar medicamentos mejorando su localización y eficiencia. La combinación de estos dos componentes representa una oportunidad única para lograr múltiples objetivos terapéuticos. En primer lugar, se estudió la preparación y caracterización de nanopartículas uniformes de óxido de hierro obtenidas através de síntesis por microondas y se compararon con las obtenidas mediante técnicas de coprecipitación y descomposición térmica, logrando tamaños de núcleo de 8 a 15 nm (cap. 4.1). Muestras seleccionadas se encapsularon en liposomas que dieron lugar a diferentes distribuciones espaciales de las nanoparticulas: unidas a la superficie del liposoma, dentro de la bicapa lipídica o dentro del volumen acuoso. También se realizó la caracterización estructural y magnética (cap. 4.2).

El efecto de los procesos de agregación en las propiedades magnéticas se ha analizado en sistemas con diferentes distribuciones espaciales de las partículas, como partículas libres, magnetoliposomas y células incubadas con partículas (cap. 4.3). Finalmente, se evalúan las partículas y los magnetoliposomas *in-vitro* para verificar sus límites de citotoxicidad en las células y se analiza su posible aplicación como agentes de contraste negativo para el diagnóstico con imágenes de resonancia magnética, para el tratamiento de hipertermia magnética y como portadores de doxorubicina, con liberación controlada por un campo magnético alterno aplicado en diferentes líneas celulares (cap. 4.4).

List of Abbreviations

AC: Alternating current

ACS: AC susceptibility

AMF: Alternating magnetic field

APS: (3-Aminopropil)trietoxysilane

BBB: Blood–brain barrier

Cryo-TEM: Cryogenic electron microscopy

DC: Direct current

DIC: Differential interference contrast

DLS: Dynamic light scattering

DMEM: Dulbecco's Modified Eagle's Medium

DMSA: Dimercaptusuccinic acid

DMSO: Dimethyl sulfoxide

DNA: Deoxyribonucleic acid

DOPC: 1,2-dioleoyl-sn-glycero-3-phosphocholine

DOPE: Dioleoylphosphatidylethanolamine

DOPG: 1,2-dioleoyl-sn-glycero-3-phospho-(1-rac-glycerol)

DOTAP: 1,2-dioleoyl-3-trimethylammonium-propane

DOX: Doxorubicin

DPPC: Dipalmitoylphosphatidylcholine

DSC: Differential scanning calorimeter

DSPC: 1,2-Distearoyl-sn-glycero-3-phosphocholine

DSPE: 1,2-Distearoyl-sn-glycero-3-phosphoethanolamine

DTA: Differential thermal analysis

EPR: Enhanced permeation and retention effect

FCS: Fetal calf serum

FDA: U.S.A Food and drug administration

FOV: Field-of-view

FTIR: Fourier transform infrared

H_C: Coercivity

HEPES: 4-(2-hydroxyethyl)-1-piperazineethanesulfonic acid

HF-AMF: High-frequency alternating magnetic field

ICP/OES:Inductively Coupled Plasma/Optical Emission Spectrometry

IR: Infrared

K: intrinsic magnetocrystalline anisotropy

k_B: Boltzmann constant

K_{eff}: Effective magnetic anisotropy

LF-AMF: Low frequency alternating magnetic field

LMV: Large multilamellar vesicle

LRT: Linear response theory

ML: Magnetoliposome

M_L: Longitudinal magnetization

MRI: Magnetic resonance imaging

M_r: Remanent magnetization

M_s: Saturation magnetization

M_T: Transverse magnetization

MTT: 3-(4,5-dimethylthiazol-2-yl)-2,5-diphenyl tetrazolium bromide

MW: Microwave

MWCO: Molecular weight cut-off

NP: Nanoparticle

PBS: Phosphate Buffered Saline

PC: Phosphatidylcholine

PDI: Polydispersity index

PDT: Photodynamic therapy

PE: Phosphatidylethanolamine

RES: Reticuloendothelial system

RF: Radio frequency

ROS: Reactive Oxygen Species

RT: Room temperature

SAR: Specific absorption rate

SLP: Specific loss power

SQUID: Superconducting quantum interference device

SUV: Small unilamellar vesicle

T_1: Longitudinal relaxation time

T_2: Transversal relaxation time

T_B: Blocking temperature

T_C: Curie temperature

TD: Thermal Decomposition

TE: Echo time

TEM: Transmission electron microscopy

TGA: Thermogravimetric analysis (weight loss)

T_M: Phase transition temperature (melting temperature)

TR: Repetition time

UV-VIS: Ultraviolet–visible spectroscopy

VSM: Vibrating sample magnetometer

XRD: X-ray diffraction

ZFC-FC: Zero field cooling-Field cooling

τ: Relaxation time (effective)

τ_B: Brownian relaxation time

τ_M: Measuring time

τ_N: Néel relaxation time

μ_B: Bohr magneton

χ': real susceptibility

χ": imaginary susceptibility

Chapter 1

Introduction

1.1 Nanotechnology

Nanotechnology is the study and application of nano-sized materials, whose size provides new physical and chemical properties very different from those of bulk materials [1]. This is still a field of interest after decades of growth [2]. New applications emerged within the area of biomedicine in the last 30 years, based on these materials mostly focused on nanoparticles and more in particular, magnetic iron oxide nanoparticles (magnetite or maghemite) which are being used since iron is easily metabolized within the body [3] [4]. These particles have comparable sizes to proteins, cells and viruses, their surface can be modified to bind biomolecules of interest, the particles have a high magnetic moment and the magnetic field can cross the human body, noninvasively. These advantages makes these nanoparticles very promising for developing tools to diagnose, prevent and treat diseases, directing selectively the nanoparticles to diseased tissues and organs, thus avoiding the side effects of current treatments, and therefore these materials are object of study in this thesis.

One important area for the application of nanotechnology is the cancer, which accounted for around 8.2 million deaths worldwide in 2012 [5]. More than 14 million cancer cases are newly diagnosed every

year, and deaths are projected to rise, with an estimated 13.1 million in 2030. Efforts must be focused at finding better cancer therapeutic options that are effective, efficient and affordable. Currently the conventional cancer treatment options are chemotherapy, radiotherapy and surgery. Other problem faced today is that more than 95 % of new drug candidates fail to have the pharmacokinetic properties needed to be an effective treatment [6] [7]. The ideal case would be nanotechnology-based cancer treatment that combines targeted delivery with imaging, diagnostics and the ability to provide therapies within a single nanoscale structure. To assemble this multifunctional structure is complex and full of challenges, as it must be colloidally stable, resist protein adsorption and immune system recognition, and achieve cellular targeting in its original form (i.e., without losing components or cargo during circulation).

This work will be focused in two nanostructures: magnetic nanoparticles and magnetoliposomes. Magnetic nanoparticles (NP) can be tracked in biological matrices allowing their *in-vivo* monitorization and the quantitative determination of their biodistribution due to their characteristic magnetic behavior. Most common magnetic nanoparticles are iron oxides, mainly magnetite or maghemite and some of its applications are magnetic resonance imaging (MRI), magnetic hyperthermia treatments, photothermia, tissue regeneration, delivery of genetic materials and drug delivery [8] [9] [10] [11] [12] [13] [14].

Industrial challenges involved in developing magnetic nanoparticles for clinical applications have been recently highlighted [15] [16]. The limitation in many cases comes from the wide size distribution of the NP, the lack of aggregation control or the poor/weak functionality of the surface. Also, the development of this new technology implies the need to determine their toxicity and to identify potential risks and side effects that could arise from their biodistribution and biodegradation [17] [18] [19] [20]. Table 1.1 presents a list of some iron oxide nanoparticle systems approved by the US Food and Drug Administration (FDA) [21]. Nanotherm is in late stage clinical trials and FDA approval is pending. *Resovist*® was withdrawn due to low efficacy but is still used in many clinical trials as a reference element [22] [23].

Table 1.1: FDA-Approved iron oxide nanoparticle systems

Name	Description	Indication	Company
$Feridex^{®}$ (Endorem)	Ultra small	MRI contrast agent	Berlex
$Nanotherm^{®}$	15 nm	Glioblastoma	MagForce
$Resovist^{®}$	Ultra small	MRI contrast agent	Bayer
$GastroMARK^{®}$	400 nm (silicone-coated)	MRI contrast agent	Amag
$Feraheme^{®}$	17-31 nm (colloidal size)	Iron deficiency anemia	Amag
$Venofer^{®}$	4 nm	Chronic kidney disease	Luitpold

Liposomes are an attractive solution for drug delivery and biomedical imaging problems because they are biocompatible carriers capable of protecting and transporting hydrophobic and/or hydrophilic therapeutic molecules and optical actives. Another advantage is the fact that some liposomes formulations have already been approved by the FDA as can be seen in table 1.2 [24]. Liposomes became the first nanomedicines in FDA clinical trials, starting with approval of formulations with doxorubicin ($Doxil^{®}$) and Amphotericin B ($AmBisome^{®}$) in mid-1990s. Recently (2015) a liposomal drug carrier $Onivyde^{®}$ was approved. Some limitations of the liposomes are their colloidal stability, batch to batch reproducibility, sterilization methods, degradation with time, low drug entrapment and the difficulty of producing large batch sizes. Also all of the approved liposomal systems are based on passive targeting (where the drug can accumulate in the tumor site given its permeability due to compromised vasculature, known as EPR effect).

Table 1.2: Liposome-based formulations approved by the FDA

Product	Active Agent	Indication	Company
$Doxil^{®}$	Doxorubicin	Ovarian cancer	Alza Corporation
$Myocet^{®}$	Doxorubicin	Metastatic breast cancer	Teva Pharmaceutical
$DaunoXome^{®}$	Daunorubicin	Kaposi's sarcoma associated with HIV	Galen Inc
$ThermoDox^{®}$	Doxorubicin	Primary liver cancer	Celsion
$Rexin-G^{®}$	MicroRNA	Pancreatic cancer, osteosarcoma and soft tissue sarcoma	Epeius Biotechnologies
$Caelyx^{®}$	Doxorubicin	Ovarian and breast cancer	Schering-Plough
$AmBisome^{®}$	Amphotericin B	Fungal infection	Gilead Sciences
$Onivyde^{®}$	Irinotecan	Pancreas metastatic adenocarcinoma	Ipsen Biopharm

Given the advantages of magnetic nanoparticles and liposomes, it is expected that a platform based on the combination of both, such as the magnetoliposomes, could be a more efficient agent for drug delivery.

They could be stimuli responsive to a magnetic field and also could be followed by MRI. State of the art on liposomes and magnetoliposomes is discussed in the next sections.

1.2 Liposomes

Liposomes are concentric vesicles formed by a double layer of phospholipids, which are amphipilic i.e. they have a hydrophilic head and a hydrophobic tail [25]. In the presence of water these molecules are attracted (polar head) or repelled (apolar tail) forming a sphere with a small aqueous space inside (lumen), where it is possible to encapsulate drugs or particles [26]. Liposomes are formulated using naturally occurring and/or synthetic phospholipids such as phophatidylcholine (PC), phosphatidylethanolamine (PE), phosphatidylserine, and phosphatidylglycerol. Liposomes can be prepared also with zwitterionic, anionic or cationic lipids, and the net liposome surface charge can be adjusted by mixing different ratios of these components.

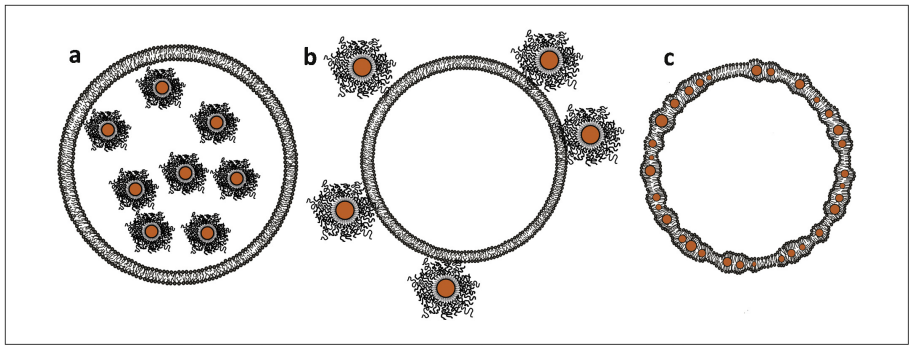

Figure 1.1: Liposome with nanoparticles (brown spheres) encapsulated in a) aqueous part, b) on the surface membrane or c) inside the lipid bilayer. Reproduced from [27].

The functional versatility of liposomes renders them one of the most intensively investigated delivery vehicles [24] [28]. Typically 100 nm to 200 nm in diameter, biocompatible, flexibility in terms of size and composition, easy modification of surface properties, and possible to engineer for long *in-vivo* circulation times, liposomes can carry both

hydrophilic cargo in the aqueous volume and hydrophobic cargo in the lipid membrane interior as seen in figure 1.1.

An important parameter to control is the phase transition temperatures (T_M) of the phospholipids. The lipids exist in either a fluid state ($T > T_M$) or a gel state ($T < T_M$), depending on their temperature. The fluid state of the lipids is more permeable to water and can be exploited to encapsulate drugs during liposome production. If the fluidification takes place at body temperatures ($T \approx 37\ ^oC$), the liposomes will become leaky, and the encapsulated drugs are likely to escape before reaching the site of action. Thus, choosing phospholipids with gel states at physiological conditions is often desirable to stabilize the liposomes. For example, Dipalmitoylphosphatidylcholine (DPPC $T_M = 42\ ^oC$) is often used to mimic the outer leaflet of a cellular membrane for studying the effect of particles on monolayers. This lipid is the chosen by most researchers as seen in table 1.3, and will be the phospholipid used through all this thesis.

A challenge to liposomal drug delivery is designing a colloidally stable and *in-vivo* long-circulating liposome that can be destabilized in a controlled fashion to facilitate drug release at a specific time and location. Release of the drug can then be externally triggered controlling its dose. This can be achieved by disruption or phase separation of the bilayer, induced by "melting" these liposomal bilayers, that is, heating to a temperature greater than its characteristic main phase transition (T_M) [6]. Important liposome characteristics were controlled in the last years like its reduction in size (smaller than 100 nm) and its surface functionalization making it possible to cross the blood–brain barrier (BBB) [29].

1.3 Magnetoliposomes

In 1988 magnetoliposomes (MLs) were introduced, where iron oxide nanoparticles were encapsulated either in the aqueous part or inside the liposome bilayer [30]. Magnets can be used to guide magnetoliposomes *in-vivo* and tracked by MRI. Controlled release for MLs can

be also achieved by using magnetic hyperthermia-triggering approach, thermosensitive components on the membrane became fluidified when high-frequency alternating magnetic field (HF-AMF) is applied [31]. Heating is achieved via magnetic losses of the nanoparticles through Néel or Brownian relaxation. However, this approach may not be suitable for the cases where temperature changes are harmful, such as in highly perfused organs (kidney, liver, lung) or in the brain tissues [32]. Hence, controlled release triggered by low-frequency alternating magnetic field (LF-AMF) would be highly desirable in which no hyperthermia is produced, but do mechanical damage. Recent reviews focusing on liposomes or NP for therapeutic applications, are provided in [33], [34], [6], [35], [36] and [27].

Some additional advantages of magnetoliposomes are their loading and delivering of hydrophobic and hydrophilic molecules/NP, their biocompatibility, ability to reduce drug degradation and toxicity.

As seen from table 1.3 a common lipid used by researchers is DPPC, used alone or in combination with other lipids, formed by dry lipid film in most cases. These formulations have been used with non functionalized nanoparticles or nanoparticles functionalized with citric acid ([44], [46], [47]) or oleic acid ([39], [42], [50]) , usually with small diameters below 15 nm and made of magnetite. It should be noted that unambiguous identification of partially oxidized Fe_3O_4 over $\gamma - Fe_2O_3$ is difficult. However, as NP of both nano-phases have similar magnetic properties the differentiation is not critical to the current work, so we shall refer to the phase as magnetite through all the text.

For most applications, the difference between encapsulated and free nanoparticles is important, and any paper reporting on release efficiency should carefully assess the encapsulation or membrane-bound fraction of nanoparticles. How nanoparticles organize in the membrane and how this affect the organization of the lipids is still argued in the literature and might be dependent on the detailed architecture of the nanoparticles and the method of liposome preparation [27]. Thus, iron oxide nanoparticles loaded into the liposome lumen of the vast majority of the reported magnetoliposomes agglomerated due to poor steric stabilization [27]. The phosphate of the phospholipid headgroup strongly

Table 1.3: Reported magnetoliposomes configurations

Lipid	Size	Method	Nanoparticles	Coating	Loading	Application	Cell tests	Ref.
DPPC	220 nm	dry lipid film + extrusion	10 nm Fe_3O_4	N/A	Protoporphyrin IX (PpIX)	Photodynamic Therapy	MCF-7	[37]
DPPC	Heterogeneous	dry lipid film	13 nm Fe_3O_4	N/A	Diphenylhexatriene	Hyperthermia	N/A	[38]
DPPC	200 nm	dry lipid film	5 nm Fe_3O_4	Oleic acid	Carboxylfluorescein	EMF heating	N/A	[39]
DPPC	N/A	dry lipid film	8 nm Fe_3O_4	N/A	Doxorubicin	AMF Treatment	N/A	[40]
DPPC	300 nm	dry lipid film	N/A Fe_3O_4	N/A	N/A	Gene Delivery	CHO	[41]
DPPC	40 nm	Muller-Rudin	10 nm Fe_3O_4	Oleic acid	N/A	NP adsorption on DPPC monolayer	N/A	[42]
DPPC	N/A	LIME/DMD simulation	1-25 nm	hydrophilic	N/A	Interaction between NP and bilayer membranes	N/A	[43]
DPPC	N/A	LIME/DMD simulation	1-4 nm	hydrophobic	N/A	Interaction between NP and bilayer membranes	N/A	[43]
DPPC	150 nm	dry lipid film	7 nm Fe_3O_4	Citric acid	Gemcitabine	AFM treatment and chemotherapy	MSC	[44]
DSPC	100 nm	dry lipid film + extrusion	5 nm / 10 nm Fe_3O_4	NitroDOPA-palmityl	Calcein	AMF treatment	N/A	[45]
DPPC + DSPC	200 nm	dry lipid film	7 nm / 9 nm Fe_2O_3	Citric acid	Rhodamine	Hyperthermia	MCF-7 *	[46]
DPPC + DSPC + DSPE	200 nm	dry lipid film	9 nm Fe_3O_4	Citric acid	m-THPC	Hyperthermia and photodynamic therapy	SKOV-3 and A431 *	[47]
DPPC + Chol + DSPE	200 nm	dry lipid film + extrusion	10 nm Fe_3O_4	N/A	Doxorubicin	Hyperthermia and drug release	KB and HeLa	[31]
DPMG	Heterogeneous	Mixture and incubation	14 nm Fe_3O_4	Lauric acid	N/A	N/A	N/A	[30]
DMPC	N/A	simulation	2.4 nm	N/A	N/A	Interactions between NP and cell membranes	N/A	[48]
DPPC + Chol + DSPE	200 nm	dry lipid film + extrusion	164 nm $C60 - Fe_3O_4$	PEG	DTX	Thermo-chemotherapy	MCF-7 *	[49]
DPPC + DOPC	110 nm	freeze/thaw + extrusion	7 nm Fe_3O_4	Oleic acid	Doxorubicin	AMF treatment	N/A	[50]
DOTAP + DOPE	200 nm	dry lipid film + extrusion	32 nm Fe_3O_4 (DLS)	Oleic acid	Silencing RNA	Gene delivery	COS-7 / HeLa / TKD2 *	[51]
DOPG + DOPC	90 nm	mixture and incubation	13 nm Fe_3O_4	DOPG	N/A	MRI contrast agent	N/A	[52]
PC	300 nm	dry lipid film	9 nm Fe_3O_4	Dextran	N/A	efficiency of encapsulation	N/A	[53]
PC	220 nm	dry lipid film	3-5 nm Fe_3O_4	Dextran	Doxorubicin	LF AMF	SH-SY5Y	[32]
PC	146 nm	dry lipid film	10 nm Fe_3O_4	N/A	Doxorubicin	Targeted drug delivery	N/A	[54]
PC	100 nm	dry lipid film + extrusion	6.6 nm Fe_3O_4	N/A	Alexa Fluor 555 / JPM-565	MRI contrast agent	MEFs *	[55]
PC	200 nm	dry lipid film + extrusion	8 nm Fe_2O_3	Citric acid	N/A	MRI contrast agent	J774 *	[56]
PC	10-50 μm	Electroformation	¡ 50 nm $CoFe_2O_4$	Silica	Alexa 488-C5-maleimide	LF AMF	N/A	[57]

DPPC = 1,2-dipalmitoyl-sn-glycero-3-phosphocholine; DSPC = 1,2-Distearoyl-sn-glycero-3-phosphocholine; DSPE = 1,2-Distearoyl-sn-glycero-3-phosphoethanolamine; DOPC = 1,2-dioleoyl-sn-glycero-3-phosphocholine
DOPE = dioleoylphosphatidylethanolamine; DOTAP = 1,2-dioleoyl-3-trimethylammonium-propane; DOPG = 1,2-dioleoyl-sn-glycero-3-phospho-(1-rac-glycerol); PC = L-α phosphatidylcholine; Chol = cholesterol

N/A = not applicable or not available, * Works that also performed *In vivo tests*

interacts with bare iron oxide [53]. Uncoated iron oxide nanoparticles or sterically stabilized with starch or dextran interact with and might disrupt the liposome membrane [27]. However, nanoparticles incorporated in the membrane have the advantage of directly transferring the locally generated heat to the membrane itself.

A major challenge though is to incorporate nanoparticles without compromising membrane integrity and cause leaking of encapsulated compounds. High loading is needed for triggering bilayer release, but can lead to NP aggregation and can compromise the liposome structure and stability. Controlled release usually report a local or nanoscale heating mechanism where the NP transfer heat to the liposome and cause a phase change within the bilayer that triggers bilayer permeabilization, which must be further studied given the rapid heat dissipation from the NP surface [38]. For example, a loss of membrane structure and an increase in permeability is observed if the nanoparticle coating is not irreversibly linked to the core. Nonleaking liposomes were observed for nanoparticles stabilized with palmityl-nitroDOPA [45], while liposomes containing oleic acid showed membrane deformation and rapid passive leaking [39] [57].

Triggered cargo release from liposomes containing superparamagnetic nanoparticles in the membrane interior by applying low [57] and high frequency alternate magnetic field (AMF) was demonstrated recentl y[45] [39]. Release triggered by low frequency AMFs applied to membrane associated nanoparticles [57] clearly relied on mechanical membrane distortion while for high frequency AMFs, local heat generation lead to a membrane permeability [45] [39]; however, the local heat mechanism has not been directly demonstrated and it has been argued that bulk heat diffusion is too fast for local heating to be possible [6]. Regardless of the mechanism, these results demonstrate that magnetically triggered release from liposomes incorporating nanoparticles within the membrane can be performed with low leakage and high dosed efficiency, while minimally affecting the surrounding environment. Full use of magnetic liposomes for drug delivery would combine magnetically triggered release with other known properties of liposomes such as stealth coatings and targeting.

Those magnetoliposomes could be used as carriers for drugs such as Doxorubicin (DOX), a highly effective anticancer drug, although its usage is limited because of its side-effects, probably the most serious being heart failure [58]. Magnetoliposomes could be used to control the release rate of DOX, which could significantly impact its safety and efficacy. But drug delivery from liposomes has to be accomplished by cellular uptake, which can occur by adsorption, endocytosis, fusion and/or lipid transfer [35]. For the tumors treatments some novel techniques have been rapidly emerged due to their high therapeutic potential such as magnetic hyperthermia, photodynamic therapy (PDT) or immunotherapy, beside the conventional methods such as chemotherapy.

Liposomes or NP for therapeutic application are well established and have been approved by the FDA for clinical use, however the combination of these two systems represents a unique opportunity for achieving multiple therapeutic objectives. Nonetheless, the design and use of magnetoliposomes is still in the beginning as can be seen from the works summarized in table 1.3. Further studies are needed to demonstrate the relationship among NP loading, liposome morphology, structure and stability, and bilayer permeability for different liposome designs.

1.4 Objectives

The general objective of this thesis is the design of a nanocarrier based on liposomes and iron oxide nanoparticles, which can be loaded with drugs, achieving a combined therapeutic agent.

This thesis was oriented toward the following specific objectives:

i) Synthesis of uniform iron oxide nanoparticles through microwave assisted method, controlling their size, shape, internal structure, assembly and consequently, tailoring their magnetic features. They will be compared to nanoparticles obtained by other synthesis methods.

ii) Production of magnetoliposomes through different methods, controlling their size and the spatial distribution of nanoparticles, depending on the nanoparticle coating.

iii) Study of nanoparticles and magnetoliposomes interaction with biological systems (Pan02 and Jurkat cell lines) and the effects on their magnetic and colloidal properties.

iv) Assessment of the toxicity of the magnetic nanoparticles and magnetoliposomes *in-vitro* and its application as T_2 MRI contrast agents and as generators of magnetic hyperthermia.

v) Investigation of the efficiency of magnetoliposomes as drug delivery vectors (for doxorubicin) using HeLa and MDA-MB-231 cells.

In order to achieve such tasks, the thesis was divided in four distinctive but complementary parts. Chapter 2 reports the scientific background needed along the thesis, Chapter 3 describes materials and procedures followed on this thesis, Chapter 4 is focused on describing and discussing the main results and at last, Chapter 5 collects the key conclusions from this work.

The experimental part was carried out at the Institute of Material Science of Madrid (ICMM), belonging to the Spanish national research council (CSIC), in the group of Materials for Health. Additionally, part of the results of the characterization arise from external collaborations with Prof. Gerardo Prieto at the University of Santiago de Compostela in Spain, Prof. Christer Johansson at the RISE Acreo Institute in Sweden, Dr. Lucía Gutiérrez at the University of Zaragoza in Spain and Dr. Francisco Javier Chichón at the National Center of Biotechnology in Spain. Results of biomedical applications arise from external collaborations with Prof. Angeles Villanueva at the Autonomous University of Madrid in Spain, Prof. Domingo Barber at the National Center of Biotechnology in Spain, Prof. Fernando Herranz at the National Center for Cardiovascular Research in Spain and Dr M. Concepción Serrano at the Institute of Material Science of Madrid.

Chapter 2

Fundamentals

This chapter reports on the scientific background that will be needed along the thesis to support the results and discussion in the following chapters. It starts with a general view of magnetism at the nanoscale, passing through particle formation and growth mechanisms, microwave assisted synthesis particularities and liposomes formation. By the end of the chapter an overview on bio applications of magnetic nanoparticles and magnetoliposomes is summarized, including first, interactions between nanoparticles and biological media, cell uptake and then, the use of these nanosystems as contrast agents for MRI, magnetic hyperthermia treatment and drug delivery platforms.

2.1 Magnetism at the nanoscale

This part of the chapter will deal with different classes of magnetic materials: diamagnets, paramagnets, antiferromagnets and ferromagnets. Materials can be classified according to their response to an external magnetic field. Magnetic properties of the materials originate essentially from the magnetic moments of the electrons in incomplete layers in the atoms and of the electrons in the conduction band, in the case of metals.

First the diamagnetism is a basic property of all substances and involves a slight repulsion by a magnetic field, being very weak [59]. The slope of magnetization vs applied field, named magnetic susceptibility, is negative, small (around -10^{-6}) and independent of the temperature. Some examples are the water and almost all biological materials having N, C, O and H [60] [61].

On the other hand, paramagnetic substances are attracted towards a magnetic field. The magnetic susceptibility is positive, small (0 to 0.01) and varies with the temperature [59]. An example is the hemoglobin in the human body [62]. Such substances possess unpaired electrons which are randomly oriented on different atoms. In the absence of an applied field, the atomic moments are randomly distributed and cancel each other, so that the magnetization of the sample is equal to zero. When a field is applied, due to the interaction of the field with the moments, known as Zeeman interaction, there is a tendency for each atomic moment to turn towards the direction of the field; if there are no opposing forces acting, the full alignment of the atomic moments would be produced and the whole sample would acquire a great moment in the direction of the field. But the thermal agitation of atoms opposes this tendency and tends to keep the atomic moments pointed randomly. The result of the competition between thermal energy and Zeeman energy is only a partial alignment of the spins in the direction of the field and therefore a small positive susceptibility. The effect of an increase in temperature is to increase the randomization effect of thermal agitation and, therefore, decreasing susceptibility.

Antiferromagnetic substances have a small positive susceptibility at all temperatures and below a critical temperature (Néel temperature) the tendency of antiparallel alignment of moments is strong, acting even in the absence of an applied field. It has two interpenetrating and identical sublattices of magnetic ions that are magnetized in opposite directions resulting in a zero net moment at zero field. A moment is obtained only when a strong field is applied to it. Most of the antiferromagnetic materials are ionic compounds, like iron oxide $\alpha - Fe_2O_3$.

Finally, ferro - and ferrimagnetic substances are strongly attracted

Table 2.1: General properties of the main iron oxides.

	Hematite $\alpha - Fe_2O_3$	Magnetite Fe_3O_4	Maghemite $\gamma - Fe_2O_3$
Lattice system	rhombohedral hexagonal	cubic	cubic or tetragonal
Structural type	corundum	inverse spinel	defect spinel
Cell dimension (nm)	a = 0.50356 / c = 1.37489	a = 0.8396	a = 0.83474
Density ($g\ cm^{-3}$)	5.26	5.18	4.87
Colour	red	black	reddish-brown
Type of magnetism	weakly ferromag. or antiferromag.	ferrimag.	ferrimag.
Curie temperature (K)	956	850	820-986

by a magnetic field. At the ferromagnetism, the spins are aligned parallel to each other as a result of the strong interaction between neighboring spins, known as exchange interaction, with a large $(0.01 - 10^6)$ and positive susceptibility. As the temperature increases, the arrangement between the spins is disturbed by the thermal agitation, resulting in a dependence on temperature. Below a certain temperature (Curie, T_C) the materials undergo a transition to a magnetically ordered state and above this temperature the materials lose their magnetic properties. On the other hand, ferrimagnetic substances consist of at least two interpenetrating sublattices of magnetic ions, which are antiparallel. However, the different spins have unequal moments, so it has a net magnetic moment that also depends on the temperature [59]. In this thesis the focus will be on iron oxides, as for example Hematite, Magnetite and Maghemite. Some of their properties can be seen in table 2.1, like the structure, cell dimensions, type of magnetism, Curie temperatures (T_C) and its density.

Besides the magnetic properties seen above another important parameter is the materials effective anisotropy (K_{eff}), including magnetocrystalline, shape and surface anisotropy, specially important for nanoparticles, among others. The magnetocrystalline one is based on the fact that each crystal has a preferred direction of magnetization known as the direction of easy magnetization where in metallic iron, for example, is the direction [100], while for iron oxides such as magnetite is [111] [1]. Applying a magnetic field along these directions, maximum magnetization is achieved. Shape anisotropy is related to the fact that for non spherical particles, it will be easier to magnetize them along the larger axis, because the demagnetizing field along the

minor axis is stronger than along the long axis. Thus the shape can be a source of magnetic anisotropy. Finnaly, surface anisotropy originates from the breaking of symmetry due to particle boundaries, since surface atoms do not have the same amount of neighbors as an atom in the middle of the particle. This fact is important for particles of nanometric size because they have a very large surface/volume ratio. As the particle size decreases, contributions due to the surface become more important than shape [63], [64].

2.1.1 Magnetization process

A hysteresis loop is generated measuring the magnetic response of a ferromagnetic material while the magnetizing force is changed (figure 2.1).

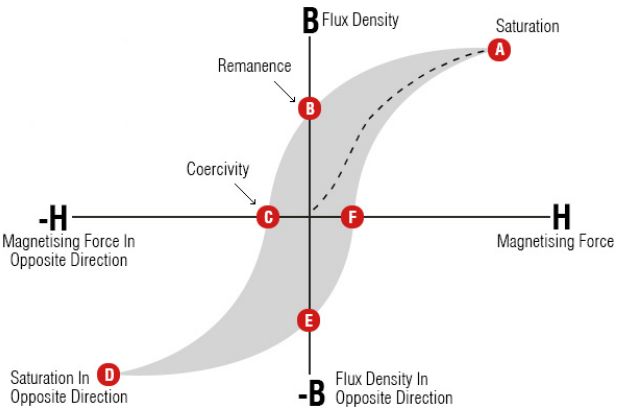

Figure 2.1: Hysteresis loop showing the relationship between the induced magnetic flux density (B) and the magnetizing force (H).

If the material have never been magnetized (or it has been demagnetized) it will follow the dashed line from the middle (H=0) to point A, representing the magnetic saturation (M_s), where all of the magnetic domains are aligned. When H is reduced to zero the curve will move from point A to point B, where it can be seen that some magnetic flux remains even though H = 0, called as remanent magnetization (M_r) indicating a residual magnetism in the material. Reversing the magnetizing force the curve moves from point B to point C, called co-

ercivity (H_c), where the magnetization within the material is zero. As the magnetizing force is increased in the negative direction the material will become magnetically saturated, now in the opposite direction, point D. By reducing H to zero the curve goes from point D to E, having a residual magnetism equal to that achieved in the other direction (point B). Now increasing H back in the positive direction the curve goes from point E to F, returning to H = 0, the same as point C but in opposite directions. Increasing H even more the curve moves from F to A, closing the loop. Important note is that the curve did not return to the dashed line because some force is required to remove the residual magnetism. Superparamagnetic materials have zero coercivity and zero remanent magnetization and the M(H) curve form has sigmoidal shape with no hysteresis.

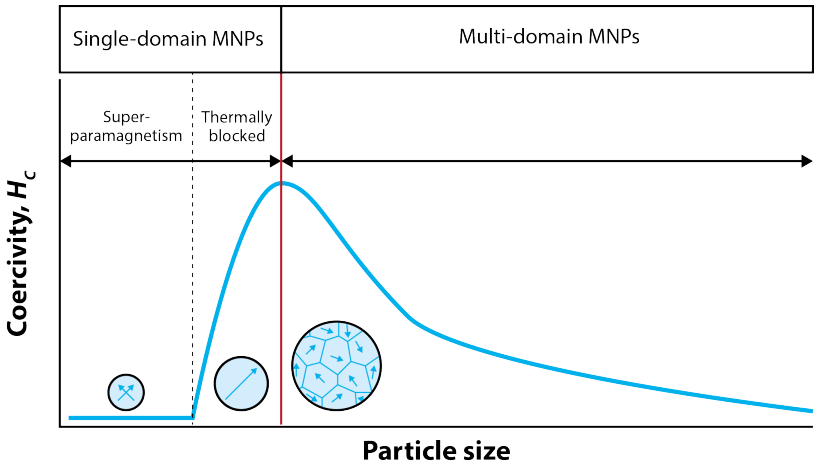

Figure 2.2: Relation between particle size and its coercivity, addicionaly with a schematic idea of the domain walls dependence with size. Kindly provided by [65].

The magnetic behavior at a given temperature depends on the nanoparticle size as can be seen in figure 2.2, where the relation between the particle size and its coercivity is visually presented, in the case of a large particle it is formed by multi-domains with the formation of domain walls, as the particle reduces in size, the domain wall disappears (since is not energetically favorable for the system [1]) and it becomes a monodomain. Reducing even more the particle size appears a phenomenon called superparamagnetism. In the case of iron oxides

this separation between multi-domain and monodomain is around 50 nm, the exact value will depend on the intrinsic properties of the material (saturation magnetization and anisotropy constant for example) [66].

Consider a set of monodomain particles with uniaxial anisotropy, each with an anisotropy energy density of $E = Ksin\theta^2$, where K is the anisotropy constant and θ the angle between the magnetization (μ) and the easy axis of magnetization. If the volume of each particle is V, the energy barrier $\Delta E = KV$ has to be overcome so that the particle can reverse its magnetization (figure 2.3). Now, in any material, thermal energy fluctuations are occurring continuously on a microscopic scale. In 1949 Néel pointed out that if monodomain particles become sufficiently small, KV would become so small that fluctuations energy could overcome the forces of anisotropy and spontaneously reverse the magnetization of a particle from one direction to another, even in the absence of an applied field. Each particle has a magnetic moment $\mu = M_s V$ and, if a field is applied, it tends to align the moments of the particles, whereas the thermal energy tends to misalign them. As a result, Bean coined the term superparamagnetism to describe the magnetic behavior of these particles. This subject can be seen in more depth in [67].

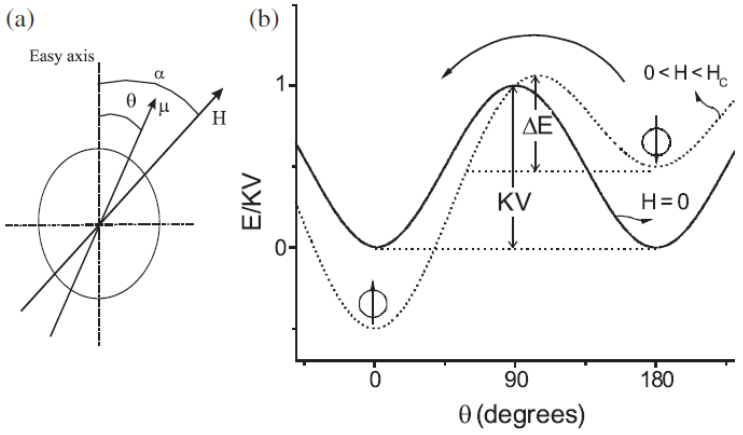

Figure 2.3: a) Definition of the axis system, (b) angular dependence of the energy barrier whithout applied field (continuous line) and for applied field smaller than coercive field (dotted line) [68].

The magnetic moment of a nanoparticle has only two stable orientations as seen in figure 2.3, separated by an energy barrier. At a given temperature, there is a probability for the magnetization to flip and reverse its direction. The mean time between two flips is called the Néel relaxation time τ_N and is given by the Néel-Arrhenius equation,

$$\tau_N = \tau_o e^{\frac{KV}{k_B T}} \tag{2.1}$$

where τ_o is an intrinsic relaxation time (typical values are between 10^{-9} and 10^{-10} seconds), KV is the height of the energy barrier and $k_B T$ is the thermal energy of the system.

The magnetic behavior observed is dependent on the measuring time (τ_M), which vary depending on the technique used, going from 100 s (typical magnetic measurements like SQUID) to 10^{-8} s in Mössbauer spectroscopy. If $\tau_M \gg \tau_N$ so the nanoparticles are in a superparamagnetic regime, while if $\tau_M \ll \tau_N$ the nanoparticles are observed in a blocked state. The temperature that divides this two regimes is called blocking temperature (T_B), which depends on the characteristic measuring time. T_B is associated to the energy barrier KV, increases as the nanoparticle core size increases (since its volume increases). Fixing the volume as $V = V_o$, substituting $\tau_N = \tau_M = 100$ s at Néel-Arrhenius equation the blocking temperature is defined as,

$$T_B = \frac{KV_o}{25k_B} \tag{2.2}$$

Noticing that the blocking temperature is directly proportional to the nanoparticles volume and its anisotropy constant, the larger the nanoparticles higher is the temperature needed to enter the superparamagnetic regime.

When the magnetic field reverse the orientation being the nanoparticles suspended in a liquid carrier they can present a Brownian relaxation (τ_B) time which is given by,

$$\tau_B = \frac{3\eta V_h}{k_B T} \tag{2.3}$$

where η is the liquid viscosity, V_h is the hydrodynamic size of the nanoparticle and $k_B T$ is the thermal energy of the system.

A representation of this two relaxation systems can be seen in figure 2.4.

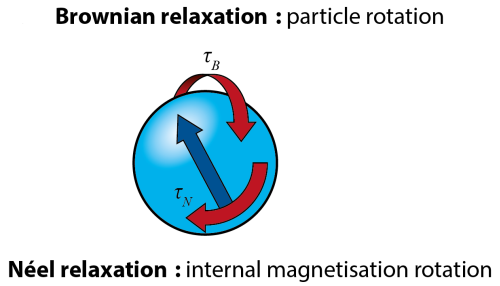

Figure 2.4: Two possible mechanisms of relaxation for a nanoparticle, Néel and Brownian. Kindly provided by [65].

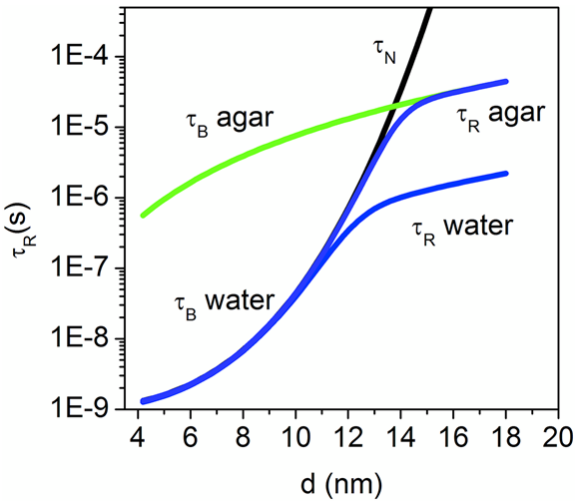

Figure 2.5: Relaxation times for iron oxide nanoparticles dispersed in water or immobilized in agar as a function of nanoparticle size. Relaxation times τ_B (Brownian), τ_N (Néel) and τ_R (Effective) have been calculated considering a mean effective anisotropy $K_{eff} = 3 \times 10^4 J/m^3$. Reproduced from [69].

For a specific nanoparticle size the faster relaxation time dominates over the other, but as a system of nanoparticles has a size distribution it presents both, as one can see at figure 2.5, where the effective relaxation time that dominates the system is a function of size. For small nanoparticles, Néel relaxation time is faster than the Brownian one, for bigger nanoparticles Brownian time becames more important. For dried samples, Brownian relaxation time is suppressed and nanoparticles can only present Néel relaxation.

2.1.2 Dynamic magnetic properties

Dynamic magnetic properties can be analyzed by AC measurements, since this information is not obtained in static DC measurements where the applied magnetic field direction is constant during the measurement time. In the dynamic measurement for superparamagnetic nanoparticles a small AC magnetic field is applied causing a fluctuation of the magnetic moment in the sample, caused by Néel or Brownian rotation of the magnetic moments. When measuring the dynamic properties as a function of the frequency, one determines the real and the imaginary parts of the dynamic susceptibility over a frequency interval, and it can be analyzed by integrating the Debye model over a size distribution of particles. The Debye model is given by,

$$\chi(\omega) = \frac{\chi_o}{1 + i\omega\tau} \tag{2.4}$$

where χ_o is the static susceptibility, $\omega = 2\pi f$ is the angular frequency (where f is the excitation frequency), and τ is a characteristic relaxation time (effective), which is given by,

$$\tau = \frac{\tau_B \tau_N}{\tau_B + \tau_N} \tag{2.5}$$

The susceptibility component that is in phase with the excitation field is the real part (χ') and the susceptibility component that is in quadrature to the excitation field is the imaginary part (χ"), figure

2.6. The main parameters that determine whether there is a Néel or Brownian relaxation at a given temperature are the size distribution of the nanoparticles, their magnetic anisotropy, the viscous properties of the liquid and magnetic interactions between the nanoparticles.

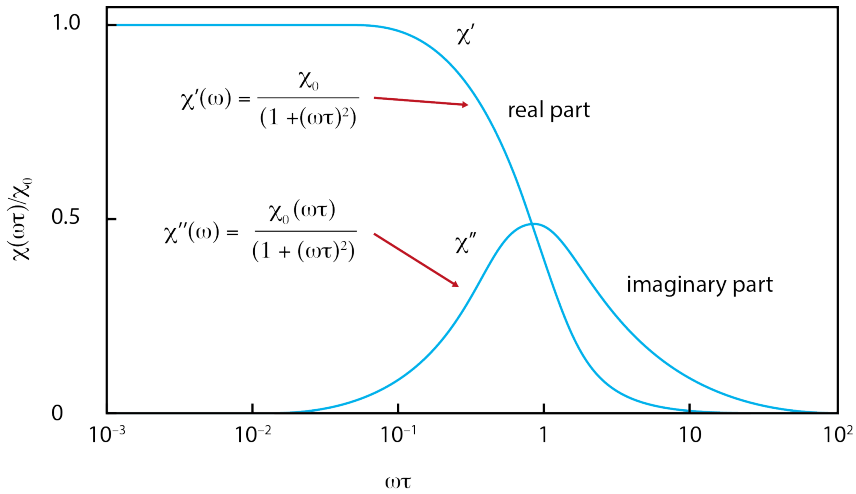

Figure 2.6: Real and imaginary part of the AC susceptibility versus excitation frequency. Kindly provided by [65].

AC measurements can be performed as a function of frequency or temperature. When measuring superparamagnetic nanoparticles AC response as a funcion of temperature the blocking temperature of the system can be determined as the maximum in χ", being a technique sensitive to aggregation and transformation processes. The signal for diamagnetic and paramagnetic species (for example tissues and blood) do not contribute to the χ" signal (zero constant), which makes a useful method to study magnetic nanoparticles in biological matrices, being possible to follow the biodegradation of this magnetic nanoparticles in animal models [70]. The advantage of AC measurements in frequency is the possibility to do the measurement in liquid phase at room temperature and also visualize the behavior of aggregated or larger particles (>20 nm), whose relaxation peaks appears at lower frequencies than those for smaller nanoparticles. This measurements are not always possible when working with AC temperature measurements, where the χ" peaks appears at temperatures higher than room temperature for larger nanoparticles. The peak height gives informa-

tion about the iron concentration in AC temperature measurements while for AC measurements in frequency gives information about heat release from nanoparticles at a specific frequency.

2.2 Magnetic nanoparticles and liposomes

2.2.1 Monodispersed nanoparticles

The formation of uniform magnetic nanoparticles can be described by the classical method of LaMer [71] [72] [73], as seen in figure 2.7, which can be separated in three different stages.

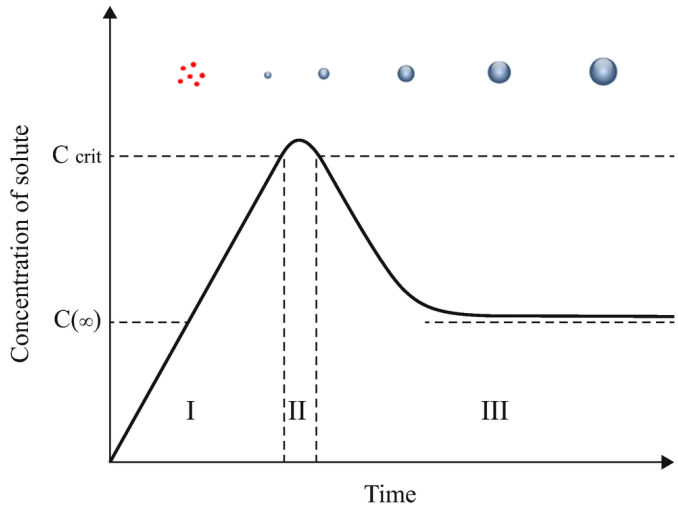

Figure 2.7: Classic LaMer mechanism for nanoparticle growth, where the concentration of solute varies with time. Stage I, the solute concentration increases to the critical supersaturation concentration required for nucleation. Stage II, the monomer saturation is partially relieved by the nucleation event. Stage III, the monomer concentration drops and particle growth proceeds by addition of the monomer to the particle surface and additional growth proceeds by Ostwald ripening.

I) The monomers (species that are dissolved in solution but unstable to form a particle) being produced usually by a chemical reaction

accumulate in solution, which reach the metastable region being supersaturated. No particles are formed in this step. II) The monomer concentration in solution exceeds the critical level of supersaturation and particles start to nucleate. III) Growth of nanoparticles continues without further nucleation. Growth after the exhaustion of precursor can occur through a diffusion process, aggregating or by Ostwald ripening [74], [75], [76], where larger particles grow at the expense of smaller ones, not being the last two ones a part of the original LaMer process. At a closed system the number of nanoparticles is defined in the nucleation event, which can be altered through the choice of reaction conditions though being a process of stochastic nature the control is extremely difficult.

Working with organic precursors as in the case of this thesis, different strategies are used to control particle size and shape. For example the oleic acid added to the solution acts as a surfactant controlling the distance between the nuclei limiting the growth (figure 2.8) [77]. In terms of shape the most commonly obtained for magnetite are spherical, cubical and rhombohedral given the spinel structure.

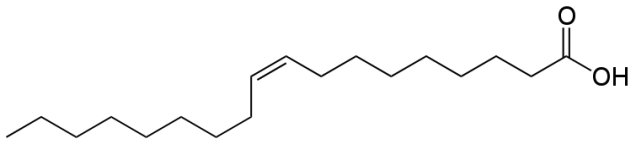

Figure 2.8: Oleic acid molecule.

Surfactant/precursor molar ratio and heating rate are crucial parameters to control the final nanoparticle size. For example, by decreasing the oleic acid/precursor ratio the mean size of the magnetite increases when the precursor is iron oleate but decreases when the precursor is iron acetylacetonate [75], [78]. Heating rate is other critical parameter to control the final nanoparticle size, so when it is properly adjusted the nucleation rate decreases, less nuclei are formed and they are able to grow more [79].

The nature of the surfactants can determine the final morphology of the magnetite nanoparticles synthesized in organic media, as

by the presence of sodium or potassium impurities may lead to cubic nanocrystals [80]. Cubic shapes can also be induced by the high amount of surface-active species in solution being the growth kinetically controlled [81].

Many other shapes can be achieved through changes in the precursors, surfactants, pH, reaction times, final temperatures, concentrations, solvents, heating method and pressure. Some of these shapes can be octahedrons, rods, disks, rings, tubes, hollow spheres or hollow cubes. For more details on this topic consult reference [82]. There is also the possibility of building nanostructures by mixing noble metals and magnetic nanoparticles, opening a spectrum of desirable synergistic and complementary effects, resulting in core-shell, dimer, composite or flower structures [10], [83]. This area is not within the scope of this thesis.

The main advantage of working with thermal decomposition synthesis if the fact that the nanoparticles are highly monodispersed with a low polydispersity index (PDI) as 0.1 (PDI(TEM)=(SD/average size)*100). The disadvantages of this method are its poor batch to batch reproducibility, the synthesis price and the temperature gradients, making it difficult the production of large batches. To overcame this difficulties, microwaves seems to be an excellent alternative for heating, which will be discussed next.

2.2.2 Microwave synthesis

In the past decades a new synthesis has gained a lot of attention, the microwave dielectric heating. It was due to its versatile applications, such as polymer chemistry, biomedicine, material science and nanotechnology. This non-classical heating has shown an expressive reduce in synthesis time, from hours to minutes, increase product yield and improve material properties, when compared to the conventional heating (by heat transfer), improving its reproducibility [84]. The first reports on microwave heating in chemistry are from 1986, by the groups of Gedye and Giguere [85], [86], since the first commercial microwave oven for home use is from 1954. Microwave (MW) is an electromagnetic

energy with frequencies in the range between 300 to 300.000 MHz. In this region only molecular rotation happens, not affecting molecular structures, given the very low energy of photons (0.037 kcal/mole), when compared to the required energy to break molecular bonds (80-120 kcal/mole).

The traditional heating is slow and inefficient, transferring energy from the reaction vessel to the mixture, overcoming the low thermal conductivity of the reactant mixture by convective currents driven by temperature gradients inside the reaction solution. In contrast, microwave irradiation triggers homogeneous heating by two mechanisms, dipolar polarization and ionic conduction. The dipoles (like a polar solvent) contribute with the first one while the charged particles in the mixture contribute with the second one.

The heat due to dipolar polarization takes place when a sample is irradiated with microwave frequencies, the dipoles tend to align in the direction of the applied electric field. As the field oscillates, the dipoles try to realign along the alternating field streamlines, in such a way energy is loss in the form of heat, through dielectric loss (material's inherent dissipation of electromagnetic energy) and molecular friction. If the dipole does not have enough time to realign with the applied field, no heating will occur, the same if it reorients too quickly. The frequency 2.45 GHz, corresponding to a wavelength of 12.24 cm, chosen by all commercial systems, is between these two extremes and does not interfere with phone frequencies and telecommunication.

The heat comming from ionic conduction is related to the ions (usually) oscillating under the influence of the microwave irradiation, colliding with other molecules and atoms in the way. These create heat by friction and agitation. To quantify the dielectric loss of a specific material it is used the so called loss tangent, the ability of a specific substance at a given frequency and temperature, to convert electromagnetic energy into heat. So $\tan\delta = \frac{\varepsilon''}{\varepsilon'}$, where ε" is the dielectric loss and ε' is the dielectric constant. For rapid heating is required a medium with high $\tan\delta$. Some common organic solvent and its respective value $\tan\delta$ can be seen in table 2.2 [87]. If $\tan\delta > 0.5$ the solvent is classified in high microwave absorbing, if $0.1 < \tan\delta < 0.5$

is medium and if tanδ < 0.1 is classified as low. In summary, when considering solvents for the microwave reaction, boiling points become less important, since the pressurized vessels provide greater options of solvents, with lower boiling points, but the efficiency of the mixture to couple with an applied microwave field is the crucial parameter. Using the table 2.2 gives an idea of which solvent is more appropriate for the required nanoparticle synthesis.

Table 2.2: Solvents dielectric constants.

Solvent	**tanδ**	**Solvent**	**tanδ**
Ethylene Glycol	1.350	Acetone	0.054
Ethanol	0.941	Dichloromethane	0.042
2-propanol	0.799	Toluene	0.040
Water	0.123	Hexane	0.020

As commented above the irradiation produces internal heating by direct coupling of the energy from the microwave with the molecules in the mixture, the more polar a reaction mixture is, the greater will be its ability to couple with the microwave energy. The gradient of temperatures in microwave versus oil-bath heating can be seen in figure 2.9.

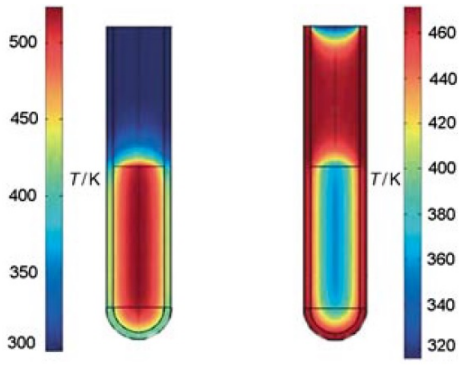

Figure 2.9: Temperature gradients in microwave (left) versus oil-bath heating (right) after 1 minute of irradiation. The wall temperature in the oil-bath is much higher than the one from microwave, where the whole volume is heated simultaneously [88].

The Arrhenius law $\kappa = Ae^{\frac{-Ea}{RT}}$ is an equation for the temperature dependence of reaction rates, which depends on two factors, the frequency of collisions between molecules (A) and the fraction of these molecules that have enough energy to overcome the energy barrier $e^{\frac{-Ea}{RT}}$. Microwave energy will affect the temperature parameter in this equation, increasing the temperature cause a more rapidly movement of molecules, which leads to more energetic collisions [87].

Nanoparticles synthesis were carried out on the new reactor available on the market with built-in magnetic stirrers, temperature measurements by internal fiber-optics probes, infrared sensors on the vial's surface and pressure/temperature control through the power delivered, as seen on figure 2.10 [89].

Figure 2.10: Monowave 300, Anton Paar GmbH, Austria, equipped with dual internal/external temperature monitoring system.

Conventional microwaves, or household ovens doesn't hold internal temperature or pressure controls leading to violent explosions, not being used nowadays in the laboratory due to safety reasons in closed recipients. Microwave instrumentation for synthesis can be classified in two kinds, one that is known as multimode ovens since one or two magnetrons create the microwave irradiation, directing it to the sample through the cavity in a chaotic way forming 'hot spots', while the other is known as monowave ovens, where the microwave energy is created by a single magnetron and directed to the sample in a homogeneous way (figure 2.11). This monowave oven was the one used in this thesis.

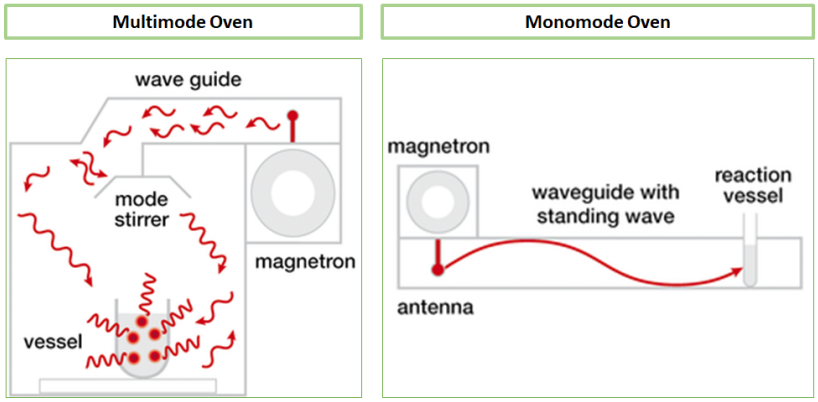

Figure 2.11: Schematic of the field distribution in a multimode and monomode oven.

Microwave synthesis is really versatile [84], as it can be found works in the literature from different groups around the world, studying wet-chemical fabrication of metal nanocrystals [90], polyol-based reactions [91] [92], core-shell hybrid nanocrystals [93] and transition-metal oxides such as magnetite [94]. Preparation routes for transition-metal oxide nanocrystals rely on nonhydrolytic pathways, in non-aqueous solvents [94]. These routes allow a good control over structure, size and shape of the nanocrystals. Alcohols are classified as high tanδ values, being convenient as reaction media for this non-aqueous microwave-assisted synthesis. Thus, small Fe_3O_4 nanocrystals were successfully produced, below 10 nm, by ultrafast reaction of benzyl alcohol with iron(III) acetylacetonate in just a few minutes at 200 ^oC under microwave heating [95]. Further reduction in size can be achieved in a facile, rapid and reproducible way, to synthesize Fe_3O_4 nanoparticles of 6 nm, the reaction of iron(III) acetylacetonate and 1,2-hexadecanediol in dibenzyl ether, in the presence of oleic acid and a ionic liquid [bmim][BF4] at 250 ^oC for 10 minutes [96]. Uniform flower-like Fe_3O_4 clusters were fabricated in ethylene glycol with $FeCl_3$, sodium acetate and a surfactant, under microwave irradiation at 160 ^oC for 15 to 60 minutes. Crystals were about 7 nm after 15 min of reaction, and increased to 12 and 15 nm after reaction for 30 and 60 min, respectively [97]. It was speculated that microwave irradiation set the conditions for creating nanocrystals seeds and accelerated its clustering under assistance of stabilizers. Finally ultrasmall nanoparticles with citrate coating can

be synthesized in only 10 minutes, mixing $FeCl_3$, sodium citrate and hydrazine in water, heating at the microwave oven at 100 ^oC. Further purification by gel chromatography leads to hydrophilic nanoparticles with 2-5 nm core size [98].

The initial motivation for the use of microwave irradiation has been its faster and cleaner methods of synthesis. However it was observed a higher quality of the derived nanoparticles, like increased phase purity, narrower size distribution and lower surface defects, which have led to speculate on the so-called "specific microwave effects" [89]. In general this is proposed when the outcome of a reaction in microwave is different from the one produced under conventionally heating.

Microwave effects on the synthesis are still in debate and are subject of controversy [99] [100] [101] [102] [103]. It is uncertain whether the unique outcome of nanoparticles irradiated by microwave derives from genuine effects of the dielectric heating mechanisms or by misinterpretation of experimental evidences [104], in particular when domestic microwave ovens are employed. Such results are probably due to thermal/kinetic effects, resulting from the more rapid heating rates obtained in a microwave oven. This can clearly be seen when the precursor has high tanδ value, meaning that it can be "superheated", above its boiling point, in a sealed vessel. In addition, using conventional heating, nanocrystals tend to nucleate on the vessel walls, given its inhomogeneous heating profile. In contrast, microwave produces efficient internal heating, creating numerous "hot spots", which could trigger multiple nucleation of seeds throughout the solution, leading to a faster nanoparticle development, and increasing the product yield.

In general, the major drawbacks of microwave synthesis is the equipment cost and the scale up process. The current price for microwave reactors is still much higher than that for conventional heating equipment. This fact limits its full penetration in academic laboratories around the world. Such drawback is expected to change when the cost drops over the next years. In order to scale up the microwave synthesis it is necessary to fully understand the influence of the electromagnetic field in the reaction, in order to manufacture suitable equipment processing.

2.2.3 Liposomes

Liposomes are spherical self-closed structures, which can entrap the surrounding solvent. Their size varies from 20 nm to several micrometers, while their thickness is around 4 nm. The bilayer is made by phospholipids, which have a hydrophilic head and a hydrophobic tail on the same molecule. When these phospolipids are in contact with water, the hydrophilic part tends to be in contact with the water molecules while the hydrophobic part tends to hidden from it. These liposomes can be loaded with polar and nonpolar substances, which triggers an interest for different applications, such as drug delivery and medical diagnostics. Phosphatidylcholines are the most widely used lipids in liposomes works, being Dipalmitoylphosphatidylcholine the one used on this thesis (figure 2.12). This liposome system is called liquid crystal, where the phases change with temperature, characterized by orientational order. Neutral liposomes are not stable (without surface modification), with time they aggregate, fuse and precipitate but charged bilayers are generally more stable.

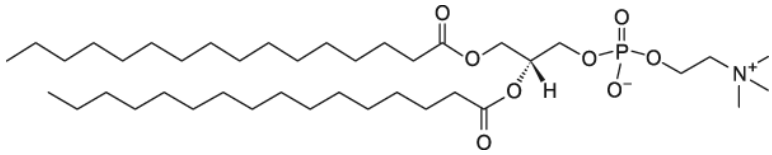

Figure 2.12: Dipalmitoylphosphatidylcholine (DPPC) molecule.

Some forces (intermembrane) are responsible for the formation of the liposomes itself, predominantly these four: attractive Van der Waals, repulsive electrostatic, hydration and steric, which are also repulsive in the bilayer [105]. Van der Waals forces exist between nonpolar molecules, being responsible for the attraction of hydrocarbon chains inside a bilayer, also known as London dispersion force, it decreases quickly with R^{-6}. The electrostatic forces are only present when the surface charge is nonzero and decayes with R^{-2} (can be calculated by Poisson-Boltzmann equation). Hydration forces are responsible for the stability of non-charged liposomes, given the repulsion caused by the bound water molecules, having a short range < 4 nm, rising exponentially upon approaching. Steric forces may originate from

interaction of pure contact, also known as excluded volume .

Stability of liposomes depends on a great extent on temperature. Thus, apart of the melting temperature there is a lipid pretransition, a low enthalpy change below the melting temperature (T_M) of lipid membranes [106]. Below the pretransition and above the main transition, the membrane surface is planar, while for the interval between pre- and main transition, periodic ripples on the membrane surface appears. Multilayers liposomes display a pretransition, while for unilamellar liposomes it usually disappears. For temperatures below the pre-transition, the lipid molecules are in the gel state, organized in a triangular lattice (figure 2.13). At the melting transition, this crystalline order is lost and the lipid chains become fluid and disordered. For DPPC lipids the main transition is at around 41.4 ^oC.

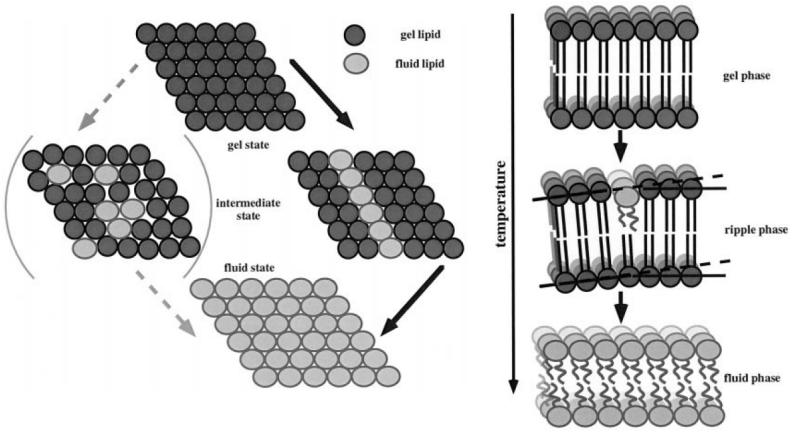

Figure 2.13: Triangular lattice during the melting process and on the right lipid monolayers going from the gel state to a fluid phase through increasing the temperature. Reproduced from [106].

The incorporation of the magnetic nanoparticles in liposomes are used for targeting a specific location of the body by an external magnetic force or to promote drug release by changing the magnetoliposome permeability by the application of an alternating magnetic field. Theoretical studies suggest that the maximum size of a NP that can be incorporated into a liposome while maintaining a lipid bilayer structure is $\sim$ 6.5 nm [48]. Above this size, micellar structures are more energetically favorable due to high local curvature strain within the

bilayer [107]. To embed NP within lipid bilayers, they must present a hydrophobic surface, as it was reported for 5 nm iron oxide nanoparticles [45], [39] or for 7 nm iron oxide nanoparticles [108], [50], [109]. Also around 3 to 6 nm gold and silver nanoparticles were stabilized inside the lipid bilayer [110], [111] and [112]. In the case of the 6 nm NP embedded in the bilayer the melting transition temperature changed from 40.4 ^oC to 38.8 ^oC, which indicates that the NP were interacting with the bilayer [112]. Also it is suggested that DPPC bilayers can be distorted to accommodate bigger particles ($>$ 7 nm) and that this distortion reduces lipid ordering [112]. Ideally the melting temperature should be above 40 degrees for biomedical applications, since the cargo-release before arriving at the desired location is not desirable.

2.3 Interactions Nano-Bio and applications

It was observed that hydrophobicity, size and surface charge are the main parameters influencing nanoparticle biocompatibility [113]. Hydrophobic nanoparticles are rapidly removed from circulation by the reticuloendothelial system (RES). As for the particle size the kidneys can excrete particles smaller than 8 nm while the liver and spleen can trap particles larger than 200 nm. Nanoparticles in size range from 10 nm to a few hundred nanometers can undergo passive accumulation at tumor sites through the enhanced permeation and retention (EPR) effect. The EPR effect is based on the following pathophysiological characteristics of solid tumors: hypervasculature, incomplete vascular architecture, secretion of vascular permeability factors stimulating extravasation within the tumor, and little drainage of macromolecules and particles [7].

The nanoparticle surface will interact with the biological media, given the amount of salts and multivalent ions, surfactants and organic matter as proteins present in it. One of the most cited interaction between nanoparticles and biological media is the formation of protein corona [114] [115], which could mediate the cell uptake, its biodistri-

bution and fate. Various proteins are known to form complexes with nanoparticles, that could depend on the particle composition, but the one that bind most strongly to iron oxide particles and liposomes is albumin, which could promote the phagocitosis by the cell when done deliberately, maybe minimizing the adverse effects caused by immune activation [116]. Also some studies indicates that the spontaneous formation of protein corona can cause an increased aggregation state of these iron oxide nanoparticles [117] [115] [114] [116]. Much ongoing debate is reported on how to control and understand this interactions *in-vitro*, but even more is the debate for the *in-vivo* experiments.

Particle uptake by the cell membrane requires specific and nonspecific binding interactions which must overcome the resistive forces that hinder this process. One of the most effective interaction is the receptor mediated endocytosis, where the nanoparticle surface ligands interact with molecules or receptors present on the cell membrane. Phagocytosis occurs primarily in specialized cells as macrophages. After internalization the nanoparticles are found in lysosomal compartments [118]. Nanoparticles interaction with cell membranes and its cellular uptake is dependent on the chemical functionality of its surface, along with its size and shape [119]. Neutral charged nanoparticles have reduced cellular internalization when compared to negative and positively charged nanoparticles [118]. Positively charged nanoparticles are most effective in crossing cell-membrane barriers but at expenses of a higher cytotoxicity effect due to oxidative damage (ROS) [120].

The interactions between liposomes and cells are usually by surface adsorption or binding of liposome bilayer with cell bilayer [121] [116]. Adsorption can be specific (assisted by targeting ligands such as antibodies) or nonspecific (controlled by intermolecular and surface forces) (figure 2.14). After this bound the liposomes can be internalized by endocytosis which involves the uptake of liposomes into the cell by encapsulation within endosomes [105]. Release of drugs to the cytoplasm can occur by membrane destabilization of the encapsulating endosome or by delivery to lysosomes. Lysosomes have an acidic pH and contain lysing enzymes. Drug release is accomplished when lysosome enzymes hydrolyze the lipid bilayer releasing the drug. Lysosome drug release is only effective when the encapsulated drugs are not susceptible to

lysosome enzymes and pH. Alternative to endocytosis is the fusion, that involves the adsorption and incorporation of the liposome bilayer with the cell membrane, releasing the payload into the cytoplasm [122]. Finally, lipid transfer involves the exchange of lipids between the liposome bilayer and the cell membrane without enveloping the liposome [123].

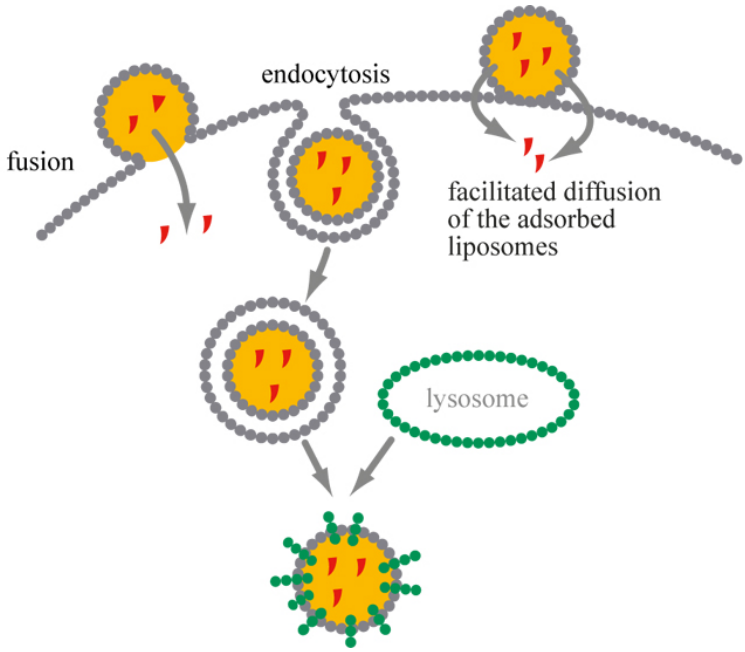

Figure 2.14: Cell uptake mechanisms for liposomes, such as adsorption, endocytosis and fusion. Image designed by Shirinsky Vladimir P.

2.3.1 MRI contrast agents

It is an imaging technique used in radiology to obtain detailed anatomical information of soft tissues, and in particular to the brain showing the active areas while it is doing different tasks (functional MRI). An advantage of MRI compared with other imaging techniques is the fact that it does not use ionizing radiation. Consequently, it is suitable for use with children and pregnant women. Magnetic nanoparticles can be used in this case as a contrast agent, enhancing the contrast in the image obtained, allowing the identification of tumors more precisely or in early stages [14].

MRI uses the magnetic spins of the protons in water molecules. In the absence of an external field the magnetic moments of the protons in water molecules are randomly orientated, thus providing a zero net magnetic moment. When an external magnetic field is applied, the individual proton magnetic moments align either parallel or anti-parallel to this field. However, the proton magnetic moments are not static in the field but are precessing, which have equal frequencies but random phases so that the transverse magnetization (M_T) is zero (for the system), and the overall magnetization is purely longitudinal (M_L).

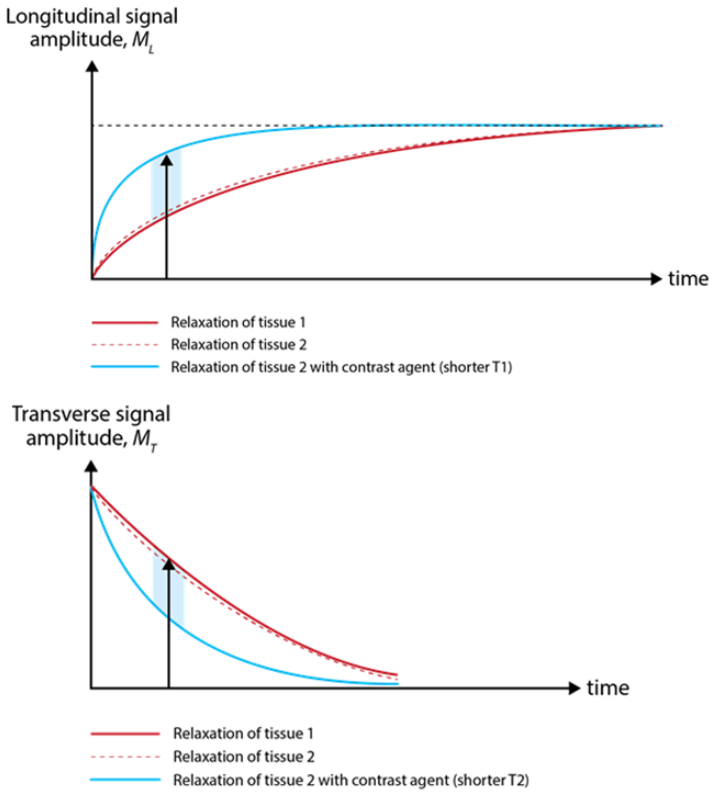

Figure 2.15: Shortening of T_1 and T_2 signals using contrasts agent. The vertical black arrows represents an appropriate time where significant contrast (cyan shading) in signal is observed. Kindly provided by [65].

In order to achieve a non-zero value of transverse magnetization, a second external magnetic field is applied, an alternating radio frequency perpendicular to the first applied field, matching the precession frequency. This cause a rotation of the overall magnetization, where

the rotation degree is controlled by the value of perpendicular field and the duration of the pulse. When the radio frequency pulse is switched off, the energy that was absorbed by the protons is transferred from the system via two independent processes known as longitudinal (T_1) and transverse (T_2) relaxations (figure 2.15).

The essence of MRI is that if two tissues in the body have different values of T_1 or T_2, then measurement of the magnetization at suitable time intervals can differentiate between the two tissues. To differentiate structures on MRI scans it has to produce distinct signals, as for example, protons density affects the signal strength, so the greater the concentration of water molecules in a tissue, the greater is the signal. As an example, fat has a short T_1 relaxation so it appears bright on a T_1 weighted image. On the other hand, water has much longer T_1 relaxation, having low signal and appears dark in the image. To differentiate between tissues with similar values of T_1 it is used contrast agents that being distributed differently in those tissues will shorten T_1 values differently. The same is applied to T_2 contrast agents (figure 2.15).

The efficacy of a MRI contrast agent is commonly evaluated in terms of its relaxivities r_1 and r_2 defined as the rates at which the excited solvent nuclei (protons) relax to regain their initial equilibrium state. They are determined from the linear relationship $1/T_{i,obs} = 1/T_{i,dw} + r_i$ [A] (measured H^1 relaxation time, $T_{i,obs}$; water diamagnetic constant, $T_{i,dw}$; contrast agent concentration, [A]) and are then expressed in s^{-1} per contrast agent concentration. Relaxivity r_1 is related to the spin-lattice relaxation process, the excited nuclei giving off their energy to the surrounding environment. Relaxivity r_2 characterizes the spin-spin relaxation process through which an excited nucleus exchanges its energy with a low-energy one. MRI contrast results from the difference between r_1 and r_2 values. In the case of T_2-agents, which accelerate the spin-spin relaxation process, the higher is the r_2 to r_1 ratio, the better is the agent's effectiveness.

Paramagnetic metallochelates, principally gadolinium derivatives, have received particular attention. They typically behave as T_1 contrast agents, which cause positive contrast enhancement and provide

brighter images where they are accumulated. Besides, particle systems based on superparamagnetic iron oxide or ultra small paramagnetic iron oxide have emerged as T_2 contrast agents, which permit negative contrast enhancement and thus darker images of the regions of interest. To use magnetic nanoparticles as contrast agents (usually as T_2), they must reach the target tissue and stay there long enough for the procedure to be performed and also follow the treatment. For that it must be small enough to pass through the vascular capillaries and large enough to have a high magnetic moment per particle. Iron oxide nanoparticles are good for imaging liver metastases for example, since it is known they are collected by the liver and the spleen in healthy areas but excluded in tumoral ones [8].

2.3.2 Hyperthermia

According to the National Institute of Health, "Hyperthermia" is a type of cancer treatment in which body tissue is exposed to high temperatures (reaching a maximum of 45 ^oC). The idea in the case of magnetic hyperthermia is to use magnetic nanoparticles under an alternating magnetic field to heat specific regions of the body with tumor tissue (figure 2.16).

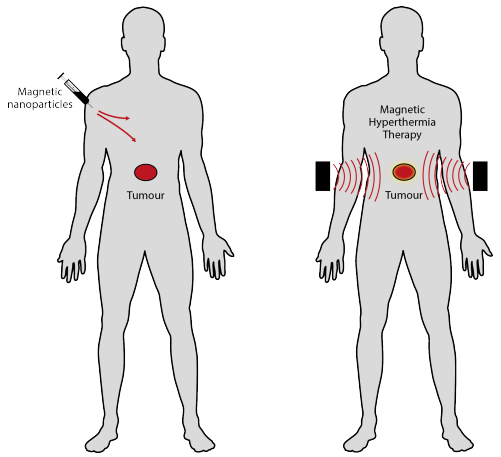

Figure 2.16: Cancer treatment based on magnetic hyperthermia where magnetic nanoparticles are injected in the body and placed under an alternate magnetic field, heating specific tumor tissues. Kindly provided by [65].

The heat comes from the two different mechanisms: Néel and Brownian relaxation (see section 2.1). The first system releases heat given the impossibility of the magnetic moments to follow the changes in the direction of a magnetic field (equals to the area inside the hysteresis) and the second system releases heat from friction between the nanoparticle and the media.

The increase in temperature can lead to cell death of basically two types: necrosis, characterized by cellular lysis followed by an inflammatory response or another type called apoptosis, characterized by a programmed death, triggered by genetically controlled cellular signals [124]. These distinct mechanisms are triggered depending on the temperatures applied (figure 2.17). Apoptosis is considered more benign given its elimination by phagocytes, avoiding the impact on surrounding cells.

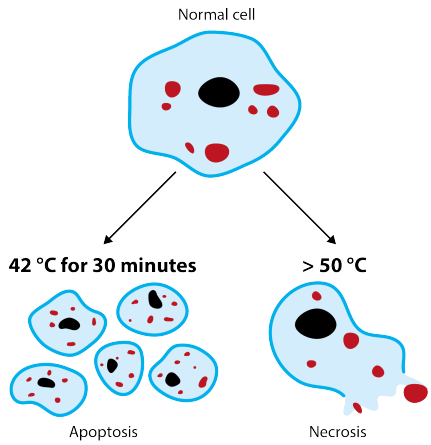

Figure 2.17: Cell death by apoptosis or necrosis, being triggered by magnetic hyperthermia. Kindly provided by [65].

In 2002, Rosensweig developed the linear response theory (LRT) to explain the heating of colloidal magnetic fluids subjected to an alternating magnetic field [125]. From this theory the expression for the power dissipation (P) was derived as follows:

$$P = \mu_o \pi \chi" f H^2 \tag{2.6}$$

where, H and f are the amplitude and frequency of the AC magnetic field, respectively, μ_o represents the permeability of free space, and χ" is the out-of-phase component of the colloidal magnetic fluid AC susceptibility,

$$\chi" = \frac{\omega\tau}{1+(\omega\tau)^2}\chi_o \tag{2.7}$$

where, $\omega = 2\pi f$, χ_o is the equilibrium susceptibility and τ is the effective relaxation time which was already seen as dependent on the collective contributions of both Néel and Brownian relaxation processes.

Substituting the values of χ" in the power dissipation expression gives,

$$P = \mu_o \pi \chi_o f H^2 (\frac{2\pi f\tau}{1+(2\pi f\tau)^2}) \tag{2.8}$$

evidencing the dependence of the heat generation process with the frequency and amplitude of the applied AC field, and the magnetic relaxation processes.

To represent the heating efficiency of a material, it is used a specific loss power (SLP), which is most known as specific absorption rate (SAR),

$$SAR = SLP = \frac{P}{m_{NP}} \tag{2.9}$$

where m_{NP} is the mass of the magnetic nanoparticles. This value has a drawback since it is dependent on H^2 and f, hindering the comparison between reported literature values, given that every laboratory has its own equipment with variations in the applied AC field conditions. At chapter 3 the experimental method to obtain specific absorption rate values is described. The temperature measurements should be done under adiabatic conditions that are ensuring the thermal insulation of the object.

By the LRT model, the heating efficiency is proportional to the saturation magnetization of the magnetic nanoparticles, but the optimum nanoparticle size and crystalline anisotropy also depend on the strength and frequency of the applied AC field.

To apply magnetic nanoparticles clinically some safety rules must be followed. For example, the application of intense alternating fields may lead to serious side effects in healthy tissues, as heating by inductive eddy-current, arrhythmia or stimulation of nerves and skeletal muscles [8]. One of the main challenges in being able to deliver an adequate quantity of the magnetic particles to generate enough heat in the target using magnetic field conditions that are clinically acceptable. These safety limits, named as Brezovich criterion, is where the product $H \times f$ is below $4.85 \times 10^5\ kAm^{-1}s^{-1}$, where H is the field amplitude (current $\times$ number of coils per length) and f is the frequency, these factors are expected to reduce eddy current heating [126]. Also for the nanoparticles administration in clinical trials, the used method is by intra-tumoural direct injection.

A solution would be to combine the heating efficiency of magnetic nanoparticles to liberate drugs on a specific target in the body, using for example the magnetoliposomes.

2.3.3 Drug delivery systems

Modern medicine is focused on increasing the drug efficiency while diminishing its side effects, influenced also by the patents expiration dates, which boosted the search for novel forms of drug delivery systems. Figure 2.18 shows an example of free drug administration versus a specific site drug delivery, which can reduce toxic and unwanted side effects. Current applications to treat cancer are non-specific drug delivery which require a high concentration of the drug in the tumor tissue, leading to side-effects in the whole body [7]. Some advantages of using a targeted drug delivery are the reduction in the dosage required to achieve the same effect as free drug administration, reduction of possible toxic side-effects, prevent the administration in other tissues or regions of the body and a prolonged release of the drug.

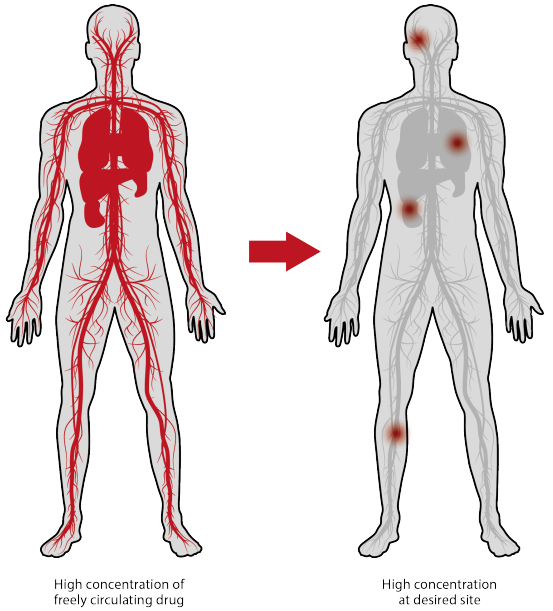

Figure 2.18: Free circulating drug *vs* targeted drug delivery, altering efficiency and reducing possible side effects. Kindly provided by [65].

To overcame this challenge a extensively studied drug carrier is the liposome, given its physicochemical properties, even in spite of its disadvantages like stability, sterilization and small scale production. It can be targeted to specific sites in the body by the conjugation of a special surface ligand [24] [127] [128]. Liposome can also escape the uptake by macrophages from the reticuloendothelial systems and other tissues.

Finally, by introducing also magnetic nanoparticles combined with the drug into the liposome, it is possible to monitor its biodistribution using for example MRI.

Many drugs have been encapsulated in the liposomes for treating cancer, being in Phase I/II or even approved by the FDA [129]. Doxorubicin, being approved for medical use in the United States in 1974 for cancer treatment, was chosen in this thesis as a case model [130]. The exact mechanisms of action of doxorrubicin are complex but it is known that it intercalates into the double-stranded DNA and blocks

the replication and transcription of the genetic material. In addition, mitochondrial activity decreases and potentiates the formation of free radicals, with the consequent oxidative damage (ROS). The dose administered must be carefully evaluated in each patient, since it can induce several adverse effects in different organs including the heart, brain, liver and kidney which came to question its clinical use [130] [58]. A particular advantage of doxorubicin is that it has a broad spectrum of absorption with a peak at 500 nm which will be used in this thesis to measure its release.

The encapsulation of DOX in liposome formulations are in clinical trials and approved by health regulatory agencies, such as the FDA as seen in the Introduction chapter . In fact there is no other DOX nanocarrier that has been approved by any regulatory agency [130].

Chapter 3

Materials and methods

This chapter reports detailed materials and procedures followed to perform the experiments carried out in this thesis. Three methods of magnetic nanoparticle synthesis have been used and presented: (1) co-precipitation of iron (II) and (III) from aqueous solutions, commonly employed in the industry; (2) Thermal decomposition of organometallic iron precursors at high temperatures to gain crystallinity and homogeneity and (3) adaptation of method (2) to the use of microwave heating newly developed for this thesis. Then, it was carried out the superficial modification of the nanoparticles and finally its encapsulation in liposomes, that have been also loaded with a drug, doxorrubicin. Subsequently all the structural, colloidal and magnetic characterization of nanoparticles and magnetoliposomes are presented. By the end of the chapter the experimental procedures for the citotoxicity assessment and evaluation of the nanosystems for several biomedical applications are described.

3.1 Synthesis of magnetic nanoparticles

3.1.1 Coprecipitation

Magnetite (Fe_3O_4) nanoparticles were synthesized by the coprecipitation method [119]. To obtain 14 nm particles, 425 mL of a mixture of $FeCl_3.6H_2O$ (0.09 mol) and $FeCl_2.4H_2O$ (0.054 mol) was added slowly (0.2 mL/s) in 75 mL of NH_4OH solution. The mixture was heated at 90 ^oC for 3 h. After the synthesis the particles were washed three times with distilled water with the help of a permanent magnet. A standard protocol was used to oxidize magnetite to maghemite ($\gamma - Fe_2O_3$) and to activate the particle surface for further coating. Briefly, 300 mL of HNO_3 (2 M) was added to the particles, and the mixture was stirred for 15 min. Then, nitric acid was removed by magnetic decantation, and 75 mL of $Fe(NO_3)_3$ (1 M) and 130 mL of water were added to the particles. The mixture was heated up to boiling temperature and stirred for 30 min. The particles were then cooled to room temperature, and by magnetic decantation, the supernatant was substituted by 300 mL of HNO_3 (2 M) and stirred for 15 min. Finally, the particles were washed three times with acetone and redispersed in 10 ml of water.

3.1.2 Thermal decomposition

To produce the precursor which will be used both in thermal decomposition and microwave synthesis (solid iron oleate), first it was added sodium hydroxide (5.91 g) and oleic acid 90 % (43.6 g) to 140 ml of hexane and heated the mixture up to 60 ^oC in an oil bath, with magnetic stirring at 400 rpm. After one day at 60 ^oC, a white precipitate of sodium oleate that is dissolved by adding 80 ml of ethanol at the same temperature appears. Then 10.8 g of $FeCl_3$ in 80 ml of distilled water is added and the solution boils violently at 57 ^oC. The system is heated for 2 hours more, and then it is chilled with a cold water bath.

The denser aqueous phase was eliminated by decantation using a separating funnel; the upper organic phase was filtered with filter paper prior to the precipitation of the solid iron oleate by the addition of an equal volume of methanol. The orange solid iron oleate was redissolved in hexane and reprecipitated with methanol three times. Finally it was dried over P_2O_5, milled gently, and stored at room temperature in a desiccator over silica gel. For comparison, a liquid oleate was prepared following a methodology previously reported [131] [132] [133].

For the synthesis of 12 nm nanoparticles a mixture containing 0.9 g of solid iron oleate, 4.5 g of oleic acid and 50 ml of Dibenzyl Ether was added on a three-neck round-bottom flask mounted on a temperature-controlled N_2 reflux system, stirred mechanically at 100 rpm until reach 100 ^oC. The temperature was increased in a controlled way, with a heating ramp of 3.75 $^oC/min$ until reflux temperature (boiling point of the solvent 290 ^oC), this temperature was maintained for 1 hour. For obtaining 15 nm nanoparticles the same quantities were used with the difference being the substitution of Dibenzyl Ether for 50 ml of Octadecene, that has a higher boiling point, 320 ^oC. The sample was washed with ethanol, centrifuged at 7000 rpm for 15 min about 5 times, until the supernatant was clean, and resuspended in 10 ml of toluene.

These quantities and heating ramps were tested considering the group experience in synthesis, as for example in [133].

3.1.3 Microwave-assisted

The synthesis of magnetic nanoparticles was carried out using a microwave oven Monowave 300 produced by Anton Paar GmbH, Austria, working on 2.45 GHz. Different parameters were explored in the synthesis of oleic acid coated iron oxide nanoparticles by microwave heating such as the nature of the solvents with different dielectric constant (octadecene, dibenzyl ether, benzyl alcohol, phenyl ether, and dimethyl sulfoxide (DMSO)), the Fe concentration, and the heating ramps (2–4 $^oC/min$). The reaction mechanism was also explored fixing all the experimental conditions and varying the reaction time from 1/2 h up to 4 hours. Finally, two microwave samples were prepared

under selected conditions as follows: a mixture containing 0.15 g of solid iron oleate, 0.76 g of oleic acid, and 8.32 ml of dibenzyl ether (7 nm nanoparticles) or benzyl alcohol (8 nm nanoparticles) was stirred at 600 rpm, while the temperature increases at 3.75 $^oC/min$ until 250 ^oC and then was maintained at this temperature for 1 hour. This conditions were tested given the results from thermal decomposition synthesis and previous results on microwave synthesis [98]. The sample was washed with ethanol, centrifuged at 7000 rpm for 15 min about 5 times, until the supernatant is clean, and resuspended in 10 ml of toluene.

3.2 Surface modification

When the particles are synthesized by the thermal decomposition or microwave-assisted methods described above, their surface is covered with oleic acid, not being suitable to use in biomedicine. For that matter this nanoparticles were transferred to an aqueous medium by exchanging the oleic acid of the surface by dimercaptosuccinic acid (DMSA) (figure 3.1 A). For that purpose a solution of 20 ml of Toluene containing 50 mg of nanoparticles were added to a solution of 90 mg of DMSA in 5 ml of dimethyl sulfoxide [134] [119]. The resulting suspension was then gently stirred for at least 2 days, until the nanoparticles stay attached to the glass wall and the suspension became transparent. The resulting nanoparticles were washed with ethanol and centrifuged at 7500 rcf, at least 3 times. The final black solid was air dried and redispersed in distilled water. $NaOH$ was added to increase the pH up to 10. The dispersion was then placed in a cellulose membrane tube molecular weight cut-off (MWCO) 10000 Da and dialyzed for 3 days in distilled water, to remove any excess of unreacted DMSA. Finally the pH of the dispersion was adjusted to 7 and the dispersion filtered through a polyethylene oxide filter with a pore size of 0.22 μm. This avoids bacteria or dust in the final dispersion, being sterilized by this procedure, when done inside a laminar flow cabinet.

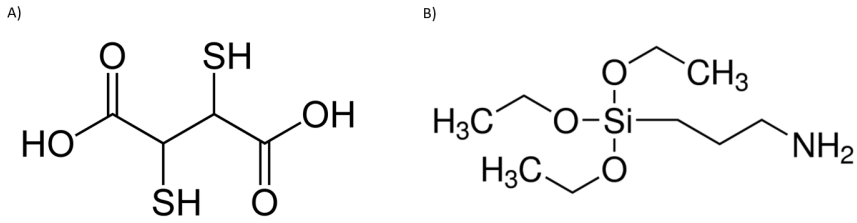

Figure 3.1: A) Dimercaptosuccinic acid (DMSA) molecule. B) Aminopropyl triethoxysilane (APS) molecule.

When the particles are synthesized by coprecipitation its surface was first activated by acid treatment and further surface modification for positive coating was performed by slowly adding 1.22 mL of 3- aminopropyl)triethoxysilane (APS, 10 $\mu L/s$, 0.005 mol) (figure 3.1 B) to a mixture of 10 mL of particles (28 g Fe_2O_3/mL) and 10 mL of methanol, maintaining rigorous stirring for 12 h [119]. After that, methanol was eliminated in the rotary evaporator, and rest of the APS was eliminated by dialysis, to achieve the final APS coated nanoparticles. To modify the surface for negative coating 14.68 mg of DMSA were dispersed in 10 ml of distilled water, which was then added to 20 ml of particles (5 g Fe_2O_3/mL) at pH 3. By gentle stirring the pH was elevated to 11 using NaOH, the dispersion was then placed in a cellulose membrane tube MWCO 10000 Da and dialyzed for 3 days in distilled water, to remove any excess of unreacted DMSA. Finally the pH of the dispersion was adjusted to 7 and the dispersion filtered through a polyethylene oxide filter with a pore size of 0.22 μm.

3.3 Synthesis of liposomes

Liposomes were prepared by a thin-layer evaporation method [135] using 1,2-Dipalmitoyl-sn-glycero-3-phosphocholine (DPPC) (figure 3.2). Lipids (10 mg) were dissolved in 5 mL of chloroform, inside a round bottom glass flask of 50 ml, the mixture was left to hydrate for 20 minutes. The solvent was removed by rotary evaporation for 1 hour under vacuum at 50 ^oC. Then, the dried lipid film was hydrated with 5 mL of distilled water at 55 ^oC (the temperature of the medium should

be above the crystalline transition temperature of the lipid) [106]. The product of this hydration is a large multilamellar vesicle (LMV). To break these structures, it is necessary to sonicate the mixture at 55 ^oC for 1 hour, producing small unilamellar vesicles (SUV), with diameters up to 200 nm (the presence of some LMV cannot be discarded) [136]. The dispersion was then placed in a cellulose membrane tube MWCO 10000 Da and dialyzed for 2 days in distilled water. Finally, the pH of the dispersion was adjusted to 7 and the dispersion filtered through a polyethylene oxide filter with a pore size of 0.45 μm.

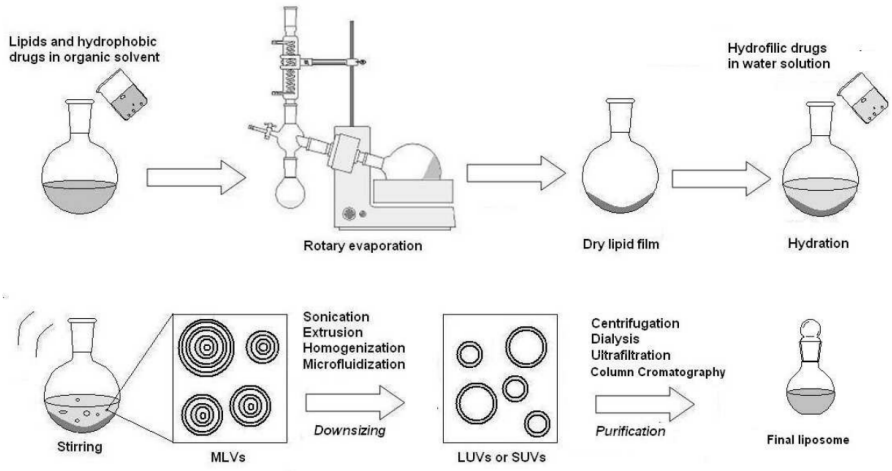

Figure 3.2: Liposome production by thin-film hydration followed by sonication to break large multilamellar vesicle (LMV) into small unilamellar vesicles (SUV). Reproduced from [137].

To produce magnetoliposomes with hydrophilic nanoparticles the process is analogous to the previous one, where 5 mg of the nanoparticles are dispersed with 5 mL of distilled water, used to hydrate the dried lipid film. To produce magnetoliposomes with hydrophobic nanoparticles, 5 mg of nanoparticles are dispersed with the 5 mL of chloroform at the beginning of the process (figure 3.2).

To synthesize liposomes loaded with drugs the process is analogous to the production of magnetoliposomes, where the main drug characteristic to be taken into account is its polarity, whether the drug is hydrophilic (Doxorubicin for example) or hydrophobic (Zinc phthalocyanine for example) (figure 3.2). As the drugs may be photosensitive

the processes of synthesis in both cases have to be made in the dark (with everything covered by aluminium foil). To produce liposomes with Doxorubicin, 2.5 mL (100 μM) were added to 2.5 mL of distilled water, used to hydrate the dried lipid film.

For comparison three other methods for the preparation of liposomes were tested: ethanol injection, freeze-thaw sonication and a commercial method by NanoVex Biotechnologies S.L. (LipoCat), that claim to produce liposomes by adding water to the lipid mixtures provided in sealed vials and hand shaking. For the ethanol injection method, 10 mg of dry DPPC was dissolved in 1 ml of ethanol and injected into 5 ml of distilled water at 55 ^oC, very slowly, at a rate of 5 ml/h. For the freeze-thaw sonication method, the lipid (10 mg of DPPC) is directly hydrated with the aqueous solution. This suspension is rapidly frozen with liquid nitrogen, followed by bath sonication at a temperature above the crystalline transition (55 ^oC). This cycle is repeated at least 15 times for greater homogeneity and destruction of the LMV. In this case, for nanoparticle loading the nanoparticles are added directly in the aqueous solution, independent of its polarity (5 mg). For the commercial method cationic liposomes were tested, named LipoCat, which are a ready-to-use formulation, only by adding an aqueous solution and posterior sonication of the mixture at 55 ^oC. In this case the hydrophilic nanoparticles (5 mg) were added with the distilled water.

3.4 Structural characterization

3.4.1 Microscopy

3.4.1.1 Transmission Electron Microscopy

This technique facilitates direct imaging and chemical analysis of samples with nanometer resolution and it is used in this thesis to know the core sizes, morphology, crystallinity and aggregation state of the nanoparticles.

A beam of high-energy electrons is focused on a very thin sample where it passes through, data being obtained from the detection of electrons transmitted through the sample (figure 3.3). The electrons are generated by thermionic effect in a filament, usually of tungsten, being needed to operate under high-vacuum conditions and may damage organic coatings. TEM images are 2D projections of the particles, having for that some limitations. The images were captured at a 100 keV JEOL-JEM 1010 microscope, equipped with a digital camera Gatan model Orius 200 SC, at the Universidad Autónoma de Madrid.

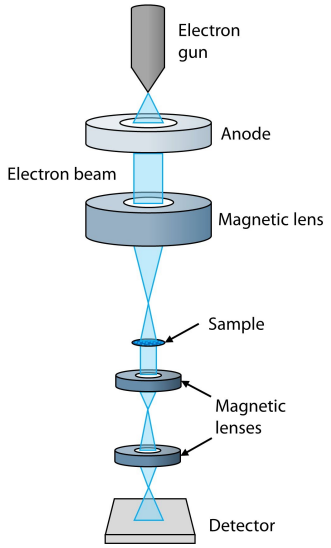

Figure 3.3: Diagram showing a typical setup of a TEM instrument. Kindly provided by [65].

For sample preparation a drop of toluene or water dispersion of nanoparticles was placed on a copper grid coated with perforated carbon film, allowing all the solvent to evaporate at room temperature. For the liposomes a drop of the suspension was placed on a carbon coated copper grid removing the excess by filter paper. To stain the liposomes, a drop of 2 % (w/v) aqueous solution of uranyl acetate was added and left in contact with the sample for 2 minutes. The surplus water was removed and the grid was dried at room conditions. Size distribution were obtained with the open source software ImageJ, counting at least 300 nanoparticles [ISO13322-1]. A log-normal fit was

performed to obtain mean sizes and deviation in number (TEM diameter in number $d = \Sigma x dN/\Sigma dN$), which can be transformed to a volume distribution in order to compare the values with X-Ray Diffraction (XRD) and mean size (TEM diameter in volume = $\Sigma x^4 dN/\Sigma x^3 dN$, where x = particle size and N = number of particles) [138].

In the case of the TEM observations of cells (Pan02 and Jurkat) the cultures were fixed with 2 % glutaraldehyde and 1 % tannic acid in HEPES buffer (0.4 M, pH 7.2) at room temperature (RT) for 2 h. Then, both adherent cell lines were harvested with a cell scraper, centrifuged (301 rcf, 3 min; Pan02 and 409 rcf, 4 min; Jurkat) and maintained in HEPES buffer at 4 ^oC until its processing as described elsewhere [139]. The cells were dehydrated in acetone at 4^oC to include them in epoxy resin that was polymerized for 48 h at 60^oC. Finally ultrafine sections of 60 nm thickness were obtained in an ultramicrotome Leica EM UC6 (Wetzlar, Germany), collected on a carbon coated nickel grid.

3.4.1.2 Cryogenic Electron Microscopy

To observe frozen hydrated sample with intact morphology it is used a technique called Cryo-TEM, suitable for single particles and semi-thick frozen cells, liposomes or sections (up to 200 nm thickness). Integration of tomography in TEM enables the reconstructions of 3D structures of particles with a spatial resolution down to around 1 nm. Main difference between TEM and Cryo-TEM is that in the second case the sample must be first cryo immobilized, then transferred to a cryo holder in liquid nitrogen and finally the holder is introduced inside the microscope, always keeping the sample in a frozen state. A disadvantage of the technique is the high sensitivity of the frozen sample to the radiation, so, the samples are viewed under low dose conditions to avoid electron beam damage. It can give information about the real size, shape and lamellarity of liposomes.

The sample must be frozen extremely rapidly, at a rate of 10^6 $^oC/s$, so that the water inside and surrounding the liposome is fixed in a vitreous state. If freezing occurs too slowly crystalline ice is formed,

which compromises the structural integrity of the sample. To acquire such images it was used a 200 kV FEI Tecnai G2 equipped with a CCD camera and a FEI Vitrobot to prepare the grids. Grids for Cryo-TEM are made of Holey Carbon Film (QUANTIFOIL®), which is a perforated support foil with circular holes. Liquid ethane is cooled at $-180\ ^oC$ by liquid nitrogen. Inside the Vitrobot equipment a drop of 3 μl of sample at 0.05 mg DPPC/ml concentration is put in contact with the grid for 15 seconds. The grid is blotted using filter paper for 3 seconds which is then immersed into the liquid ethane. After immersion, the grid must be kept under liquid nitrogen until its use.

3.4.1.3 Optical Microscopy

The routine observation of cell cultures during maintenance, as well as the effect of different treatments are done by optical microscopy. Observations of cell samples were made with an Olympus BX61 epi-fluorescence microscope equipped with an Olympus DP50 digital camera (Olympus, Center Valley, PA, USA). In the case of living cells, a differential interference contrast (DIC) inverted microscope (Leica DMI6000B) equipped with a Leica DFC420 C digital camera (Leica Microsystems, Heerbrugg, Switzerland) was employed.

3.4.1.4 Confocal Microscopy

It is a system designed for scanning fluorescence marked living and fixed specimens. Present lateral resolution up to 0.14 μm. Nanoparticles coated with APS loaded-Jurkat and Pan02 cells adhered to poly-L-lysine coated coverslips were fixed with 4 % PFA, permeabilized with 0.5 % Triton-X100 in PBS and stained for plasma and Golgi membranes with WGA (1:200, W-11262, Life Technologies) and for tubulin (1:200, T4026, Sigma Aldrich). Images were taken on a Leica TCS SP5 confocal microscope with a 63 x 1.4 oil objective and x3 zoom. The samples were excited with laser light at 561 nm and NP were detected by reflection. Images were processed with ImageJ.

3.4.2 X-Ray Diffraction

This is a technique based on the elastic scattering of X-rays by the atoms within a sample, allowing the determination of the crystal structure. The X-ray beam is usually generated by a copper anode and typically carried out on solids or powders. When an incident beam interacts with a sample it is elastically scattered by planes of atoms (or molecules/ions) separated by a distance d. The difference in path between two diffracted waves by adjacent parallel planes is $2dsin\theta$ (figure 3.4).

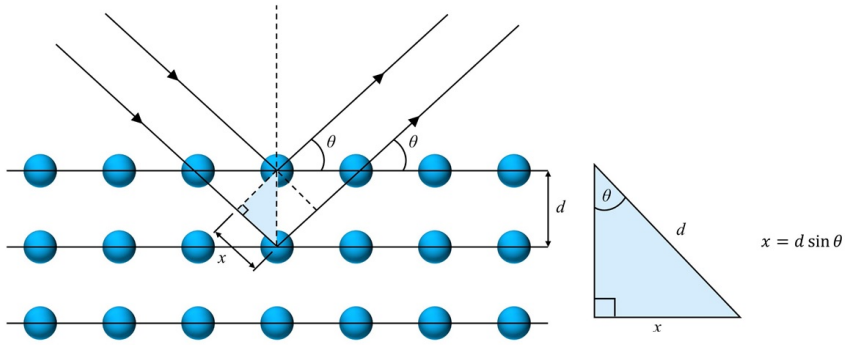

Figure 3.4: Diagram showing an incident beam interacting with a sample, being elastically scattered by planes of atoms separated by a distance d. Kindly provided by [65].

To produce a diffraction peak, constructive interference must occur, that is when both waves are in-phase. This condition happens when the difference in path is equal to an integer multiple n of the wavelength λ, in other words $2dsin\theta = n\lambda$, being this the Bragg's law [140]. Each peak occurs at an angle θ corresponding to a different separation of planes d in the crystal. Analysis of the position, intensity and width of the peaks obtained from the diffraction pattern enables a comprehensive crystallographic assessment of the particles, being possible to determine the structure, composition and NP size of the sample. Comparing XRD patterns with databases of already known materials enables the identification of the phases present in the sample.

In this thesis, the iron oxide phase was determined by X-ray diffrac-

tion on a Powder Diffractometer Bruker D8 Advance, at the Institute of Material Science of Madrid, with Cu$K\alpha$ radiation ($\lambda = 1.5406$ $\mathring{A}$) with energy-discriminator detector (SolX), in 2θ ranging from 10 to 90 degrees, with acquisition time of 5 seconds using 0.05-degree step. Crystal sizes were calculated by the width of the peak with the greatest intensity (311) reflection of the spinel struture, using the Scherrer equation. The calculations were made using the APD (Phillips) computer program and the instrumental error in the crystal sizes obtained by use of the Scherrer's equation is estimated to be ± 0.1 nm, which is related to the small broadening produced for the samples in comparison to the instrumental line width ($\Delta 2\theta = 0.11$ ^{o}), being the real uncertainty of the measurements of approximately 1 nm determined by the uncertainty of the determination of peaks broadening.

3.4.3 Infrared Spectroscopy

This technique allows the characterization of the functional groups contained in the coatings of the different nanoparticles and also the core iron oxide phase. The chemical bonds in the molecules have specific vibration frequencies, when this molecules are subjected to infrared radiation its dipole moment changes and energetic transitions take place. This change of energy due to the energetic transitions produces changes in the modes of vibration and rotation of the molecules. Each type of bond between atoms vibrates in different modes producing characteristic bands in the spectrum.

The apparatus used in this thesis for recording the fourier transform infrared spectroscopy (FTIR) spectra was a Bruker IFS 66VS, to confirm the iron oxide phase, the presence and nature of the coating and its surface bonding. IR spectra were recorded between 4000 and 250 cm^{-1} and the samples were prepared by diluting 2 % wt iron oxide powder in KBr and pressing it into a pellet.

3.4.4 Thermogravimetric and Differential Thermal Analysis

This technique provides the proportion of organic material in a sample from the weight loss that occurs in a solid sample when raising its temperature in a oxidant atmosphere. Knowing the calcination temperatures of the organic compounds it is possible to analyze the nature, the proportion of these coatings and how they are bounded.

Quantification of the coatings was carried out by simultaneous thermogravimetric (TGA) and differential thermal analysis (DTA) of the samples, in this thesis were performed on a Seiko Exstar 6300 instrument. Samples were heated from room temperature to 900 ^oC at 10 $^oC/min$ under an air flow of 100 ml/min.

To evaluate the phase transition temperatures of the liposomes it was used a differential scanning calorimeter (DSC) MicroCal VP-DSC (MicroCal LLC, Northampton, MA, USA) with a cell volume of 0.514 ml, where the reference cell is filled with water. The heat flow between cells has been explored with an temperature increase rate of 1 ^oC per minute, and the temperature range covered was from 15 ^oC to 75 ^oC.

3.4.5 Inductively Coupled Plasma Mass Spectrometry

This is an analytical technique used to determine the elemental composition or concentration of specific analytes at the trace level, allows determination of around 70 elements up to the atomic number 83 (Bi). Samples are analyzed in a liquid state, so solid samples must be dissolved (digested) prior to the analysis. The sample is transported to an inductive coupling plasma where it is nebulized into micrometre size droplets and its temperature raised to 10000 K, where the atoms are partially ionized or highly excited. The photons emitted by the elements when relaxing their energy are recorded through an optical spectroscopy system where their energy and intensity are analyzed. By those peaks it is possible to quantify the quantity and proportion of

each of them.

In this thesis, iron determination was carried out by Inductively Coupled Plasma – Optical Emission Spectrometry (ICP-OES) using an apparatus from Perkin Elmer, model OPTIME 2100DV. Digestion of nanoparticles and liposomes prior to analysis was done using nitric acid at 90 ^oC for at least 4 hours. The wavelengths used for iron was 238.204 nm with an extra wavelength at 239.562 nm to control the interferences from other elements at the standard wavelength.

3.5 Colloidal characterization

3.5.1 Dynamic Light Scattering

This is a method to determine the mean size and charge of particles in a colloidal system. A laser beam of visible light impacts the sample and the light is scattered by the particles, by measuring the intensity of this light and how it fluctuates over time it can be analyzed the hydrodynamic size, given the nanoparticles Brownian motion. Smaller particles move rapidly while large particles show slower Brownian motion, leading to higher intensity fluctuations in comparison to the large ones (figure 3.5).

The ζ-potential is used to characterize systems in terms of their colloidal stability arising from electrostatic repulsion. It can be determined by using the physical effect of electrophoresis, the movement of charged particles (relative to the liquid it is suspended in) under the influence of an applied electric field. Measuring the velocity of the particles as they move in the electric field the surface charge can be determined, considering also the direction of the movement whether is towards or opposite the field. The liquid layer surrounding the particle is divided in two: an inner region (called Stern layer) where the ions are strongly bound and an outer diffused region where the ions are not firmly attached (figure 3.6). The potential that exist in this boundary (Stern layer) is known as ζ-potential.

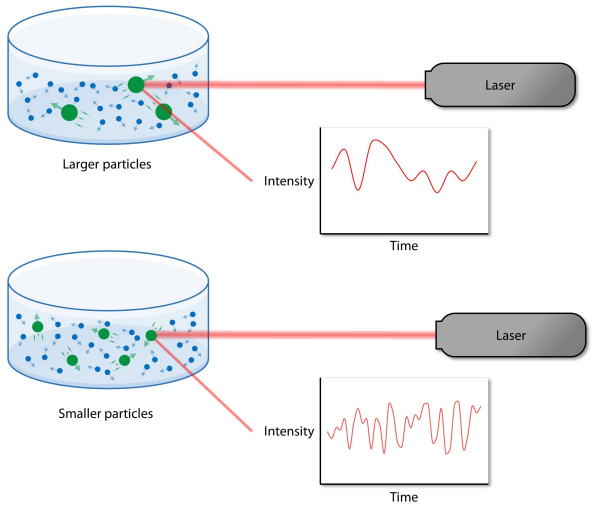

Figure 3.5: Scattered light from nanoparticles of different core sizes. Kindly provided by [65].

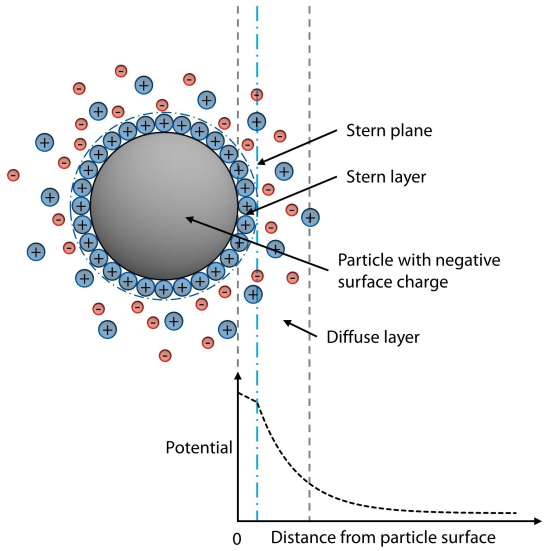

Figure 3.6: Particle's electrical double layer potential. Kindly provided by [65].

In this work, the hydrodynamic diameter of the samples was measured in water at pH 7 in a standard cuvette, using a Zetasizer NanoZS device (Malvern Instruments). A laser emitting green light is the energy source with an angle of 173^o between the sample and detector.

The hydrodynamic size of the particles are expressed in terms of intensity or number. The fundamental size distribution generated is in intensity but it can be converted (using Mie theory [141]) to a number distribution, where it is considered the number of nanoparticles in the mixture, not the light scattered from them. ζ potential was measured as a function of the pH, at room temperature, using KNO_3 (10^{-3} M) as the electrolyte and using KOH and HNO_3 to vary the pH.

3.5.2 Colloidal stability analysis

To monitor the colloidal stability of a sample it is used a TURBISCAN ® Lab (Formulaction), which measures and analyzes the light transmission and backscattering of the samples using a detection head, which contains a pulsed near-infrared light source (λ = 880 nm). It moves up and down along a cylindrical cell to acquire data from transmission (180^o from the incident light) and backscattering (45^o from the incident light). To make all the measurements, 20 ml of sample in water at concentrations of 1 mgFe/ml were used to fill the cell. The samples used in this thesis were scanned each minute for the first day and every five minutes for the next 4 days.

3.6 Magnetic characterization

3.6.1 DC magnetometry

These techniques allows to calculate the magnetic moment of the sample as a function of field and temperature. The vibrating sample magnetometer generates an electromagnetic field which is applied to the sample, that is vibrating at a known frequency and amplitude. This field generates a magnetic flux change that in turn produces an electromotive force that is collected in the detection coils present in the equipment. The electromotive force generated by applying the magnetic field is proportional to the magnetic moment of the sample, allowing the calculation of its value.

The superconducting quantum interference device create an electric current that flows indefinitely without the need to apply a potential difference. This equipment, known as Josephson junction, is achieved by coupling two superconductors linked through a weak link that acts as a thin insulating barrier. The advantage of using this type of systems allows the measurement of very subtle magnetic fields, being able to measure magnetic signals of the order of 10^{-9} to 10^{-10} Am^2, while the limit of detection for magnetometers of vibrating sample is of 10^{-6} to 10^{-8} Am^2.

Here, magnetic characterization was performed on dried powder using a vibrating sample magnetometer (VSM; MLVSM9 MagLab 9 T, Oxford Instrument) and a SQUID magnetometer (MPMS-XL, Quantum Design). Magnetization curves with a maximum applied field of 5 T were measured at 5 and 290 K. The saturation magnetization (M_s) and coercive field (H_c) was achieved by fitting the magnetization curves at room temperature to the Langevin function (default Langevin function in Origin2016). The initial susceptibility (χ) was measured in the field range $\pm$100 Oe. Thermal dependence of the magnetization under zero field cooled (ZFC) and field cooled (FC) conditions, from 5 to 350 K, has been measured by applying 100 Oe magnetic field. The blocking temperature (T_B) was determined from the maximum of the ZFC measurement, by fitting the curve with a parabolic function.

For the cell samples, the cell pellets were re-suspended in 100 μl of PBS, frozen (-20 ^oC) and lyophilized. Finally, the powder was transferred to gelatine capsules. If the sample is not lyophilized there will be a diamagnetic contribution on the MH curve due to water, showing a negative linear magnetization response at high fields.

3.6.2 AC susceptibility

In this technique a low field amplitude AC magnetic field is applied over the sample. The magnetic moment of the sample is measured as a function of either the frequency of the applied field at constant temperature or as a function of temperature at a specific frequency, being the first one used in this thesis. The frequency of the applied

field is varied and the dynamic response from the sample is measured. Physical modeling enables indirect determination of some nanoparticles properties as the size and size distribution, magnetic anisotropy and magnetic relaxation properties.

Frequency dependence of the AC magnetic susceptibility (ACS) was measured using two AC susceptometers: the DynoMag system was utilized between 1 Hz and 500 kHz and a high frequency AC susceptometer was used in the frequency range between 500 kHz and 10 MHz. Measurements were carried out at room temperatures with samples in liquid (200 μl), using excitation fields in the range of 30 μT to 500 μT. AC susceptibility spectra were recorded as a function of the frequency and the curves were fitted to obtain the hydrodynamic and core size using different models. Data were normalized for comparison. For the cell samples, AC Susceptibility measurements were performed with lysosomes in liquid, at room temperature. The cell pellets were lysed in 200 μl of ice-cold lysis buffer containing 50 mM HEPES, 150 mM NaCl, 1 % Tritón-X 100, 1 mM PMSF, 10 $\mu g/mL$ leupeptin, 10 $\mu g/mL$ aprotinin, 0.5 mM EDTA, 5 mM NaF, 1 mM sodium orthovanadateand, 0.2 µM okadaic acid, keeping pH 7.4 for 30 min on an orbital shaker at 4 ^oC.

To fit the curves it was used two models named Multi-core and Single-core which will be described below.

i) Multi-core model:

$$\chi(\omega) = \chi_{0B} \int \frac{1}{1 + j\omega\tau_B(r_H)} f(r_H) dr_H + \chi_{high} \tag{3.1}$$

where χ_{0B} is the DC susceptibility for the particles that undergoes Brownian relaxation, χ_{high} is the dynamic susceptibility at frequencies much higher than the Brownian relaxation frequency (due to single-domain crystals with fast Néel relaxation with respect to the Brownian relaxation), ω the angular frequency ($2\pi f$), r_H the hydrodynamic radius of the particles, $f(r_H)$ is the hydrodynamic radius distribution function, and τ_B is the Brownian relaxation time, σ is the distribution width and r_{mH} is the median particle radius.

Hydrodynamic radius distribution function:

$$f(r_H) \propto \frac{1}{r_H} e^{-\frac{1}{2ln^2\sigma} ln^2(\frac{r_H}{r_{mH}})} \tag{3.2}$$

ii) Single-core model:

$$\chi(\omega) = C \int \frac{r_C^6}{1 + j\omega\tau_{eff}(r_H)} f(r_H) dr_H + \chi_{high} \tag{3.3}$$

where

$$C = \mu_0 M_S (\frac{4\pi}{3})^2 \frac{1}{3kT} \tag{3.4}$$

τ_{eff} is the effective relaxation time (s) and it can be modeled using the Brownian relaxation time, τ_B, and the Néel relaxation time, τ_N, r_C is the particle core radius, r_H is the particle hydrodynamic radius .

3.7 Assessment of different bioapplications

3.7.1 Magnetic Resonance Imaging

This technique has been used to measure the proton relaxation times of suspensions in the presence of nanoparticles, being essential to determine the efficacy of the particles for its use as contrast agents in magnetic resonance imaging (MRI). Thus, MRI relaxometric properties were investigated by measuring the longitudinal (T_1) (sequence t1-ir-mb) and transversal (T_2) (sequence t2-ir-mb) protons relaxation times at different dilutions between 0 and 0.07 mM of Fe in a MINISPEC MQ60 (Bruker) at 37 ^oC and a magnetic field of 1.5 T. The sequences used are original from Bruker.

MRI images were taken in a Agilent/Varian with a magnetic field of

7 T. The animals were anesthetized with 2 % isoflurane and one line of 100 % oxygen and positioned on a stretcher regulated to a temperature of 38.7 ^oC. Liver images were acquired using a gradient echo sequence with TE (echo time) / TR (repetition time) 5 ms / 50 ms, bandwidth of 50 kHz, Field-of-view (FOV) of 3 cm x 3 cm, 1 mm of thickness of cut, 30 sweeps and angles of rotation of 30 and 20^o. Nanoparticles and magnetoliposomes were injected (100 μl at 1 mgFe/ml) and the signal in the liver monitored with time. Phantoms images were obtained at different iron concentrations from 0 to 1 mM in water and placed inside the MRI equipment at the same time.

3.7.2 Magnetic hyperthermia

The magnetic nanoparticles produce heat under the effect of an alternating magnetic (AC) field. The energy from the external AC source is transformed in heat by mechanical (Brownian) or magnetic (Néel) fluctuations of the nanoparticles, depending on the frequency range considered. The parameter used to compare the performance of different magnetic colloids is the specific power absorption rate (SAR) (the power absorbed by unit mass of the magnetic material involved at a given magnetic field amplitude and frequency). SAR was measured on a Fives Celes generator specially designed for heating magnetic nanoparticles model Nº 12118 M01 (France), equipped with water cooled electrolytic copper made 50 mm diameter coils with 6 numbers of turns. The sample was kept in a vial and placed at the centre of the heating coil. Experiments were performed under frequencies of 92, 202 or 282 kHz at different external field amplitudes, 52, 24 or 17 kAm^{-1} respectively. Sample temperature was measured using a fiber optic temperature sensor (OSENSA's FTX).

SAR was determined from the ΔT vs time curves (where ΔT indicates temperature increase over the base line temperature),

$$SAR = C_P \frac{m_S}{m_F} \frac{\Delta T}{\Delta t} \tag{3.5}$$

where C_P is the solution specific heat(4.18 $J/g\ ^oC$ for water), m_S the total ensemble mass, m_F the magnetite mass and $\Delta T/\Delta t$ the initial slope of the field induced heating curve. As the measurements are performed in nonadiabatic conditions, the curve slope is fitted only in the first few seconds after turning the magnetic field on, typically during the first 30 s. Measurements must be done with at least 500 μl, and sample should be sonicated for 5 minutes before to prevent precipitation. In this work the initial temperature was settled at 37.2 ^oC with a refrigerator.

3.7.3 Drug release kinetics

Drug release experiments were carried out with doxorrubicin taking advantage of its optical properties. A Biochorom WPA Biowave DNA UV-Visible spectrophotometer was used over the wavelength range from 450 to 700 nm. The samples were dispersed in water and placed on a 1 mm wide quartz cuvette. The spectral range of the apparatus is 190-900 nm (5 nm bandwidth). The precision of the equipment is $\pm$2 nm. A standard curve was performed with concentrations from 1 to 100 μM of DOX. For the experiments *in vitro* it was used an initial concentration of 50 μM. The DOX release from liposomes was evaluated as a function of time up to 48 h, as a function of temperature up to 45 ^oC for one hour, as a function of applied magnetic field with 30 mT for one hour and finally as a function of dialysis up to 48 h.

3.7.4 In-vitro cell culture studies: uptake and cytotoxicity assays

Cytotoxicity assays in this thesis have been conducted in four different cell lines: Pan02, Jurkat, HeLa and MDA-MB-231.

The murine Pan02 pancreatic ductal adenocarcinoma cell line and the human T-lymphocyte Jurkat cell line were cultured in DMEM supplemented with 10 % fetal calf serum (FCS), 100 U/ml penicillin, 100 mg/ml streptomycin, 2 mM L-glutamine and 1 mM sodium pyruvate in

standard culture conditions (37 ^oC, 5 % CO_2, 90 % relative humidity). Pan02 cells were seeded in 35 mm plates (10^5 cells/plate) and allowed to adhere for 24 h. Meanwhile, at the corresponding time, the cells were treated with dispersions of nanoparticles (DMSA or APS coated) in culture media (150 $\mu gFe/ml$, 2 ml) for different time intervals (0.5, 3 or 24 h), once reached 48 h, culture medium was removed and samples were washed three times with 2 ml of phosphate-buffered saline (PBS, pH 7.4). Jurkat cells (3×10^6 cells) were incubated with the nanoparticles coated with APS (0.15 mgFe/ml, 300 μl) for 2 h. After incubation, cells were washed twice with 1 ml of PBS (400 rcf, 4 min) and prepared according to the corresponding technique.

HeLa cells (human cervical cancer cell line) were cultured in DMEM culture medium, supplemented with 10 % fetal bovine serum (FBS), 50 U/ml penicillin and 50 mg/mL streptomycin. Cell cultures were performed in a 5 % CO_2 atmosphere and subsequently incubated for 24 h at 37 ^oC with different concentrations of nanoparticles (0.05 mgFe/ml, 0.1 mgFe/ml, 0.2 mgFe/ml) and DOX (1 to 5 μM) in a SteriCult 200 (Hucoa-Erloss, Madrid, Spain) incubator. 25×10^3 HeLa cells were seeded per well in 24-well culture plates and 40×10^3 cells were seeded in individual culture plates (35 mm diameter) for the hyperthermia tests.

MDA-MB-231 cells (human breast cancer cell line) were cultured in DMEM culture medium supplemented with 10 % FBS, 100 mg/ml streptomycin, 100 U/ml penicillin, and 1 mM L-glutamine in standard culture conditions (37 ^oC, 5 % CO_2, 90 % relative humidity). MDA-MB-231 cells were seeded at the appropriate density that guaranteed subconfluence, specifically at a density of 25×10^3 cells per well at a 24-well plate. Also it was seeded 125×10^3 cells per individual plate 835 mm), used for the tests with applied magnetic field. The working volumes of 1 ml and 3 ml were used for 24-well and individual plates, respectively. Three days after cell seeding, cell cultures were exposed to different treatments, with free DOX, liposomes, NP, liposomes with DOX encapsulated, liposomes with NP encapsulated and liposomes with both NP and DOX encapsulated, maintaining the concentrations of 0.1 mgFe/ml and 0.4 μM DOX. After exposure to the treatments for 24 h, the excess was eliminated and culture media were replaced.

Individual plates were submitted to the application of an alternate magnetic field, 30 mT, 202 kHz for 1 hour. Cells were analyzed after 24 hours. Culture media was replaced every other day.

Cellular uptake of the nanoparticles, expressed as the amount of iron per cell, was quantified by elemental analysis of Fe using ICP-OES analysis. Cell digestion was carried out at 90 ^oC, using firstly 900 μL of 65 % (v/v) HNO_3 (1 h) and secondly 1 ml of 30 % (p/v) H_2O_2. After dilution with 8 ml of distilled water, iron concentration was measured by ICP-OES. Untreated cells were also analyzed to subtract the amount of endogenous iron. Data obtained by the elemental analysis was divided by the number of cells per sample, previously counted with a Neubauer chamber.

To localize and visualize the nanoparticles distribution inside HeLa cells, a specific reaction called Prussian blue staining was performed, that detects iron. Cells were seeded and incubated with magnetic nanoparticles and their subsequent post-incubation in complete medium, were fixed in methanol at 20 ^oC for 5 min and allowed to dry. Then, they were stained for 15 min with a solution of 2 % potassium ferrocyanide and 2 % HCl in distilled water. After two washes in distilled water, the cells were counterstained with 0.1 % neutral red in distilled water for 2 min.

To test cell viability, MDA-MB-231 cell cultures were analyzed by using a Live-Dead kit according to the manufacturer's instructions (Life Sciences). This kit is based on the use of calcein and ethidium homodimer-1 (EthD-1). Calcein is a non-fluorescent cell permeable dye that gets converted into a strong green light emitting compound after contact with intracellular esterases and so retained inside live cells. In contrast, EthD-1 is a DNAintercalating agent that penetrates cell membranes in dead cells and emits red fluorescence when inserted into the DNA double helix. After staining, samples were visualized by using a Leica SP5 confocal laser scanning microscope (CLSM). The fluorescence of both probes was excited by an argon laser tuned to 488 nm. After excitation, emitted fluorescence was separated by using a triple dichroic filter 488-561-633 and measured in the range 505-570 nm for green fluorescence (calcein) and 630-750 nm for red fluores-

cence (EthD-1). To quantify cell viability, the number of live (green) and dead (red) cells was counted and averaged from the confocal images acquired.

To determine cytotoxicity of the nanoparticles, 5×10^3 Pan02 cells and 10^5 Jurkat cells were seeded per well in 96-well culture plates and cultured for 24 h. Next, cells were treated with the corresponding nanoparticles in a concentration range of 0.01–0.5 mg Fe/ml and incubated for 24 h. For the last 4 h, PrestoBlue (PrestoBlue Cell Viability Reagent, A13261; Invitrogen) was added following manufacturer's instructions. Finally, cell suspensions were centrifuged (1467 rcf, 15 min), 100 μL of the supernatant were transferred to a new plate and fluorescence was measured ($\lambda_e x$ 460 nm; $\lambda_e m$ 490 nm). Untreated cells were used as controls and complete DMEM incubated with PrestoBlue was used as background control. Cell viability was calculated according to the following formula:

$$cytotoxicity(\%) = \frac{treatedcellfluorescence - background}{untreatedcellfluorescence - background} \times 100 \tag{3.6}$$

Mitochondrial activity of HeLa cells was also assessed by MTT colorimetric assay. Cells exposed to treatments were incubated with a 50 mg/mL solution of dimethylthiazolyl-diphenyl-tetrazolium bromide (MTT;Sigma-Aldrich) in culture medium (from an initial MTT stock 1 mg/mL in PBS). Cells were incubated for 3 h, then reduced formazan was extracted with 500 ml DMSO and absorbance was measured at 542 nm in a SpectraFluor spectrophotometer (Tecan Group Ltd,Mannedorf, Switzerland). Mitochondrial activity, as an indirect indicator of cell survival, was expressed as the percentage of absorption of treated cells in comparison with that of control cells.

Chapter 4

Results

This chapter is focused on describing and discussing the main results obtained in this thesis, starting with the synthesis of magnetite nanoparticles by microwave heating and comparing then with those obtained by thermal decomposition in organic media. Varying the amount and proportion of the reagents used, as well as the conditions of the synthesis, we have established the limits on how these parameters influence the size of the nanoparticles prepared by microwave heating. Afterwards those nanoparticles are encapsulated in liposomes by different preparation methods.

Different spatial distribution of the nanoparticles are controlled by the coating, being possible to attach them on the liposome surface, inside the lipid bilayer or inside the aqueous compartment. Aggregation degree and the spatial distribution of nanoparticles in cells and magnetoliposomes are compared and the magnetic properties were evaluated by DC measurements on lyophilized samples and the Dynamic magnetic behavior (AC) was analyzed in liquid samples.

By the end of the chapter are the biomedical application evaluation, starting with the viability tests carried on HeLa cell line, followed by the study of the nanoparticles and magnetoliposomes as contrast agents for MRI, for magnetic hyperthermia treatment and as carriers for drug delivery.

4.1 Microwave assisted synthesis of magnetic nanoparticles

Iron oxide magnetic nanoparticles have been synthesized using a microwave assisted synthesis method in organic media, looking for a more efficient and reproducible method. Previous works show that in water very small nanoparticles were achieved [142], while larger nanoparticles were obtained at higher temperatures using organic solvents of high boiling point. The effect of different experimental conditions such as the solvent, precursor, and surfactant concentration and reaction time are analyzed and optimized to obtain magnetic iron oxide nanoparticles with different core sizes. Structural, colloidal and magnetic properties have been analyzed after its transference to water and compared with those nanoparticles prepared by thermal decomposition in organic media. The novelty relies on the use of a solid oleate-iron precursor, which assures the scalability and reproducibility of the synthesis, and the fact that microwave heating resulted in being more efficient than traditional heating methods, and therefore it has a great potential for nanoparticle industrial production.

4.1.1 Synthesis assisted by microwave heating

To fully understand the synthesis with microwave heating several tests were performed. First it was tested different polar solvents such as Dibenzyl-Ether, Phenyl-Ether, Octadecene, Ethylene Glycol and Benzyl Alcohol, which have different dielectric constants. After testing different iron precursors the finally chosen one was an oleate derivative of iron prepared in solid form, which is easily handled [143]. After that some changes were made on parameters like the heating ramps followed by the iron concentration and molar ratio (oleic acid/iron).

Microwave assisted synthesis of magnetic nanoparticles in organic media was carried out starting from a solid oleate-iron precursor. Having a solid precursor has many advantages in comparison to a liquid oleate: its scalability, reproducibility, high stability over time, easy pu-

rification by precipitation, and finally its ease to weight in comparison to the standard liquid oleate, which is a highly viscous plastic fluid [131] [133] [132].

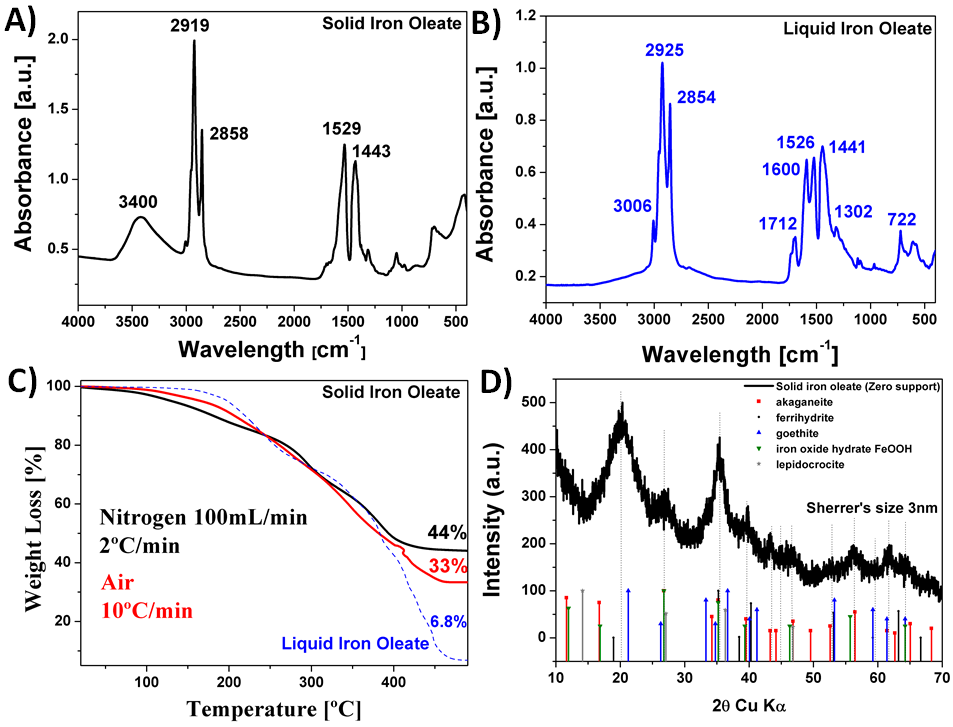

Figure 4.1: Infrared spectroscopy absorbance of solid (A) and liquid oleate (B) [131] [144]. C) Thermogravimetric analysis of the Fe oleates (solid and liquid) under different conditions. D) X-ray diffraction pattern for solid iron oleate. Adapted from [145].

Solid oleate-iron also presents distinctive characteristics in comparison to the authenthic liquid oleate such as a higher Fe content as determined by TG (33 $\%wt$ Fe in the solid iron oleate against 6.8 $\%wt$ in the liquid iron oleate, figure 4.1C) and different iron-oleic acid coordination. As a result of that, using the solid oleate-iron in a reaction requires the addition of a larger amount of oleic acid to preserve the oleic acid/Fe ratio of 3-4 that has been described as ideal for the synthesis of uniform magnetic nanoparticles by thermal decomposition [132] [146]. One of the problems of using liquid oleate in a reaction is that its composition change with time, making it difficult to control the amount of oleic acid needed in the reaction media, which is critical

to control the particle growth and consequently the particle size [146] [79].

Solid and liquid oleates have different Fe coordination to the carboxylic groups of the oleic acid as shown by IR spectroscopy (figures 4.1 A and B), being bidentate in the case of the solid oleate instead of monodentate. Such difference is seen by the distance between the carboxyl bands at 1600 and 1455 cm^{-1} [147], which is 86 cm^{-1} for the solid oleate and 145 cm^{-1} for the liquid oleate. Solid oleate-iron is in fact an iron hydroxide as demonstrated by X-ray diffraction (figure 4.1D). This oleic coated hydroxide is expected to be less reactive than liquid iron oleate, which also presents X-ray diffraction pattern but with low crystallinity (data not shown). Consequently, the heating ramp becomes a key parameter to control the solid oleate-iron precursor decomposition and therefore the particle nucleation. Solid oleate-iron also consists of tiny anisometric nanoparticles (around 10 by 2 nm as shown by TEM figure 4.2) that resemble those for Fe hydroxides such as goethite or lepidocrocite [59]. In contrast to that, liquid oleate having monodentate coordination and amorphous structure decomposes easily and is less sensible to the temperature ramp resulting in similar particle sizes for temperature ramps between 3 and 6 $^oC/min$ [148].

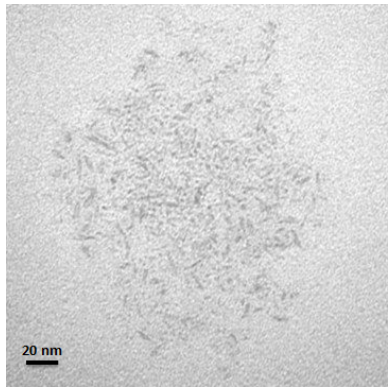

Figure 4.2: TEM image of solid oleate-iron, where it can be seen a hydrophobized hydroxide nanomaterial. Reprinted from [145].

Now when considering solvents for the microwave reaction in a pressurized vessel, the efficiency of the reactant mixture to couple with an applied microwave field becames more important than boiling points,

as mentioned before in chapter 2. Knowing that the dielectric constant goes from 1 (vacuum) to 88 (water), in this work it was elected solvents with different dielectric constants, from above 2 (Octadecene) to 47 (DMSO), to identify its effect on the nanoparticles formation. The first thing observed was that too polar solvents with relatively high vapor pressure (like DMSO), quickly rise the pressure in the system and the equipment shuts down, as a safety precaution. The second thing observed was that solvents with low dielectric constant (like Octadecene) generate paramagnetic nanoparticles, which are not the aim of this work (figure 4.3). Dibenzyl-Ether (dielectric constant of 3.86) was elected as the most suitable one, given the magnetic properties of nanoparticles synthesized with it, also its price is 10 times lower than Benzyl Alcohol [145], solvent utilized by many research groups using microwave heating [149] [142] [150] [95] [151]. After that parameter it was analyzed the effect of different heating ramps and total time of synthesis.

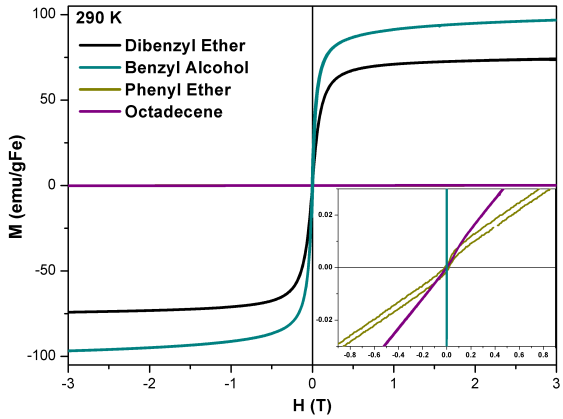

Figure 4.3: Hysteresis loops at room temperature for nanoparticles obtained by microwave assisted synthesis using different solvents. Solvents with low dielectric constant such as Octadecene and Phenyl Ether generate paramagnetic nanoparticles while solvents with higher dielectric constant generate nanoparticles with high saturation magnetization values. Reprinted from [145].

In this work three heating ramps were tested, 3.75 $^oC/min$ (fig-

ure 4.4B), $> 4\ ^oC/min$ (figure 4.4E) and $< 2\ ^oC/min$ (figure 4.4F). The optimal ramp is 3.75 $^oC/min$ for giving rise to the most uniform nanoparticles (figure 4.4A and B). Faster heating ramps result in smaller nanoparticles, while slower heating ramps result in nanoparticles heterogeneous in shape and with wide size distribution. It is possible to get larger uniform particles by extending the reaction time from 1 up to 4 hours, with a limit in size of around 8 nm, which is given by the exhaustion of iron precursor (figure 4.4C and D) [79].

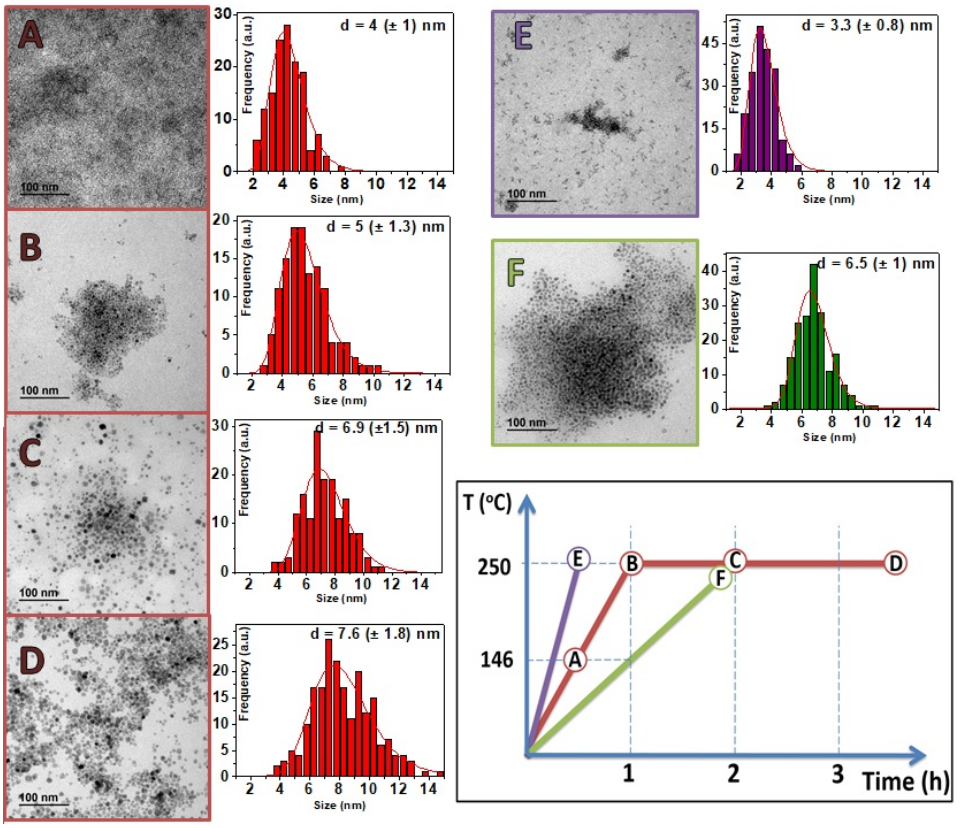

Figure 4.4: Temperature profile of the microwave synthesis. TEM images of the nanoparticles obtained with different heating ramps and total synthesis time. a) 146 ^oC in 30 minutes, b) 250 ^oC in 1 hour, c) 250 ^oC in 1 hour and maintained for 1 hour, d) 250 ^oC in 1 hour and maintained for 2 hours and 30 minutes, e) 250 ^oC in 30 minutes and f) 250 ^oC in 2 hours. Adapted from [145].

Other critical parameter in iron-oxide nanoparticle synthesis is the iron concentration of the reaction mixture and the molar ratio between

oleic acid and iron. To that matter it was carried out different tests with different iron concentration and molar ratio (Oleic/Fe). Figure 4.5 shows different samples, with the same heating ramp 250 ^oC in 1 hour and maintained for 1 hour,(figure 4.4, ramp B).

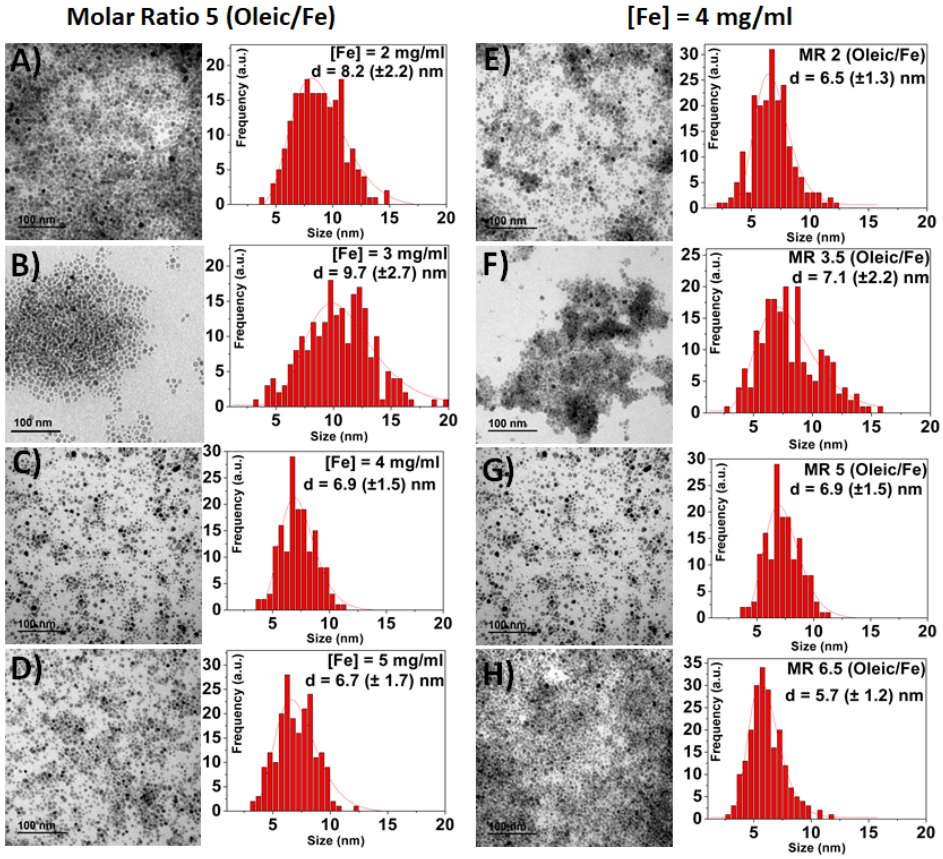

Figure 4.5: TEM images and size distribution of the nanoparticles obtained when changing the iron concentration from 2 to 5 mgFe/ml (35.8 mM to 89.5 mM), shown on images A to D. On the other hand, changing the molar ratio Oleic acid/Fe (MR) from 2 to 6.5, images E to H. Red lines represent a Log-normal fit. Adapted from [145].

From figure 4.5 A to D same molar ratio of 5 (Oleic/Fe) with different iron concentrations were tested, the particle sizes were measured by the TEM images and the size distribution were fitted by Log-normal distribution function. It can be seen that the higher is the iron precursor concentration (from 2 to 5 mgFe/ml), the smaller are the nanoparticles. Similar results were found for thermal decomposition where

the saturation concentration of the growth species increases and more nuclei are formed, resulting in less growth and hence smaller nanoparticles are formed [152] [75]. To study the effect of molar ratio it was chosen an iron concentration of 4 mgFe/ml. As can be seen in figures 4.5 E to H, there is no significant change on the particle size not even when increasing 3 times the amount of oleic acid in the reaction mixture, in contrast with the strong oleic acid effect when using other iron precursors such as iron acetylacetonate [78].

As said, the most common solvent in recent works is Benzyl Alcohol. Alternatively, room temperature ionic liquids such as 1-butyl-3-methylimidazolium tetrafluoroborate ([BMIM][BF4]) are good candidates for making a nonpolar, or with low dielectric constant, solvent suitable for microwave heating [96]. Their ionic character presents excellent coupling capability with microwave irradiation. Unfortunately this is only true when the pressure of the microwave equipment can be controlled, otherwise the difference between both synthesis, in this case magnetite nanoparticles synthesized with Dibenzyl ether, is not worth the high prices of ionic liquids, as seen in figure 4.6, since there is no evident increase of the core size nor a reduction in size distribution.

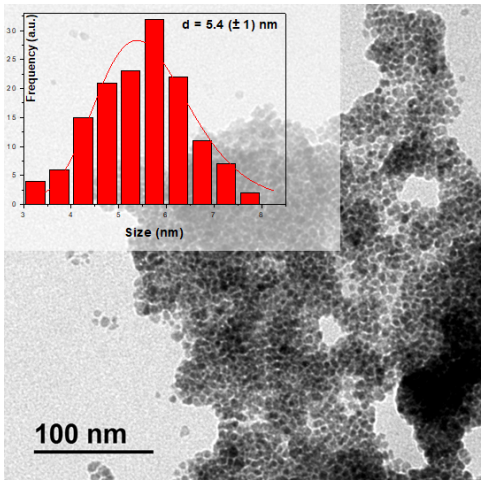

Figure 4.6: TEM image of magnetite nanoparticles obtained by microwave (MW) using Dibenzyl Ether as solvent with the addition of 1/10 wt of ionic liquid 1-butyl-3-methylimidazolium tetrafluoroborate [BMIM][BF4]. Inset shows size distribution fitted by Log-normal with mean size of 5.4 nm ($\sigma = 0.17$).

4.1.2 Comparison with other heating sources

Other important point to be considered is if the heating method plays an important role on the final size and size distribution of the nanoparticles, as said in [84]. To do so, the same reaction mixture was performed with microwave assisted synthesis and thermal decomposition synthesis. The parameters chosen as standard are: heating ramp of 3.75 $^oC/min$ until 250 ^oC and 1 hour at this temperature, iron concentration of 4 mgFe/ml, molar ratio of 5 (Oleic/Fe), and solid iron oleate as the precursor.

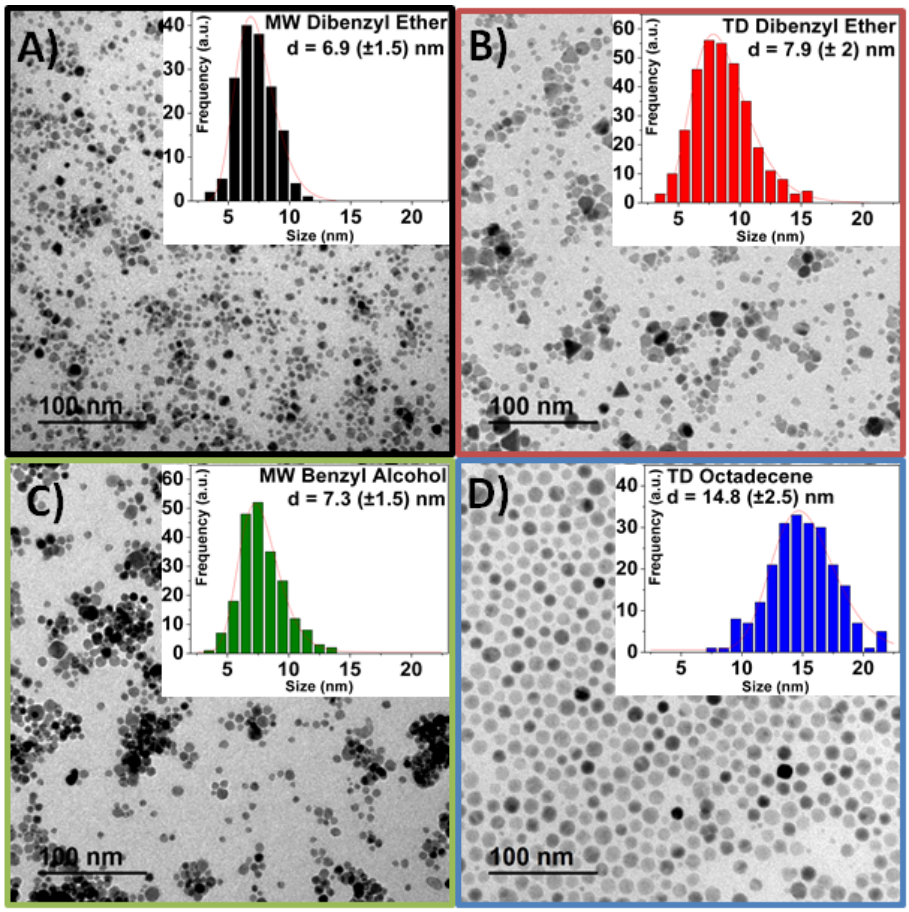

Figure 4.7: TEM images of magnetite nanoparticles obtained by microwave (MW) and thermal decomposition (TD), using different solvents (dibenzyl ether (A and B), benzyl alcohol (C) and octadecene (D)).Nanoparticles coated with DMSA. Adapted from [145].

Starting from the microwave, samples were synthesized using dibenzyl ether (figure 4.7A) and benzyl alcohol (figure 4.7C) as solvents (named as MwE8 and MwA8 respectively), while the ones prepared by thermal decomposition were achieved by using dibenzyl ether (figure 4.7B) and octadecene (figure 4.7D) as solvents (named TdE12 and TdO15 respectively). Their respective TEM images are shown in figure 4.7, with the same magnification for ease comparison. Insets show their size distribution fitted by Log-normal functions. Sample MwE8 (Black) has a mean size of 6.9 nm ($\sigma = 0.21$), while MwA8 (Green) has a mean size of 7.3 nm ($\sigma = 0.21$). Otherwise, sample TdE12 (Red) has a mean size of 7.9 nm ($\sigma = 0.26$) and TdO15 (Blue) has a mean size of 14.8 nm ($\sigma = 0.17$).

Firstly, the largest size of magnetite nanoparticles is always obtained when prepared with the highest boiling point solvent (dibenzyl ether = 160 ^oC, benzyl alcohol = 205 ^oC, and octadecene = 315 ^oC) [131] [79] [153]. Secondly, nanoparticles synthesized by heat transfer tend to be bigger than the ones produced by microwave heating. This difference in sizes between both synthesis methods can be explained by their different nucleation and growth processes, as seen in figure 4.8. Using the same initial parameters and changing the method of heating it can be seen that there is difference between the sizes of nanoparticles in figure 4.8. For the microwave heating the mean size is in 6.9 nm ($\sigma = 0.21$), while for thermal decomposition the mean size is in 7.9 nm ($\sigma = 0.26$). By conventional heating nanoparticles tend to nucleate on the vessel walls first, given its inhomogeneous heating profile [154]. On the other hand, for samples irradiated with microwave frequencies, dipoles tend to align in the direction of the applied electric field; in such a way energy is lost in the form of heat, through dielectric loss and molecular friction [155], producing efficient internal heating, by creating numerous "hot spots" which could trigger multiple nucleation events throughout the solution, increasing the product yield [84] [104] but decreasing the average size due to the enhanced competitive growth.

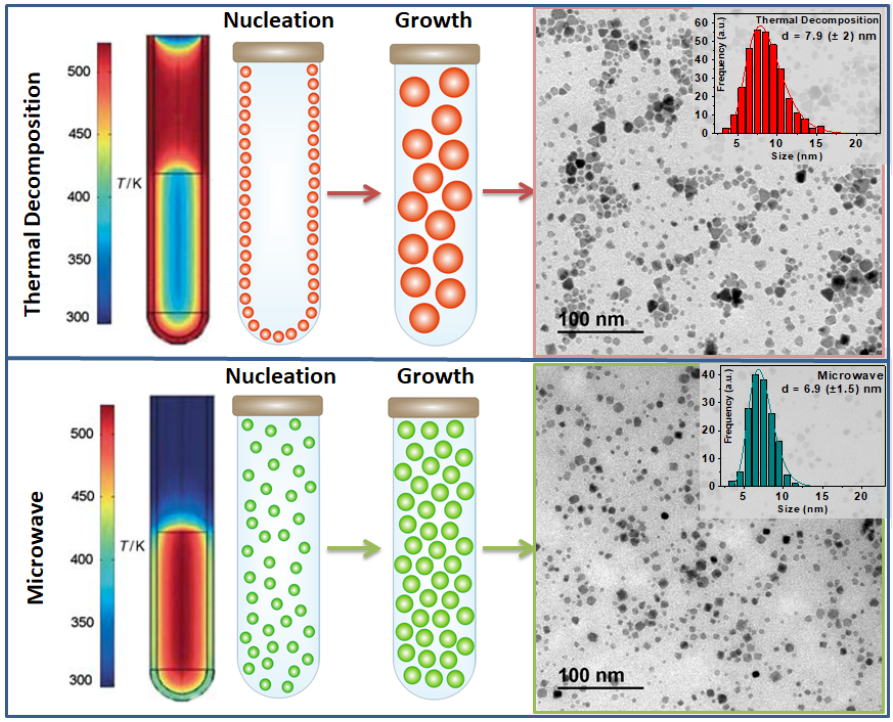

Figure 4.8: Comparison between Thermal Decomposition and Microwave heating and the effect on nanoparticles sizes. On the upper part, nanocrystals tend to nucleate on the vessel walls first for thermal decomposition (mean size of 7.9 nm), on the other hand for microwave, at the bottom part, nanocrystals tend to form more rapidly, creating more seeds that grow less in size (mean size of 6.9 nm).

Given the hydrophobicity of the synthesized particles (which are coated with oleic acid), they are not suitable to use in biomedicine, for that matter this nanoparticles were transferred to an aqueous medium by exchanging the oleic acid of the surface by dimercaptosuccinic acid (DMSA) (for more details go to chapter 3, section 3.2).

4.1.3 Structural and colloidal characterization

Structural and colloidal properties of the nanoparticles after being transferred to water were evaluated. Figure 4.9A shows the X-ray patterns for nanoparticles obtained by microwave (MW) and thermal decomposition (TD) as described above. All peaks correspond to crys-

tallographic magnetite or maghemite planes discarding the presence of secondary phases. Crystal sizes were calculated from the broadening of 311 peak, which vary from 7.9 nm (Black) to 8.5 nm (Green) for MW samples and from 12.2 nm (Red) to 15.5 nm (Blue) for TD samples.

Nanoparticles infrared spectra shows the typical bands for water above 3100 cm^{-1}, for C-H vibration at 3000 cm^{-1}, for the coating signature between 1000 and 1700 cm^{-1} and bands below 1000 cm^{-1} are associated with the vibration modes of the iron oxide, Fe-O stretching [156] (figure 4.9D).

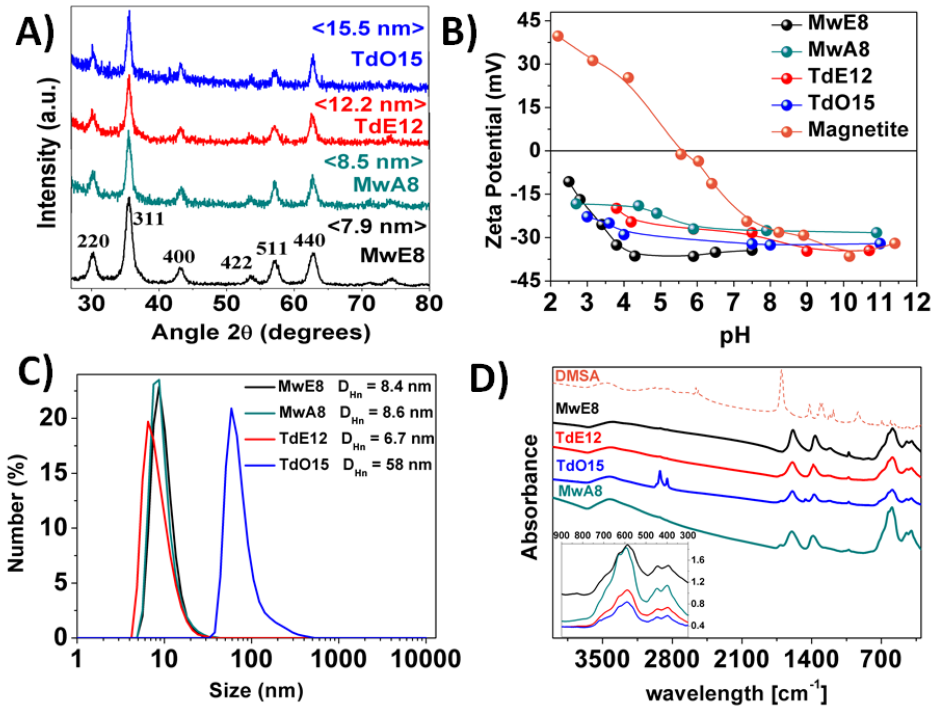

Figure 4.9: A) X-ray diffraction patterns with calculated crystal mean size for magnetite nanoparticles obtained by microwave (MW) and thermal decomposition (TD) using different solvents; B) Surface charge measurements as a function of pH for DMSA coated nanoparticles and uncoated magnetite for comparison; C) Hydrodynamic size in number distribution; D) Infrared spectra for DMSA coated nanoparticles and DMSA for comparison. Inset shows the spectra at low frequency range. Adapted from [145].

The coating of the nanoparticles (DMSA) is responsible for the high negative zeta potential (between -10 and -34 mV) in a wide pH

range (between pH 2 and 11) (figure 4.9B), allowing a great stability in different media, without loosing the negative characteristic surface charge, uncoated magnetite (produced by coprecipitation) is used for comparison, presenting an isoelectric point at around pH 6 (orange curve figure 4.9B).

Hydrodynamic sizes of the nanoparticles aqueous suspensions were measured by Dynamic Light Scattering (DLS) in intensity. Sizes are between 30 and 170 nm (figure 4.10), increasing as the amount of coating on the nanoparticle surface increases, as it can be observed if we compare the hydrodynamic sizes with the weight losses obtained from the thermogravimetric analysis (figure 4.10). For instance, the larger hydrodynamic size (corresponding to sample TdO15), has the larger amount of DMSA on the nanoparticle surface, nevertheless the presence of aggregates cannot be completely discarded.

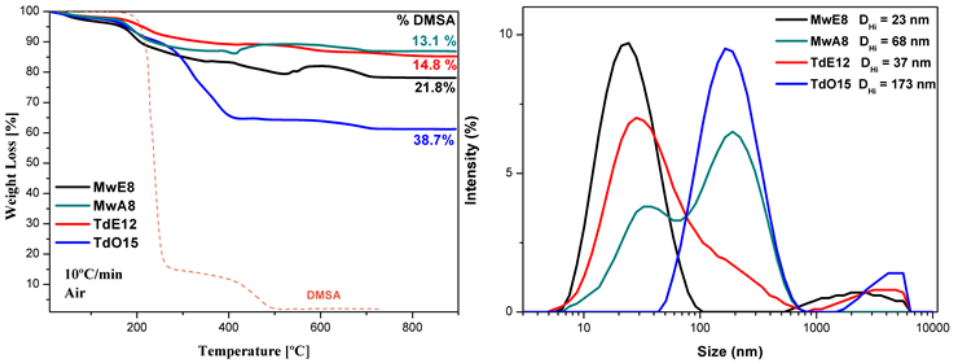

Figure 4.10: Thermogravimetric analysis showing the amount of DMSA coating on nanoparticles obtained by microwave (MW) and thermal decomposition (TD), using different solvents. DMSA weight loss is included for comparison (left image). Hydrodynamic size in intensity distribution are between 30 and 170 nm (right image). Adapted from [145].

Hydrodynamic sizes in number (derived from the intensity distribution using Mie theory) are adjusted to a monomodal distribution with mean values around 6-9 nm for the smallest particles and 58 nm for the largest ones (figure 4.9 C). This result indicates that most of the particles are well dispersed forming a stable colloid and only a small fraction are aggregated leading to a broadening of the peak in the DLS intensity distribution or a bimodal distribution, as it is the case of

sample MwA8 (figure 4.10). No remarkable differences were found for particles prepared by TD and MW in relation to the colloidal properties. Hydrodynamic sizes are important depending on the application since it may limit its use. For example, particles larger than 200 nm are rapidly captured by the Reticuloendothelial System (RES) [157].

Colloidal stability with time was evaluated using nanoparticles suspensions at 1 mgFe/ml, at pH 7 and the results can be seen in table 4.1. The most stable presents only 0.2 % precipitate after 24 h, while the less stable suspension presents 1.8 % precipitate in the same time interval. After 4 days the nanoparticles suspension stability was maintained, with less than 2 % precipitate in all cases. This is an important parameter when working with biological applications since a stable colloidal suspension is required to work with *in-vivo* experiments, which will be discussed more in chapter 4.4.

4.1.4 Magnetic characterization

DC magnetic properties were evaluated for DMSA coated nanoparticles. Figure 4.11 shows the hysteresis loops at room temperature and 5 K. Saturation magnetization values and nanoparticle magnetic size were obtained by fitting the magnetization curves at room temperature to the Langevin function. The particles are close to the superparamagnetic regime, showing rather low coercive fields at room temperature. At 5 K the system is magnetically blocked, showing higher coercivity for larger particles.

The hysteresis loops show that the larger the particle, greater their saturation magnetization due to the decrease in surface area/volume ratio, and therefore lower surface effects such as spin canting [132] [158]. The higher saturation magnetization values (TdO15, blue) are close to those reported for bulk magnetite (115–128 $Am^2/kgFe$ at RT and 5 K respectively) [140]. The smallest values (55-60 $Am^2/kgFe$) correspond to MwE8 sample (black) with the smallest crystal size (figure 4.9A).

Figure 4.11 also shows the ZFC-FC curve for all samples described above; being measured from 20 K to room temperature at 100 Oe. The

blocking at low temperature is evident for smaller nanoparticles (MW), while larger particles are still blocked at room temperature (TD) [132].

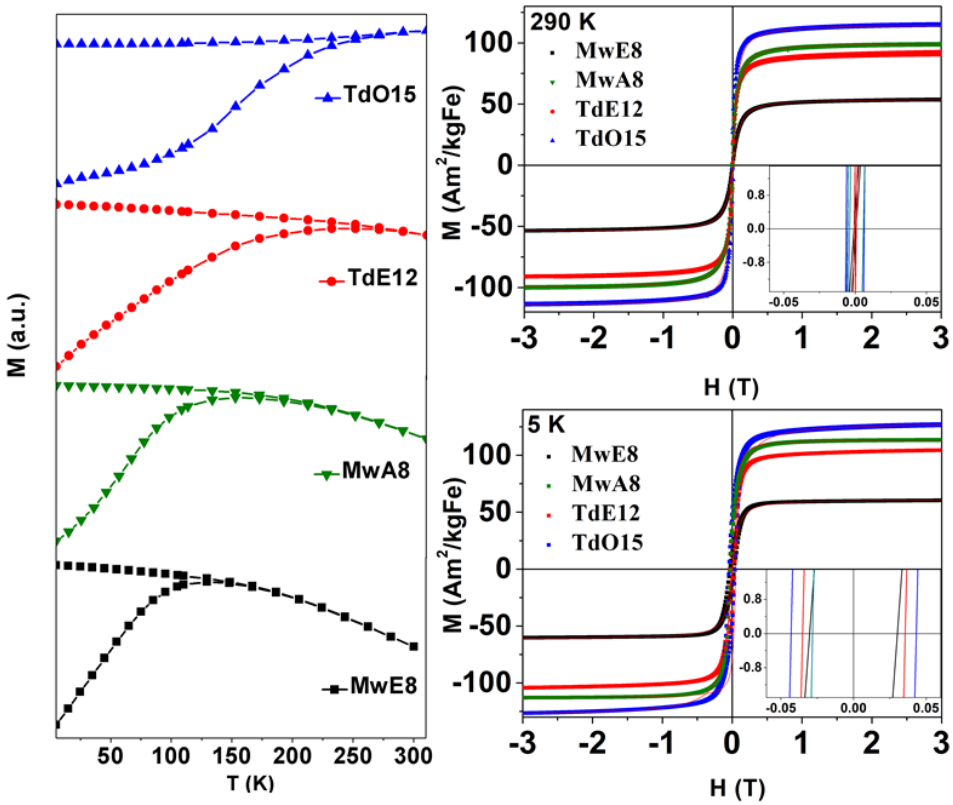

Figure 4.11: Hysteresis loops at room temperature and 5 K and zero field cooled (ZFC)/field cooled (FC) magnetization curves measured at 100 Oe for DMSA coated magnetite nanoparticles obtained by microwave (MW) and thermal decomposition (TD) using different solvents. The loops were fitted by Langevin function. Adapted from [145].

The initial susceptibility values increase as the particle size increases, as the number of magnetic moments that align with the field growth. Magnetic particle sizes calculated from the Langevin function vary from 6.4 nm ($\sigma = 0.33$) for MwE8 up to 8.8 nm for TdO15 ($\sigma = 0.27$), as seen in figure 4.12. The differences between TEM and magnetic size for TD samples suggest a strong surface effect. Comparative values for all the samples can be seen in table 4.1 by the end of the chapter.

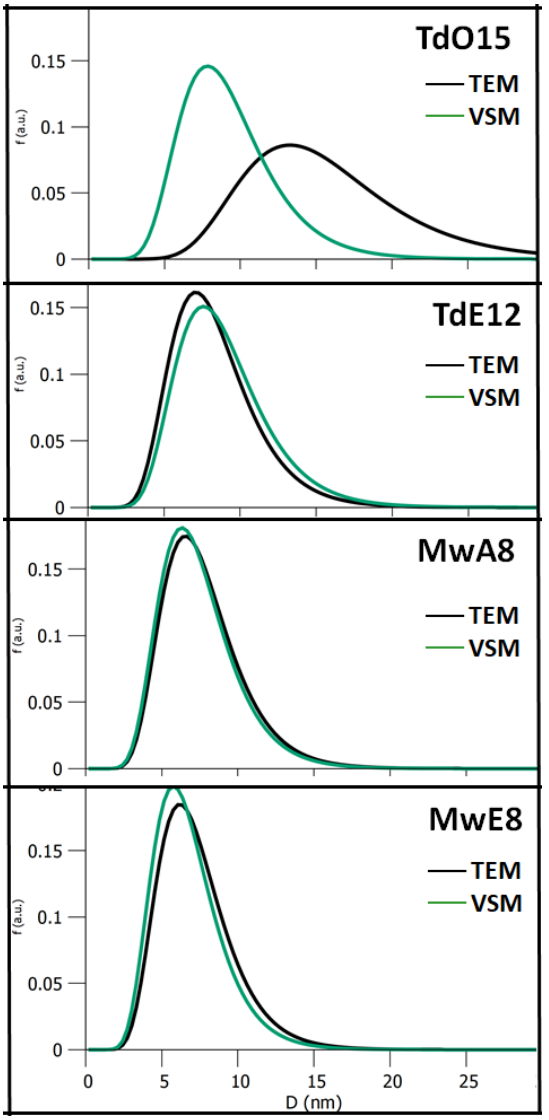

Figure 4.12: Differences in sizes measured by TEM (black curves) or magnetic particles sizes calculated from the Langevin function at room temperature histeresis (green curves), for DMSA coated magnetite nanoparticles obtained by microwave (MW) and thermal decomposition (TD) using different solvents.

Dynamic magnetic behaviour (ACS) has been analyzed in liquid samples. These measurements in liquid allow the samples to preserve both relaxation mechanisms, Brownian and Néel. As shown in figure 4.13, the drop of the real component of the susceptibility (χ') indicates

the existence of a peak in the imaginary part of the curve (χ") [159], that corresponds to the magnetic relaxations of the nanoparticles. In powder, the Brownian relaxation is suppressed, whereas in liquid the Brownian time constant (τ_B) is directly proportional to the viscosity of the medium and the hydrodynamic volume of the particles, as explained in chapter 2. Néel relaxation time (τ_N) is solely determined by the volume of the magnetic core multiplied by the anisotropy constant.

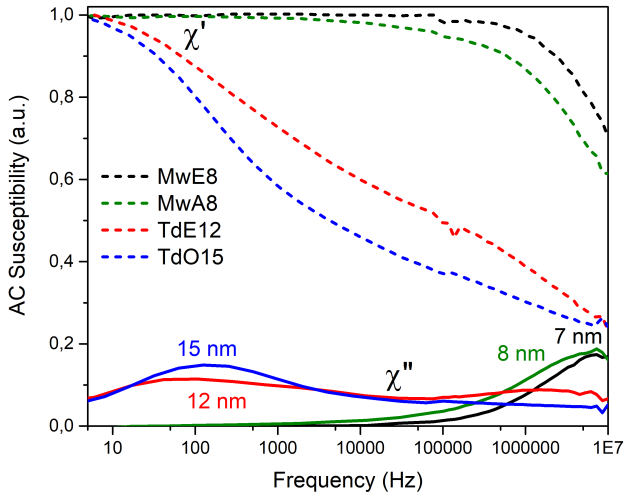

Figure 4.13: Frequency dependence of the low-field mass AC susceptibility showing the real part χ' and imaginary part χ" for the different nanoparticle systems. For ease of visualization, data were normalized such that the maximum χ' values were unity in each case. Excitation field in the range of 30 μT to 500 μT. The leap around 10^5 Hz is given by the fusion of data acquired by two different AC susceptometers.

Larger particles as TdO15 have a Brownian relaxation frequency (the frequency at the maximum in χ") of 144 Hz (figure 4.13, blue curve), or in the case of TdE12, a peak appears at 90 Hz and another at higher frequencies, around 1 MHz (figure 4.13, red curve). None of the real (χ') nor the imaginary (χ") components reach zero susceptibility at high frequencies ($> 10^7$ Hz) indicating the presence of a fast Néel relaxation component for both samples or a portion corresponding to blocked particles [160].

Smaller particles (as MwE8 and MwA8, figure 4.13 black and green curves, respectively) present a peak in the imaginary part of the susceptibility around 10 MHz, which indicates a relaxation time due exclusively to the Néel mechanism.

From measurements on dilutions of the samples (data not shown) no shift in the AC susceptibility peak was found and therefore, no evidence of interactions between the aggregates of particles in the dynamic magnetic response (relaxation frequencies were constant with respect to particle concentration) [139].

Fitting the data to a multi-core model [161] for TdO15 and TdE12 (larger NP), hydrodynamic sizes can be calculated as 131 nm and 74 nm respectively, which are lower than those measured by DLS (173 and 37 nm respectively). Also for smaller nanoparticles, MwE8 and MwA8, it was used the single-core model [161], where it can be calculated the core size, giving 11.4 nm and 11.8 nm respectively. Here for smaller nanoparticles the peak in χ" is not completely visible, hindering the fit, causing distortion on the core size. Details on the fitting models are in chapter 3.

Table 4.1: Comparison of structural and magnetic properties for all samples described on text, to easy access.

	MwE8	**MwA8**	**TdE12**	**TdO15**
Diameter TEM (nm) number	6.9 (0.21)	7.3 (0.21)	7.9 (0.26)	14.8 (0.17)
Diameter TEM (nm) volume	8.1	9	10.5	16.3
Diameter XRD (nm)	7.9	8.5	12.2	15.5
Diameter DLS (nm)	23 (0.2)	68 (0.5)	37 (0.3)	173 (0.3)
Diameter VSM (nm)	6.4 (0.33)	7.1 (0.4)	8.5 (0.29)	8.8 (0.27)
Volume XRD (10^3 nm^3)	2.1	2.5	7.6	15.6
M_s at 5 K(Am^2/kg)	60	114	105	128
M_s at RT(Am^2/kg)	55	100	93	115
H_c at 5 K (10^4 A/m)	2.4	2.2	2.8	3.2
H_c at RT (10^4 A/m)	0.47	0.21	0.18	0.63
Zeta Potential (mV) at pH 7	-34.4	-27.6	-28.3	-32.2
Colloidal Stability (24 h)	0.2%	1.8%	1.5%	0.5%

Diameter DLS = $Z_{average}$ and the number between brackets is the polydispersity index
M_s = saturation magnetization; H_c = coercive field

4.1.5 Partial conclusions

Microwave assisted synthesis has been explored for the preparation of magnetic iron oxide nanoparticles showing the effect of different experimental parameters such as the solvent, the precursor, and the surfactant on the nucleation and growth processes that determine particle size and uniformity. The most suitable solvent for the synthesis was chosen as dibenzyl ether, the optimal ramp was set at 3.75 $^oC/min$, the iron concentration was set as 4 mgFe/ml, and (oleic/Fe) molar ratio was set at 5, giving rise to the most uniform nanoparticles, where size is limited to a maximum of around 10 nm.

For conventional heating the nanocrystals tend to nucleate on the vessel walls first given its inhomogeneous heating profile, in contrast, microwave produces efficient internal heating promoting nucleation everywhere reducing the growth possibilities of the numerous nuclei generated. This is the main limitation of this technique, which is ideal for the production of relatively small nanoparticles, with core sizes around 10 nm.

Magnetic iron oxide nanoparticles with sizes between 8 and 15 nm synthesized by microwave and thermal decomposition in organic media present nearly superparamagnetic behavior at RT, high saturation magnetization and great colloidal stability in water after coating with DMSA.

4.2 Encapsulation of magnetic nanoparticles in liposomes

Liposomes are interesting structures, biocompatible, non - immunogenic and able to encapsulate drugs and nanoparticles, transport them inside the cells and control the cargo release. Nanoparticles encapsulated in liposomes present different spatial distribution depending on the nanoparticle coating. Thus, nanoparticles can be located inside, in the aqueous compartment, in the lipid bilayer, or outside, attached at the liposome surface, resulting in very different aggregation state. Structural, colloidal and magnetic properties have been presented in this chapter. Their localization in the liposome are expected to affect the nanoparticles magnetic properties and consequently their performance in several biomedical applications (MRI contrast media, magnetic hyperthermia and drug delivery).

4.2.1 Preparation of magnetoliposomes

Liposomes with the same lipid composition but prepared by different methods can have different properties, such as stability, size and encapsulation efficiency. In order to produce liposomes, the lipid molecules must be introduced into an aqueous solution. To do so the lipid must be hydrated, increasing the surface-to-volume ratio, normally done by preparing a thin lipid film from evaporation of organic phase or directly introducing the lipid into water by injection, emulsification or solvent dialysis. The methods used in this work are presented below, for more details check chapter 3.

Thin-film hydration is the main method used on this work. It first begin by weighting the dry lipid, which is then dissolved in organic solvent and left to solvate. This mixture is dried by rotatory evaporation until all the solvent has evaporated and formed a continuous film on the bottom of the flask. This film is now hydrated with an aqueous solution at 55 ^oC. The product of this hydration is a large multilamellar vesicle (LMV), analogous to the structure of an onion, where each

lipid bilayer is separated by water. Small unilamellar vesicles (SUV) are produced by breaking these structures by indirect sonication at 55 ^oC. Electron microscopy of liposomes without nanoparticles can be seen in figure 4.14, indicated as "Rotavap" with mean size of 85 nm. Hydrodynamic size in number distribution can be seen in figure 4.15 with mean size of 45 nm. This method in spite of being currently used has the disadvantage of the very low internal volume/encapsulation efficacy and the possible accelerated degradation of phospholipids [105].

Ethanol injection is a classic method for preparation of SUV´s. As described on chapter 3, lipids are dissolved in ethanol, which is then slowly injected into an aqueous solution of the material to be encapsulated. TEM image can be seen in figure 4.14 for liposomes without nanoparticle loading with mean size of 60 nm. Hydrodynamic size in number distribution can be seen in figure 4.15 with mean size of 25 nm. The disadvantage of this technique is the difficulty of withdrawing the ethanol from the blend [136], considering that many biologically active molecules are not compatible with ethanol, not even in small amounts, this represent a serious drawback. Another difficulty of this technique will appear when loading with magnetic nanoparticles is intended, since they precipitate in the presence of ethanol, being hard to obtain a homogeneous mixture.

Freeze-thaw sonication is a straightforward method, where the lipid is directly hydrated with the aqueous solution without the need of formation of a previous film. This method affords to obtain SUV without contamination, because it does not imply the introduction of ethanol or chloroform in the system. The trouble with this method appears when the mixture passes through the extruder, where a great amount of the nanoparticles stay attached to the filter membrane, clogging the pores, resulting in a big waste of magnetic nanoparticles. TEM image can be seen in figure 4.14, for liposomes without nanoparticles encapsulated with mean size of 95 nm. Hydrodynamic size in number distribution can be seen in figure 4.15 with mean size of 65 nm.

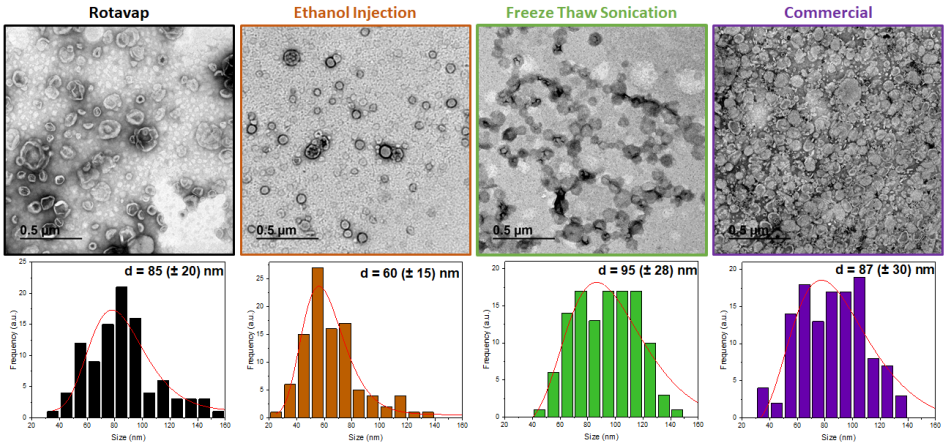

Figure 4.14: Transmission electron microscopy images for different methods of producing liposomes with its respective size distribution below, fitted by Log-normal (red lines): rotatory evaporation (Rotavap, black) mean size 85 nm, ethanol injection (orange) mean size 60 nm, Freeze-thaw sonication (green) with mean size of 95 nm and a commercial one (NanoVex, purple) with mean size of 87 nm, all liposomes presented are without nanoparticles loading.

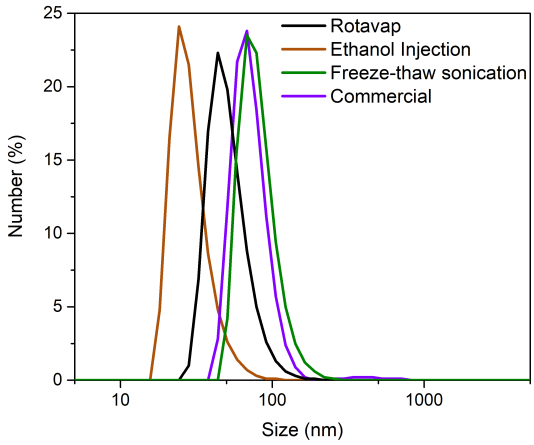

Figure 4.15: Hydrodynamic size in number distribution for liposomes produced by different methods: rotatory evaporation (black) 45 nm, ethanol injection (orange) 25 nm, Freeze-thaw sonication (green) 65 nm and a commercial formulation (NanoVex, purple) with 70 nm, all liposomes presented are without nanoparticles loaded.

Lipo-Cat is a commercial formulation, produced by NanoVex Biotechnologies SL, designed to obtain positively charged liposomes (cationic liposomes). Cationic nanovesicles could be more easily endocyted by cells to achieve intracellular delivery. Besides, liposomes positively charged were used in this case to contrast with the negatively charged liposomes obtained from the methods described above and study its effect on nanoparticle loading. Important note here is the fact that this formulation contains cholesterol in a ratio 1:1 with respect to the phosphatidylcholine, which increases the lipid bilayer stiffness, hindering the hydrophobic nanoparticles loading. TEM image can be seen in figure 4.14, for liposomes without nanoparticles loaded with mean size of 87 nm. Hydrodynamic size in number distribution can be seen in figure 4.15 with mean size of 70 nm. The main advantage of this method is the easy (on the shelf) storage of the solid lipid mixture already sterilized and the fast rehydration process.

4.2.2 Controlling NP spatial distribution

From the methods described above the most suitable one for our purposes (encapsulating NP) was the thin-film hydration, given its versatility when working with hydrophilic or hydrophobic loading. To observe the effect of NP size in the liposome it was chosen 2 core sizes, 8 and 15 nm. To incorporate hydrophobic nanoparticles (coated with oleic acid) into the liposome it is necessary to add them at the beginning of the process along with chloroform. These NP are encapsulated inside the lipid bilayer, as observed in the electron microscopy images 4.16, marked in black. However, to incorporate the hydrophilic nanoparticles (DMSA-coated) it is necessary to disperse the NP in the aqueous medium, following the same protocol described in chapter 3, TEM image can be observed in figure 4.16, marked as light blue. Observing the TEM images it is possible to verify that the NP coated with oleic acid are inside the lipid bilayer, as expected, but for the DMSA coated NP there is no internalization, but an attachment of the NP to the surface of the liposomes, probably due to the negative charge of the DMSA, using DPPC lipids.

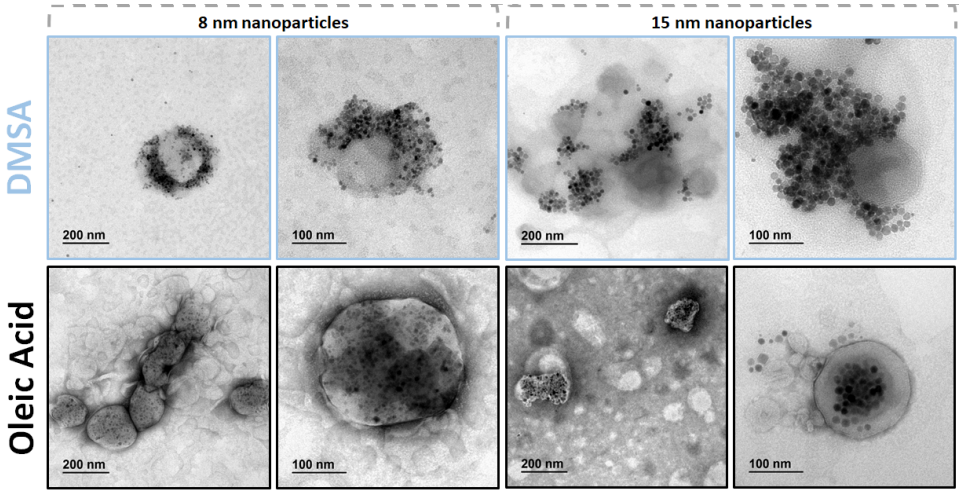

Figure 4.16: TEM images of liposomes produced with small (8 nm) and large (15 nm) nanoparticles coated by DMSA (blue) or oleic acid (black).

Magnetoliposomes hydrodynamic size in aqueous suspensions at pH 7 was measured by dynamic light scattering (DLS). Hydrodynamic sizes in number are adjusted to a monomodal distribution, as seen in figure 4.17, where the smallest mean value corresponds to the liposomes without nanoparticles. Mean value in number distribution for liposomes without NP is 45 nm (with PDI = 0.25), for 8 nm nanoparticles coated by DMSA it is 68 nm (with PDI = 0.25) and for 8 nm nanoparticles coated by oleic acid it is 53 nm (with PDI = 0.2).

For 15 nm nanoparticles coated by DMSA, two peaks appear corresponding to 155 nm and 470 nm (with PDI $>$ 0.7) meaning heterogeneity in size sample, and for 15 nm nanoparticles coated by oleic acid, the mean value is 74 nm (with PDI = 0.22).

When the NP coated with oleic acid are incorporated in the liposome they still maintain its spherical shape, increasing its diameter with respect to the liposome without NP. On the other hand, for nanoparticles coated with DMSA, which stay attached to the surface of the liposome, this result in a broadening and a shift of the peaks to larger sizes. In brief, liposomes loaded with DMSA coated NP are bigger and more polydisperse that liposomes loaded with the same size hydrophobic NP, and in the case of bigger nanoparticles (15 nm) the

differences increase and even a bimodal distribution appears, since this samples were not extruded.

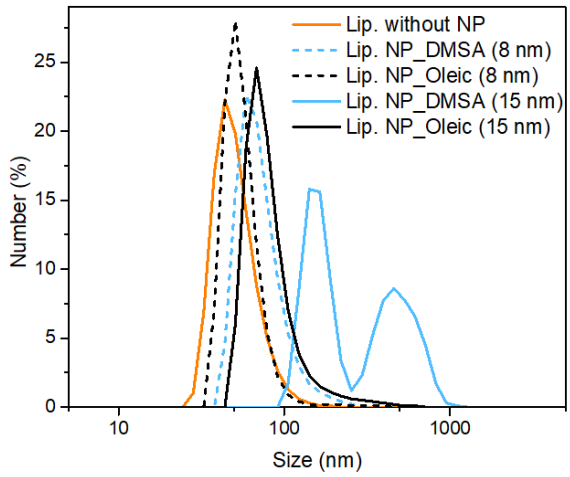

Figure 4.17: Hydrodynamic size in number distribution for liposomes produced by thin-film hydration without nanoparticles (orange curve), with small and large nanoparticles coated by DMSA (dashed and continuous blue line, respectively) or with small and large nanoparticles coated by oleic acid (dashed and continuous black line, respectively).

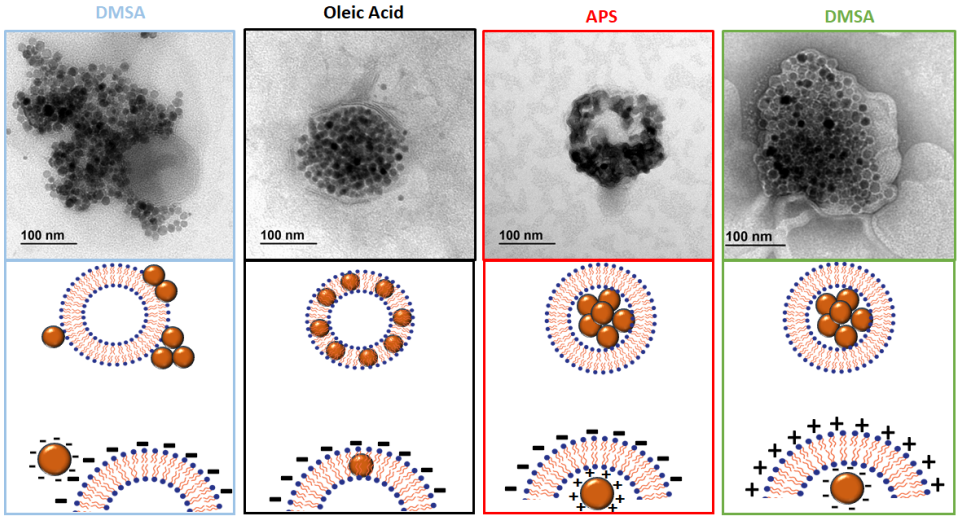

Figure 4.18: TEM images of liposomes produced with nanoparticles using different coatings as DMSA (blue), oleic acid (black), APS (red) or changing the liposome's surface charge to positive (green), producing as a result four different spatial configurations.

To observe the effect of nanoparticle coating on the liposome formation, 15 nm core size nanoparticles was chosen to follow the experiments. Changing the nanoparticles coating offer the possibility to obtain magnetoliposomes with nanoparticles in different spatial distributions. Here it was used iron oxide nanoparticles with three different coatings: APS (positively charged), DMSA (negatively charged) and oleic acid (hydrophobic). The structures that result of this study can be seen in figure 4.18; NP attached to the liposome surface (DMSA coating), NP inside the lipid bilayer (oleic acid coating), NP encapsulated in its aqueous volume (APS coating) and for cationic liposome (positive surface charge) NP are encapsulated in its aqueous volume (DMSA coating). More details on the APS coated nanoparticles are discussed in chapter 4.3.

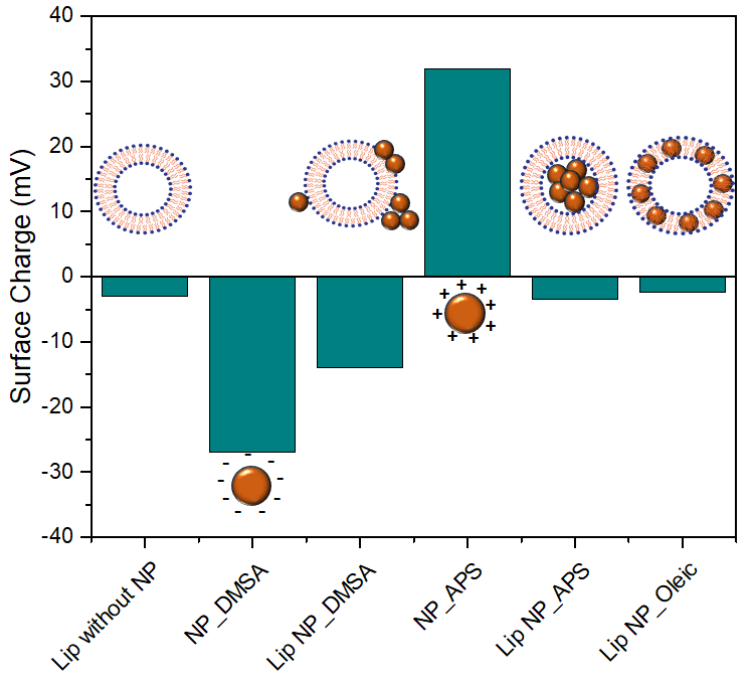

Figure 4.19: Zeta potential measurements at pH 7 for magnetoliposomes produced with nanoparticles coated by DMSA, APS or Oleic acid, and the comparison with the free nanoparticles surface charge.

By comparison of the zeta potentials of these systems at pH 7 it is possible to observe (figure 4.19) that the liposome without nanoparticles has a negative zeta potential of around -3 mV, correspondent to

the usual charge of DPPC lipids. As seen in chapter 4.1 the surface charge of NP coated by DMSA is highly negative, at around −30 mV while for NP coated with APS is highly positive, at around +30 mV. In the case of liposomes with NP coated by DMSA its zeta potential is around −15 mV, which supports the fact that the NP are indeed attached to the surface of the liposome. However, for the liposomes with NP coated by oleic acid and NP coated by APS, the surface charge is around −3 mV for both cases, equivalent to the liposomes without NP, which support the fact that the NP are inside the lipid bilayer (Oleic) or inside the aqueous part (APS) of the liposomes, respectively, as seen in figure 4.18.

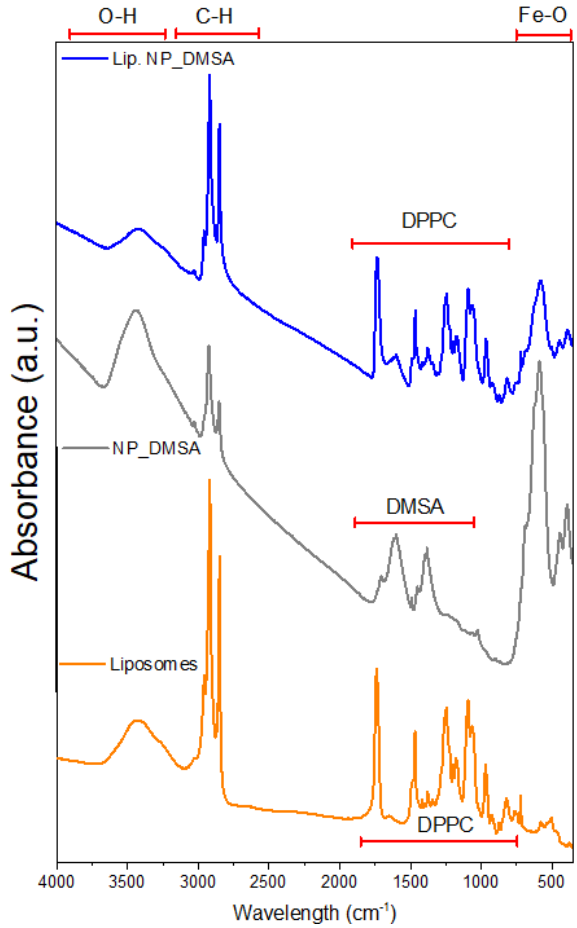

Figure 4.20: Infrared spectra for comparison between nanoparticles coated by DMSA (gray curve), liposomes without nanoparticles (orange curve) and magnetoliposomes with DMSA coated nanoparticles (blue curve).

Infrared spectra are presented in figure 4.20 where it shows the typical bands for water above 3100 cm^{-1}, antisymmetric and symmetric CH stretching between 3000 and 2500 cm^{-1}, signature bands for DPPC phospholipids [162] below 2000 cm^{-1} in the case of liposomes (orange curve) and magnetoliposomes (blue curve). Between 1700 and 1000 cm^{-1} it appears bands for the coating signature (DMSA) for free nanoparticles (gray curve). Finally, bands below 1000 cm^{-1} are associated with the vibration modes of the iron oxide, Fe-O stretching [156], appearing in the curve of free nanoparticles (gray) and magnetoliposomes (blue). For the DMSA sample, bands at 1640 cm^{-1} are due to the vibration of the C=O bond, at 1450 cm^{-1} are due to bending of CH bond and at 1140 and 1000 cm^{-1} broad absorption bands appear owing to the vibration of the bond S-CH. For the DPPC samples a band at 1730 cm^{-1} appears due to C=O bond, bands in the region 1469-1439 cm^{-1} are mainly due to C-H deformation modes from the lipid acyl chains, asymmetric CH_3 stretching mode at around 1377 cm^{-1} and asymmetric and symmetric stretching modes for the PO_2^- group are found near 1250 cm^{-1} and 1085 cm^{-1}, respectively. One important conclusion is that the positions of DMSA bands were not shifted after the loading process indicating the stability of the coating.

For a more in-depth study of the interactions between NP and lipids calorimetri measurements were made, as it can be seen in figure 4.21 (A and B). A peak at 41.6 ^oC is observed for liposomes without particles, corresponding to the fusion transition (or melt transition). In this case the pretransition is not observed, in agreement with the unilamellar vesicles structure observed by TEM (figure 4.16), which contains less cooperativity compared to the multilamellar vesicles [106]. Lipid pretransition is a transition of low enthalpy, below the fusion transition of the lipid chains. It is linked to the formation of periodic waves on the surface of the membrane. Below the pre-transition and above the main transition the surface of the membrane is flat [106]. The lipid chains are tilted in the gel state and at the fusion transition the crystalline order is lost, where the lipid chains become fluid and disordered.

Incorporating DMSA coated NP (8 nm) has shifted the main peak to 40 ^oC, since the NP are attached to the surface of the liposomes perturbing the lipid bilayer slighty, figure 4.21A, blue curve. However,

when incorporating NP of different sizes (8 and 15 nm), covered by oleic acid, the main peak is shifted to even lower temperatures (around 38 ^oC) and a significant broadening appears (figure 4.21B), given the substantial perturbation of the lipid bilayer, as previously observed [162]. It is important to keep the main transition above 37 ^oC to avoid lipid fluidification at body temperatures, when working with bioapplications. Therefore, the magnetoliposome structure chosen to follow the tests with drug delivery, by the end of the chapter, will be with nanoparticles coated with DMSA, where the main transition is at 40 ^oC.

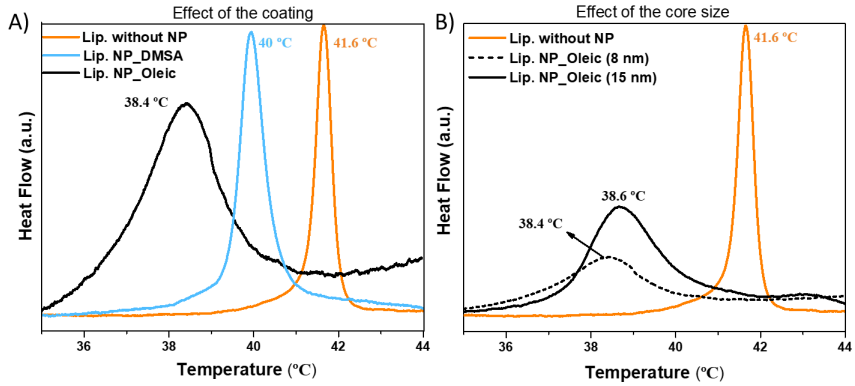

Figure 4.21: DSC measurements of DPPC lipid membranes for liposomes without particles (orange curves), A) with 8 nm nanoparticles with different coatings (DMSA blue curve and oleic acid black curve), B) with nanoparticles coated by oleic acid with different core size (8 nm dashed line and 15 nm continuous line), where the shift of the peak is proportional to the lipid membrane perturbation. Pre-transition peak is not observed.

4.2.3 Effect of NP aggregation on the magnetic properties

DC magnetic properties were analyzed in powder form for DMSA coated nanoparticles and magnetoliposomes. The samples are close to the superparamagnetic regime at 290 K, showing rather low coercive fields. Enlargement of the low-field sections of the curves are shown in the insets to get a more accurate view of hysteresis effects. From figure 4.22 it is also noted that the fact of being encapsulated in li-

posomes changes slightly the nanoparticles DC magnetic behavior at room temperature.

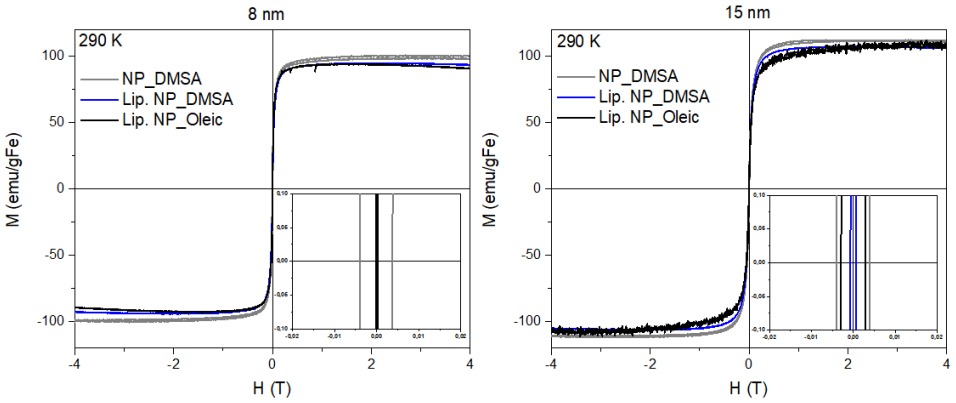

Figure 4.22: Hysteresis loops at room temperature for 8 nm and 15 nm nanoparticles coated with DMSA (black curves) or encapsulated in the liposomes (blue curves).

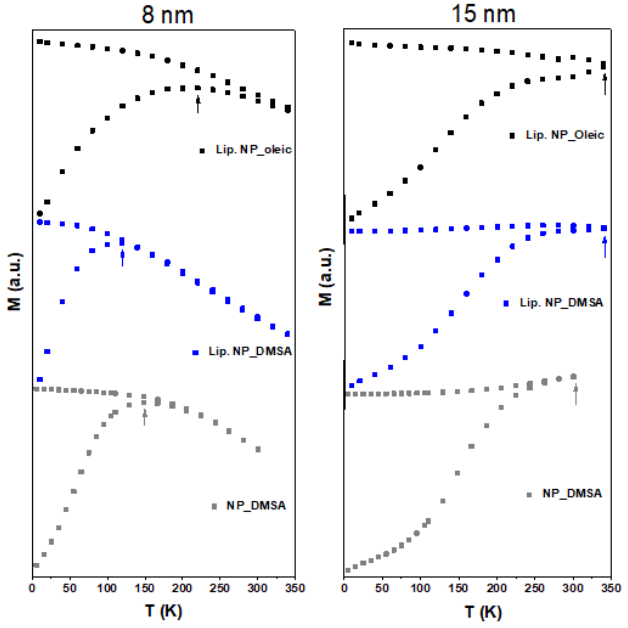

Figure 4.23: Zero field cooled (ZFC)/field cooled (FC) magnetization curves measured at 100 Oe for DMSA coated magnetite nanoparticles of 8 and 15 nm (gray curves), magnetoliposomes with DMSA coated nanoparticles (blue curves) and magnetoliposomes with oleic acid coated nanoparticles (black curves). Arrows indicate the blocking temperature.

The ZFC-FC magnetization curves for both 8 and 15 nm nanoparticles can be seen in figure 4.23 where the blocking temperature is marked with an arrow. It is clear that the bigger NP are still blocked at room temperature while the smaller ones have a T_B at lower temperatures (at around 150 K). The fact of being encapsulated inside the lipid bilayer induces a T_B shift to higher temperatures, indicating an increased aggregation degree in comparison with free nanoparticles [163]. The aggregation degree is higher for oleic acid coated NP given its confinement at the lipid bilayer, in particular for 8 nm NP.

Dynamic magnetic behavior (ACS) has been analyzed in liquid samples and can be seen in figure 4.24. From measurements on dilutions of the samples it was found no evidence of interactions between the particles in the dynamic magnetic response (relaxation frequencies were constant with particle concentration). Small particles coated with DMSA (8 nm) exhibit Néel relaxation, giving that the maximum on the out-of-phase susceptibility component χ" appears above 10 MHz, and a non-zero value of the real part of the AC susceptibility. From the above result, one can fit the data to a single-core Debye model, obtaining a core-size distribution of 11 nm (the difference between TEM and the fit size is probably due to the fact that it is not possible to see the whole χ" peak, which is above 10 MHz, compromising the accuracy of the fit) (data presented in table 4.2). Magnetoliposomes containing small particles show similar results independent on the nanoparticle coating and therefore its configuration, either if nanoparticles are attached to the external surface of the liposome or inside the lipid bilayer (data not shown). The χ" peak in the imaginary part is still above 10 MHz, indicating strict Néel relaxation. Larger particles coated with DMSA (15 nm) present a peak in the imaginary part at about 130 Hz, which is due to a Brownian relaxation of the nanoparticles, figure 4.24. If the AC susceptibility data are fitted to a multi-core model one can estimate a particle hydrodynamic diameter of about 74 nm (table 4.2). Magnetoliposomes with these particles attached to the external surface of the liposome present a peak shift to higher frequencies in the imaginary part, with a pronounced broadening, indicating that indeed there are a Brownian relaxation. The hydrodynamic size given by the multi-core fitting is 180 nm. The peak shift and broadening can be

related to the effect on interaction between nanoparticles when are encapsulated in liposomes and by the polydispersity of the sample, also seen in figure 4.22.

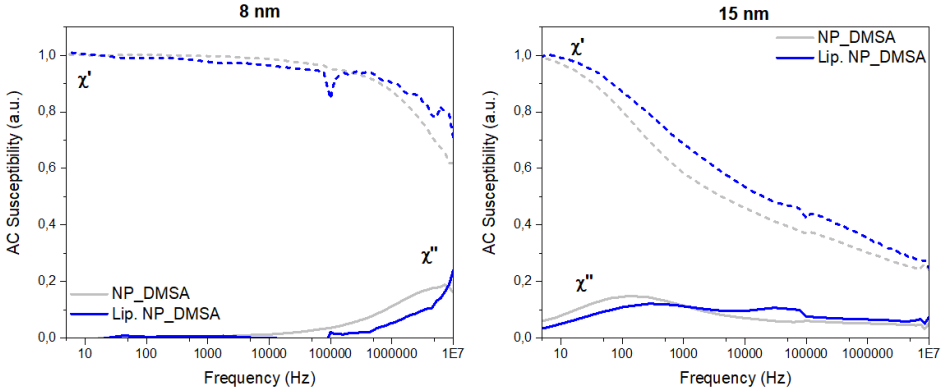

Figure 4.24: Frequency dependence of the low-field mass AC susceptibility showing the real part χ' (dashed lines) and imaginary part χ" (continuous lines) for the nanoparticles coated by DMSA (gray curves) or liposomes with nanoparticles coated by DMSA (blue curves). For ease of visualization, data were normalized such that the maximum χ' values were unity in each case. The leap around 10^5 Hz is an artifact given by the fusion of data acquired by two different AC susceptometers.

Table 4.2: Comparison of structural and magnetic properties for nanoparticles and magnetoliposomes.

	8 nm			**15 nm**		
	NP DMSA	Lip.NP DMSA	Lip.NP Oleic	NP DMSA	Lip.NP DMSA	Lip.NP Oleic
DLS Diameter (nm)	8.6	68	53	58	155+470	74
χ" peak (Hz)	$> 10^6$	$> 10^6$	$> 10^6$	130	≈ 300	$\approx 74 \times 10^3$
ACS Diameter (nm)	11	10	-	74	180	-
T_M (^oC)	-	40	38.4	-	40	38.6

DLS diameter in number. χ" = imaginary component of the AC susceptibility.
T_M = lipid main transition.

For a different perspective data for 15 nm nanoparticles was represented as a function of the coating, as can be seen in figure 4.25. The shift in the χ" peak is clearly observed from free nanoparticles coated by oleic acid (green curve) to those coated by DMSA (gray curve), and its respective magnetoliposomes. From the TEM images (figure 4.16) and DLS data (figure 4.17) it can be noted that magnetoliposomes with nanoparticles inside the lipid bilayer (black curve) have

smaller hydrodynamic size when compared to those magnetoliposomes with nanoparticles attached to the surface (blue curve). The results of this study support the fact that AC magnetic properties of the particles are affected by their spatial distribution when encapsulated by the liposomes and it can be evaluated by the position of the χ' and χ" peaks. In chapter 4.3 it will also be studied the effect of viscosity in NP aggregation.

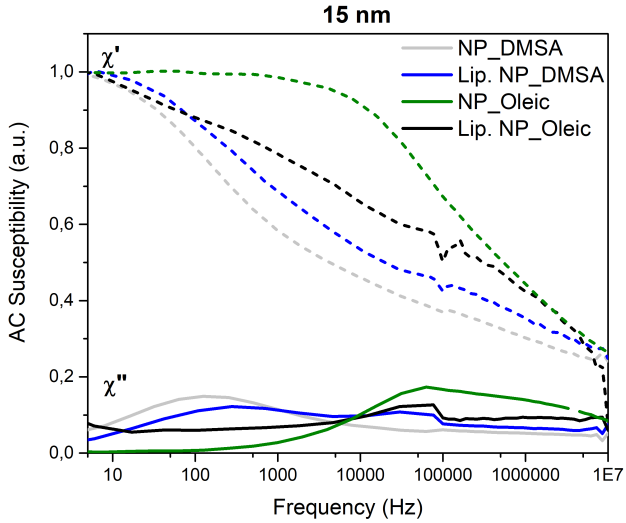

Figure 4.25: Frequency dependence of the low-field mass AC susceptibility showing the real part χ' (dashed lines) and imaginary part χ" (continuous lines) for larger nanoparticles (15 nm) with different coatings (DMSA, gray curves or oleic acid, green curves) and its respective magnetoliposomes (DMSA, blue curve or oleic acid, black curve). The leap around 10^5 Hz is an artifact given by the fusion of data acquired by two different AC susceptometers.

4.2.4 Nanoparticle loading

To evaluate the nanoparticles/liposome ratio we assume first that all liposomes have similar size, as observed by TEM, around 200 nm, and have a unilamellar structure as observed by Cryo-TEM (figure 4.26).

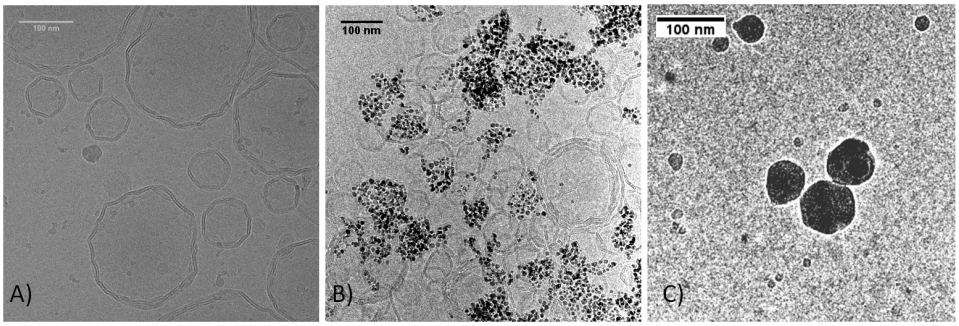

Figure 4.26: Cryo-TEM images of A) liposomes without nanoparticles, revealing mostly spherical unilamellar vesicles, B) liposomes with nanoparticles coated by DMSA, C) and also an example of how liposomes with oleic acid coated nanoparticles appear in this technique. Scale bar = 100 nm.

The number of lipid molecules in a unilamellar liposome is given by

$$N_{tot} = \frac{\left[4\pi\left(\frac{d}{2}\right)^2 + 4\pi\left(\frac{d}{2} - h\right)^2\right]}{a} \tag{4.1}$$

where ,

$$4\pi\left(\frac{d}{2}\right)^2 \tag{4.2}$$

is the area of one monolayer of the liposome, d is the diameter of the liposome, h is the bilayer thickness and a is the lipid head group area. In this work, for DPPC liposomes, we assume $h = 5\ nm$ and $a = 0.71\ nm^2$ [164]. So the number of lipid molecules in a 200 nm size liposome is about 336.000. Given the quantities used in this work (10 mg of DPPC), we have in around 2.5×10^{13} liposomes in the suspension.

For 8 nm nanoparticles and taking into account the quantities used in this work (chapter 3), the amount of nanoparticles is around 2.6×10^{15} per sample. Therefore, we have around 105 nanoparticles per liposome. For 15 nm nanoparticles, and the quantities used in this work, the amount of nanoparticles is around 4×10^{14} per sample. The

relation would be around 16 nanoparticles per liposome. These values agree with those reported previously, showing that liposomes of around 100 nm have been loaded with around 60 particles of 7.7 nm average size [56] while for 40 nm liposomes and 16 nm particles, there were around 6 particles encapsulated per liposome [165]. The comparison of nanoparticles per liposomes is complicated given that liposomes and nanoparticles have different sizes. It should be noted that the maximum loading theoretically, considering liposomes of 200 nm of internal cavity and nanoparticles of 8 nm, knowing that the maximum random packings of spheres is 65 % [166], then the highest amount of nanoparticles inside the liposome would be 10156 ($0.65 * 200^3/8^3 = 10156$). Doing the same thing for 15 nm nanoparticles the theoretical maximum would be 1540.

The loading could also be estimated by the mol of iron per mol of lipids ratio, which in this work is around 6.9. Values around 1 have been reported for small particles of around 7 nm (0.53 [56] and 1.6 [167]) while much larger values, 19, have been reported for 16 nm nanoparticles [165]. The issue here is the independence of liposome size of the number of lipids molecules per iron.

We must keep in mind that these type of estimations are qualitative because we cannot discard the presence of free liposomes as observed by TEM images (figure 4.26) and few free nanoparticles. Also note that DMSA nanoparticles stay attached to the surface of the liposome, where the loading is not being limited by the volume of the liposome itself. Finally we must keep in mind that in real samples there is a size distribution, therefore the calculations are only estimates.

4.2.5 Partial conclusions

It was developed a the methodology for obtaining magnetoliposomes in a reproducible manner, with distinct spatial distribution of the nanoparticles depending on the NP coating. The difference depends on both the particle and the liposome surface charges. Thus, for DPPC liposomes, the nanoparticles can be attached to the liposome surface (negative NP coating as DMSA), inside the lipid bilayer

(hydrophobic NP coating as oleic acid) or encapsulated in its aqueous volume (positive NP coating as APS). Hydrodynamic size of liposomes with DMSA coated NP are higher than liposomes with oleic acid coated NP given that in the first case the nanoparticles are attached to the surface deforming the usual spherical shape of the liposomes, while with the oleic acid the liposomes still maintain their original spherical format. Sizes vary from around 100 nm for liposomes without nanoparticles to around 200 nm when nanoparticles are incorporated.

The temperature of the lipid bilayer melt transition is affected by the incorporation of nanoparticles, shifting the peak from 41.6 ^oC (no particle) to 40 ^oC (DMSA particles) or around 38 ^oC (oleic acid nanoparticles), with a significant broadening indicating a substantial perturbation of the lipid bilayer.

Differences in magnetic properties are appreciated by DC measurementsby the increase in T_B. By AC measurements in liquid the effect of the encapsulation was followed, where a peak shift in the imaginary part of the susceptibility (χ") is observed when nanoparticles are encapsulated by liposomes, indicating a Brownian relaxation for larger nanoparticles, which is associated with the higher hydrodynamic size of magnetoliposomes. Smaller nanoparticles (below 8 nm) only exhibit fast Néel relaxation, with a χ" peak above 10 MHz, which remains almost unaltered after its encapsulation in liposomes.

4.3 Interaction between cells and magnetic nanoparticles compared with magnetoliposomes

Once the nanoparticles are internalized into cells some aggregation occurs affecting its performance and metabolization [168]. This alteration has already been observed in cancer therapy based on magnetic hyperthermia, where insufficient heating is generated by nanoparticles once internalized by cells, probably as a consequence of NP aggregation [20]. The objective of this chapter is to develop a model able to mimic the aggregation degree and the spatial distribution of nanoparticles in biosystems and compare their magnetic properties with real biological examples. For that the magnetic properties of three systems with different spatial distribution of nanoparticles was compared. First one being iron oxide nanoparticles (NP) of 14 nm with two coatings (DMSA and APS), the second system being magnetoliposomes, which have different configurations depending on the NP coating (NP attached to the liposome surface or encapsulated in its aqueous volume) and the last system, in which two cell lines (Pan02 and Jurkat) are incubated with the nanoparticles.

4.3.1 NP spatial distribution in cells and magnetoliposomes

The three systems with different spatial distribution of nanoparticles were characterized in this chapter. The first one consists on iron oxide nanoparticles, synthesized by coprecipitation, with a core size of 14 nm ($\sigma = 0.2$) as calculated by TEM (figure 4.27 A and B).

Core size determined from the XRD spectra is 12.3 nm (figure 4.27 C). Infrared spectra of these nanoparticles show the typical bands for water above 3100 cm^{-1}, at 3000 cm^{-1} for $C-H$ vibration, between 1000 and 1700 cm^{-1} for the coating signature and bands below 1000 cm^{-1} associated with the vibration modes of the iron oxide, $Fe-O$

stretching (figure 4.27 D) [156]. The sharp peak at 1387 cm^{-1} of $N-O$ stretching evidences that the sample with nanoparticles coated by APS contained nitrate rests due to the acid treatment during nanoparticle synthesis (check chapter 3 for more details). Nanoparticles coated by APS or DMSA result in hydrodynamic sizes of 220 nm ($\sigma = 0.2$) and 80 nm ($\sigma = 0.2$), respectively, at physiological pH (figure 4.28). Surface charge at pH 7 of the coated particles is over +30 mV for APS coated particles and -31 mV for the DMSA coated ones, as shown in figure 4.28.

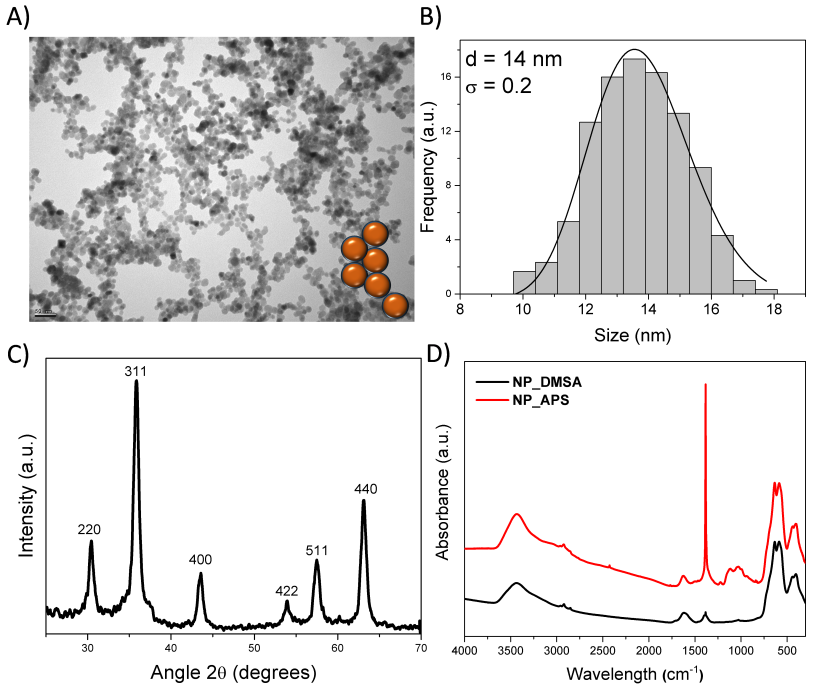

Figure 4.27: A) TEM image of the nanoparticles. b) Size distribution fitted by a Log-normal function, where the mean size is 14 nm. C) X-ray diffraction pattern for the nanoparticles. D) Infrared spectra for DMSA and APS coated nanoparticles. Reproduced from [163].

The second system consists on magnetoliposomes with nanoparticles coated by DMSA or APS, presenting a completely different configuration under the TEM as seen in chapter 4.2, with NP encapsulated in the aqueous volume of the liposome (APS) or attached to the liposome surface (DMSA), due to the NP surface charges at pH 7 (figure 4.28). The mean size by TEM in both cases is around 100 nm with

a wide size distribution (data not shown). Hydrodynamic sizes of the magnetoliposomes go from 400 nm ($\sigma = 0.4$) for those containing APS coated NP to 880 nm ($\sigma = 0.3$) for the DMSA coated NP. Liposomes without particles present hydrodynamic sizes of around 100 nm (figure 4.28), already discussed on chapter 4.2.

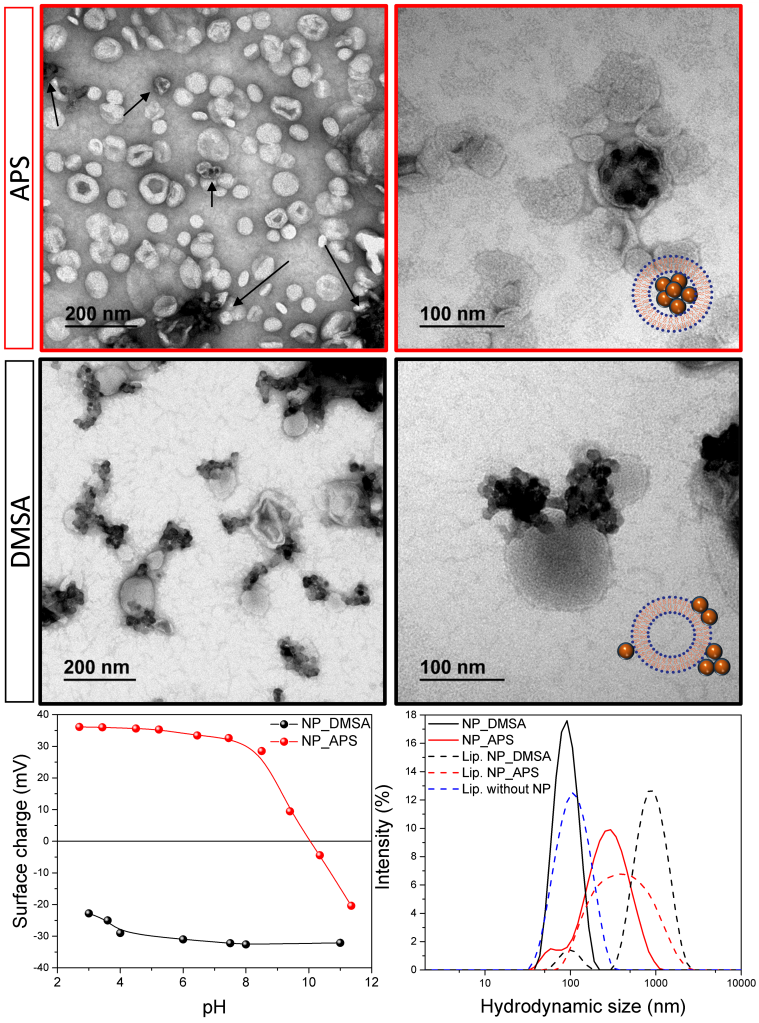

Figure 4.28: TEM images of the magnetoliposomes with the particles inside the aqueous volume (NP coated by APS) or attached to the surface (NP coated by DMSA). Hydrodynamic size in intensity, for the nanoparticles and the magnetoliposomes and zeta potential measurements as a function of pH for both DMSA and APS coated nanoparticles. Reproduced from [163].

The third system studied in this work for comparison were cells incubated with NP (with both DMSA or APS coating). Two cell lines were chosen: Pan02 (murine pancreatic ductal adenocarcinoma) and Jurkat (human T-lymphocyte). Pan02 cells internalize the nanoparticles and confine them into endosomal/lysosomal compartments, which are intracellular enzyme-containing organelles tasked with degrading material unessential for cell maintenance (figure 4.29). However, Jurkat cells almost do not internalize the nanoparticles, occurring instead an attachment of the nanoparticles on the outer cell membrane, thus obtaining, in a natural way, two distinct aggregation systems (figure 4.29).

Internalization process of the APS coated nanoparticles in Pan02 cells starts with the attachment of the nanoparticles to the plasma membrane after 30 min incubation time (figure 4.29 A). The incubation for longer periods (24 h) led to particle confinement into endolysosomes (figure 4.29 B) [139]. DMSA coated nanoparticles also ended up in the lysosomal compartments at a lesser extent, i.e. they never fill the total volume of these endocytic compartments (figure 4.29 C) [157], [169], [170]. The control of NP location in cells was previously achieved by controlling the incubation temperature, using 4 ^oC to inhibit the internalization or 37 ^oC to fully internalize the nanoparticles [20]. On the other hand, Jurkat cells maintained the APS coated nanoparticles adhered to their plasma membrane and hardly endocyted them (figure 4.29 D). Indeed, APS coated nanoparticles were grouped in a single region of the cell membrane as observed in the confocal microscope (figure 4.30). White spots due to the magnetic nanoparticles can be distinguished in both images located at different cell regions, in the cytoplasm for Pan02 and outside the cell membrane for Jurkat cells (figure 4.30 A and B).

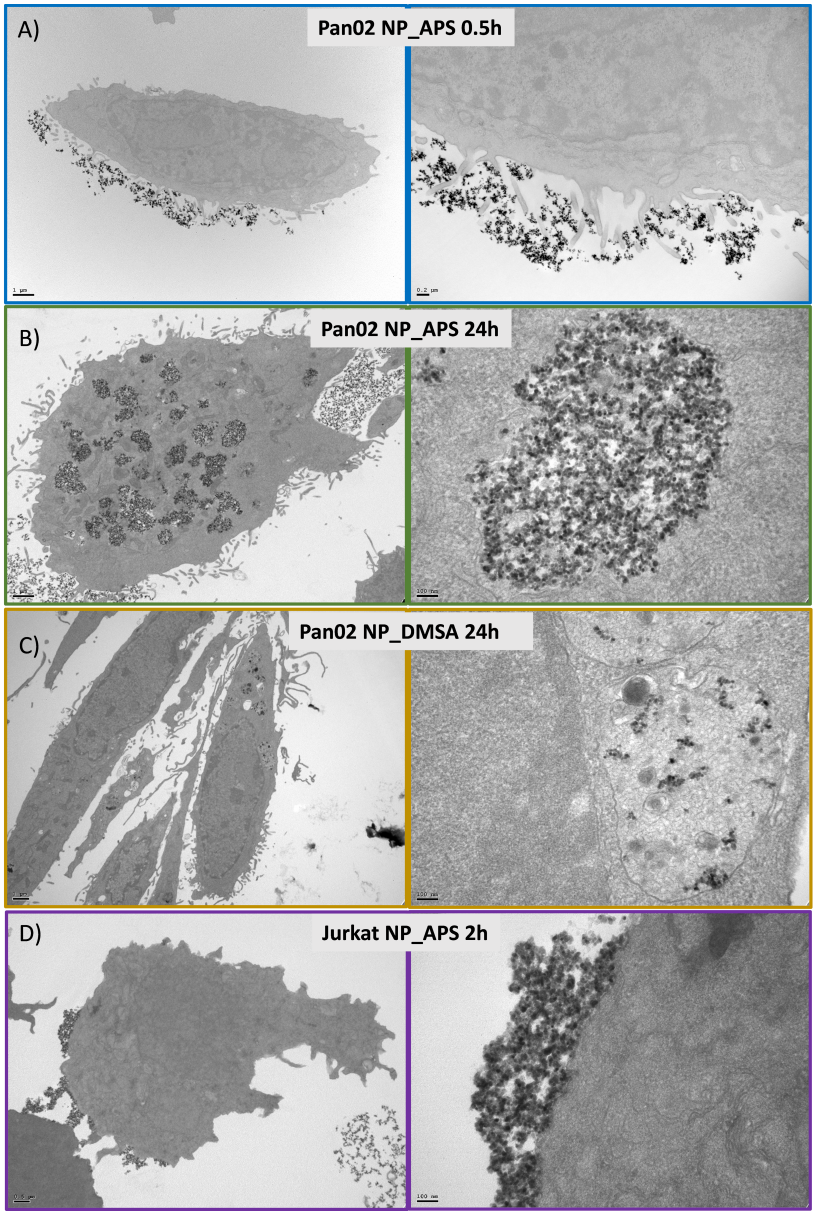

Figure 4.29: TEM images from thin sections of different cell lines incubated with nanoparticles. A) Pan02 NP-APS incubated for 0.5 h. B) Pan02 NP-APS incubated for 24 h. C) Pan02 NP-DMSA incubated for 24 h. D) Jurkat NP-APS incubated for 2 h. Reproduced from [163].

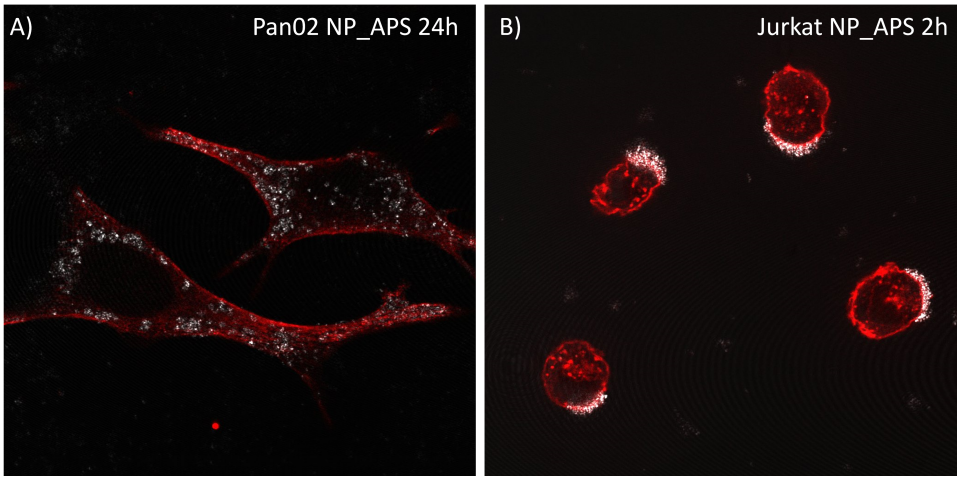

Figure 4.30: Confocal microscopy of A) Pan02 cells incubated for 24 h with NP-APS, red (tubulin), white (NP). B) Jurkat cells incubated for 2 h with NP-APS, red (plasma and Golgi membranes), white (NP). Reproduced from [163].

4.3.2 Comparison of magnetic properties between magnetoliposomes and cells incubated with NP

DC magnetic properties were analyzed in powder form for DMSA and APS coated nanoparticles, magnetoliposomes and cells incubated with these nanoparticles as can be seen in figures 4.31 and 4.32.

Samples are close to the superparamagnetic regime at room temperature as previously shown for nanoparticles prepared by other methods and magnetoliposomes (figure 4.22), showing rather low coercive fields. Enlargement of the low-field sections of the curves are shown in the insets to get a more accurate view of hysteresis effects.

Saturation magnetization values and coercive field at low and room temperature remain unchanged independently on the spatial distribution of nanoparticles, for all samples. This means that there is no evident nanoparticle degradation inside the cells for these periods of incubation time and therefore, the changes in the magnetic behavior could only be due mainly to aggregation. The observed small varia-

tions of the M_s value may be due to the error in the iron quantification [171]. As an example, nanoparticle degradation was not observed in macrophages [139] nor in stem cells endosomes over 3 days [18]. For murine model a degradation process over more than a week has been reported, due to nanoparticle disaggregation or reduction in nanoparticle size [172], [3].

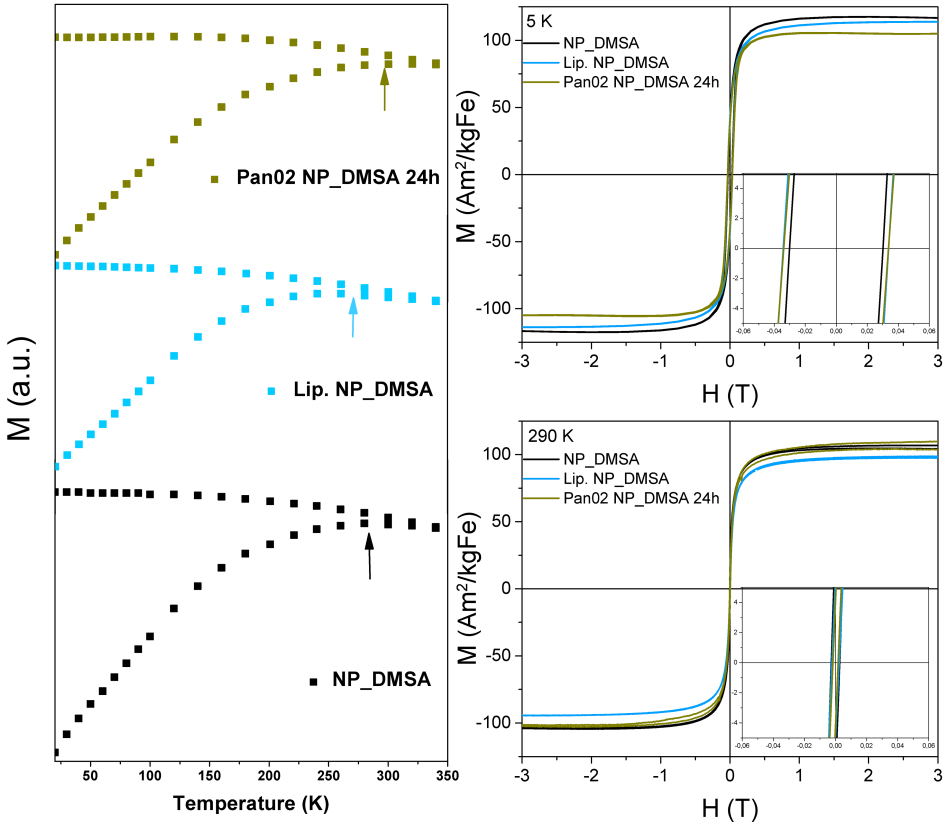

Figure 4.31: ZFC and FC magnetization curves and hysteresis loops at 5 K and room temperature for nanoparticles coated with DMSA (black), encapsulated in the liposome (light blue) and incubated with Pan02 (yellow). Reproduced from [163].

Figures 4.31 and 4.32 shows also the field dependent magnetization at room temperature and 5 K, likewise the zero-field cooled (ZFC) and field cooled (FC) curves of the samples containing free nanoparticles, magnetoliposomes and cells incubated with nanoparticles. At room temperature the ZFC and FC curves join up indicating a superparam-

agnetic behavior above this temperature.

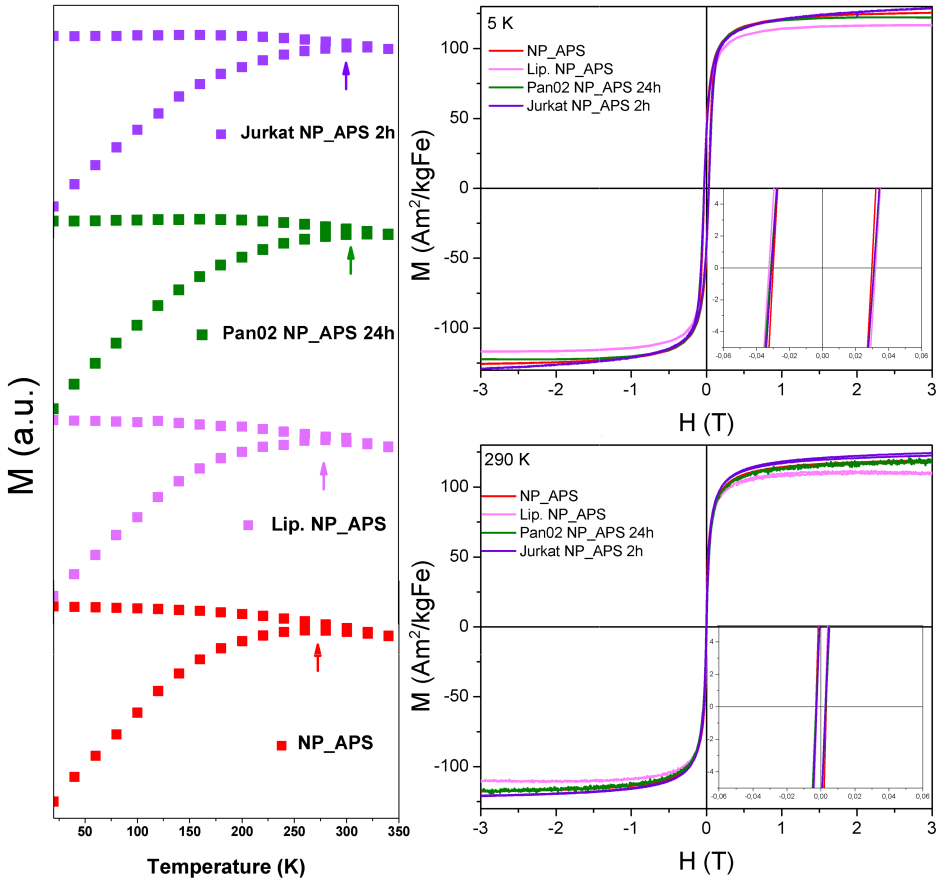

Figure 4.32: ZFC and FC magnetization curves and hysteresis loops at 5 K and room temperature for nanoparticles coated with APS (red), encapsulated in the liposome (pink) and incubated with Pan02 (24 h) (green) and Jurkat (2 h) (purple) cell lines. Reproduced from [163].

Blocking temperature (T_B) was determined from the maximum of the ZFC measurement and it was observed that nanoparticles in cells, regardless of its location, the incubation time, the cell line or the nanoparticle coating present a larger blocking temperature than free nanoparticles and magnetoliposomes (figure 4.33). This suggests that the simple fact of being in contact with the cells makes the nanoparticles aggregate. It can be seen that sample Pan02 NP-APS 24 h shows the highest T_B in agreement with the TEM images, which exhibit larger aggregates (figure 4.29). The effect of the intra- (short distance) and

inter-aggregate (long distance) magnetic dipolar interactions may result in magnetizing and demagnetizing effects [173]. Clustering formation after nanoparticle internalization into cells may enhance short-range magnetic dipolar interactions which could explain the difference in T_B values. This is in agreement with the data previously reported [174], [175], in which T_B increases as intralysosomal density of NP rises. It should be noted that this effect could not be observed in the hysteresis measurements.

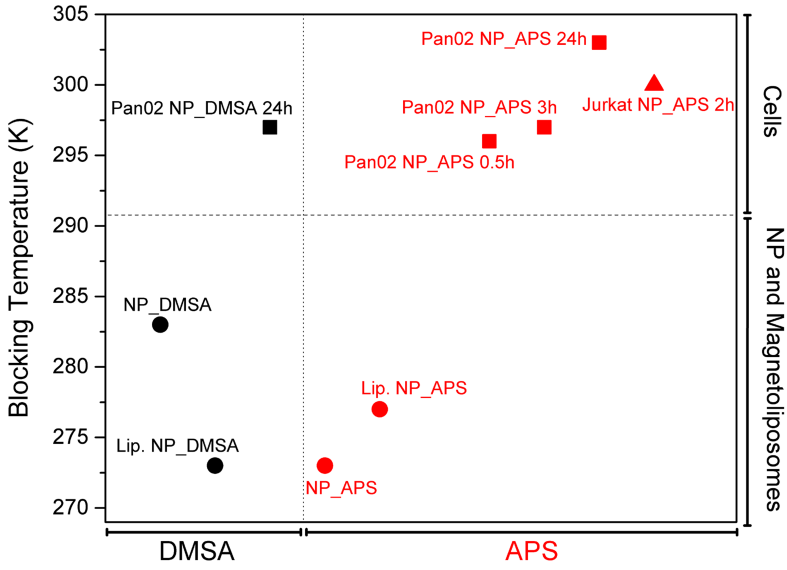

Figure 4.33: Blocking temperature determined from the maximum of the ZFC measurements for the different systems, including free particles, magnetoliposomes and cells incubated with NP. Reproduced from [163].

Dynamic magnetic behaviour (ACS) has been analyzed in liquid, allowing the samples to preserve both relaxation mechanisms, Brownian and Néel. As seen in figure 4.34, the drop of the real component of the susceptibility (χ') indicates the existence of a peak in the imaginary part of the curve (χ"), for more details check chapter 2 [159]. From measurements on dilutions of the samples (data not shown) no shift in the AC susceptibility peak was found and therefore, there is no evidence of interactions between aggregates of particles in the dynamic magnetic response (relaxation frequencies were constant with respect to particle concentration) [139].

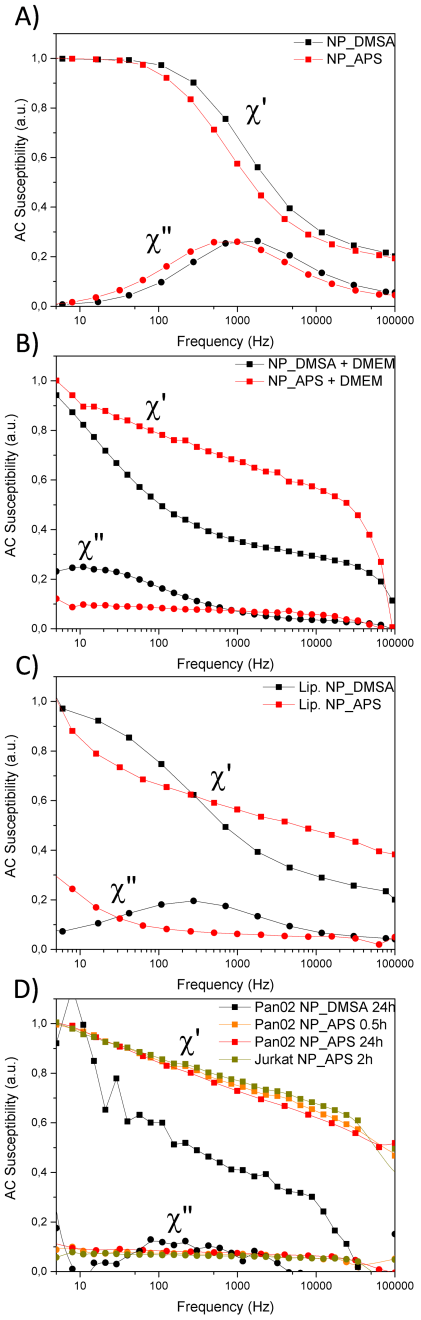

Figure 4.34: Frequency dependence of the low-field mass AC susceptibility showing the real part χ' and imaginary part χ" for the different systems. For ease of visualization, data were normalized such that the maximum χ' values were unity in each case. Excitation field of 0.5 mT. Reproduced from [163].

Nanoparticles coated by DMSA in water have a Brownian relaxation frequency (the frequency at the maximum in χ") at 1285 Hz that shifts to 243 Hz when encapsulated in liposomes (figures 4.34 A and C, black curves). None of the real (χ') nor the imaginary (χ") components reach zero susceptibility at high frequencies ($> 10^7\ Hz$) indicating the presence of a fast Néel relaxation residual component or it could be related to the blocked NP in the system [160]. When these measurements were performed in culture medium, the χ" peak (at the Brownian relaxation frequency) moves to lower frequencies ($< 10\ Hz$), indicating an even larger aggregation state than the one presented by the liposomes (figure 4.34B, black curve). The formation of a protein corona when particles are in contact with cell culture media has been reported to lead to an increase in the hydrodynamic size of the nanoparticles [172]. The differences in ionic strength and the binding of proteins from the media to the particle surfaces are responsible for this effect [176]. Once the nanoparticles are internalized in cells (Pan02 with 24 h incubation time), the peak of χ" has a pronounced broadening at around 100 Hz, indicating the presence of aggregates heterogeneous in size (figure 4.34D, black curve). A peak in χ" at the same frequencies was previously observed for lysed cells containing citric-coated nanoparticles of similar size [160]. Fitting the data to a multi-core model [161], hydrodynamic sizes of 68 nm ($\sigma = 0.1$) for the nanoparticles coated by DMSA and 118 nm ($\sigma = 0.1$) for the magnetoliposomes were obtained, which are lower than those measured by DLS (data presented in table 4.3).

Table 4.3: Comparison of structural and magnetic properties for nanoparticles, magnetoliposomes and cell lysosomes.

Coating	**DMSA**		**APS**		**NP DMSA**	**NP APS**		
Samples	NP	Lip.NP	NP	Lip.NP	Pan02 24h	Pan02 0.5h	Pan02 24h	Jurkat
DLS Diameter (nm)	80	880	220	400	-	-	-	-
χ" peak (Hz)	1285	243	754	16	≈ 100	≈ 100	≈ 100	≈ 100
ACS Diameter (nm)	68	118	82	986	-	-	-	-
T_B (K)	283	273	273	277	297	296	303	300

DLS = Dynamic Light Scattering. χ" = imaginary component of the AC susceptibility. T_B = Blocking temperature.

In the same manner, for the nanoparticles coated by APS in water the Brownian relaxation frequency (χ") is at 754 Hz that shifts to 16 Hz when encapsulated in the liposome indicating in fact an aggregation

state higher than in the case of the free particles (figures 4.34 A and C, red curves). When measured in culture medium the peak resembles the ones of the cells, very broad AC response, not being able to clearly identify the relaxation peak (figure 4.34B, red curve). The origin of this increase in hydrodynamic particle size is the clustering effect due to the protein corona [114], [115], [117]. Once the NP-APS are internalized by the cells (Pan02 with 0.5 h and 24 h or Jurkat for 2 hours incubation time) the χ" peak shifts to lower frequencies (figure 4.34D, reddish curves) and shows the pronounced AC response broadening already seen for the DMSA samples, due to polydispersity in the aggregate sizes of the particles. As it was mentioned before, a drop in the χ' curve at the relaxation frequency gives a peak in the χ" curve, even though it is very broad as seen in figure 4.34D. This broadening of the χ" peak seems to be independent on the incubation time, the cell line and the nanoparticle coating, suggesting once again that the simple fact of being in contact with the cells makes the nanoparticles aggregate, as previously indicated by the blocking temperature shift in figure 4.33.

Despite the fact that the nanoparticles aggregation in the cells looks completely different in the TEM images (figure 4.29) (NP on the cell membrane or confined into cell lysosomes) they behave in a similar way when compared from the magnetic point of view (figure 4.34). From the fit of the AC susceptibility data, hydrodynamic sizes of around 82 nm ($\sigma = 0.1$) were obtained for NP-APS sample and 986 nm ($\sigma > 0.5$) for the magnetoliposomes, which is, in the case of NP-APS, lower than the value obtained by DLS (data presented in table 4.3). Higher for magnetoliposomes, the value obtained by AC susceptibility is higher than DLS value, due to the fact that the peak in the χ" curve is not completely visible (figure 4.34C), hindering the fit. The fits for the cell curves did not result satisfactory given the noise in data due to low iron concentration of the cell samples.

Dynamic magnetic response of iron oxide nanoparticles with different core sizes (11 and 21 nm) can be found in the bibliography [177], where χ" also shows values near zero across the overall measured frequency range for nanoparticles inside cells ($MCF-7$), independently of the core size. It was also seen [160] a peak χ" shift to lower frequencies when nanoparticles (10 nm) were dispersed in cell culture medium,

in agreement with our data.

To determine if the nanoparticles preferential orientation during cellular aggregation could be the cause of the magnetic behavior observed in AC susceptibility, the nanoparticles aggregates were isolated from lysosomes and its orientation analyzed using bright and dark field transmission electron microscopy (figure 4.35).

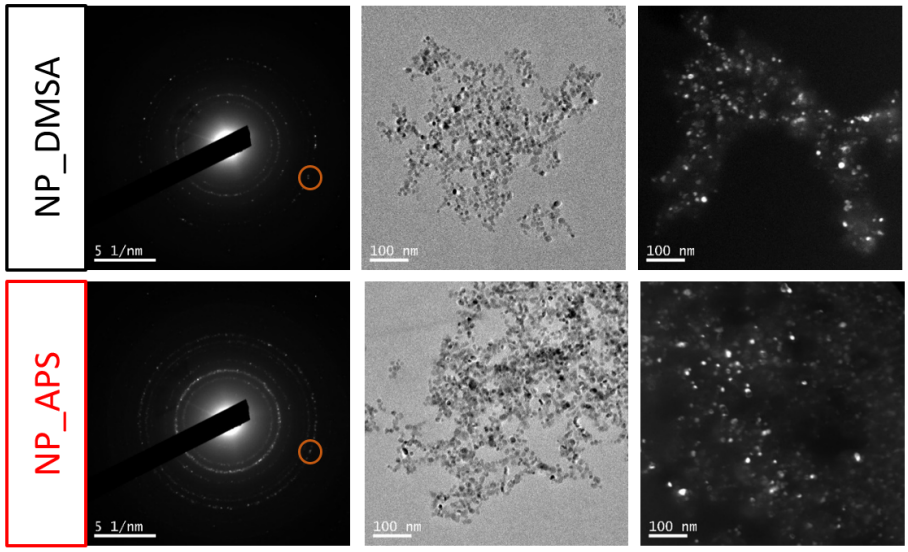

Figure 4.35: Electron diffraction patterns assigned to a spinel iron oxide structure (on the left), bright field images (central) and dark field images obtained by tilting the electron beam, for both nanoparticles coated by DMSA or APS obtained from Pan02 lysossomes. Adapted from [178].

This technique is used to locate and identify crystalline nanoparticles in complex biological matrices [179]. The incident electron beam is tilted an angle that corresponds to the direction of the diffraction and the nanoparticles with the same crystallographic orientation appear bright. The NP-APS aggregates from Pan02 lysosomes are analyzed in bright field mode, appearing as dark. On the other hand, for dark field mode the nanoparticles, corresponding to the direction of the selected diffraction, appears bright. It can be observed that bright spots with sizes similar to the particles are dispersed over the aggregate with random orientation. The same behavior is obtained for NP-DMSA aggregates. The nanoparticles aggregation in a non-controlled way causes

the magnetic behavior of a very broad χ" peak in AC susceptibility. Concluding, the formation of large oriented aggregates or even chains are not observed, as reported in [178].

4.3.3 Partial conclusions

Aggregation states of magnetic nanoparticles in biosystems have been analyzed in three systems with different spatial distribution of the nanoparticles, i.e. iron oxide nanoparticles positively (APS) and negatively (DMSA) coated, magnetoliposomes and cells.

DC measurements in powder indicates that the saturation magnetization values and coercive field at low and room temperature remain practically the same independently on the spatial distribution of nanoparticles. This means that there is no evident degradation of the nanoparticles inside the cells for the periods of incubation time applied in this work. Also, the blocking temperature of cells incubated with nanoparticles, regardless of the location in which they are, the incubation time, the cell line or the nanoparticle coating, is greater than the blocking temperature of the free nanoparticles and the magnetoliposomes, indicating that the simple fact of being in contact with the cells makes the nanoparticles randomly aggregate, there are differences in the aggregation state when is caused by the contact with the cell medium or inside the liposomes.

Finally, AC susceptometry in liquid was used to probe the magnetic relaxation mechanisms of the nanoparticles in these complex systems. The results demonstrate that the biological environment significantly influences the dynamic magnetic response of the nanoparticles. These results could explain bibliographic data on the heating efficiency and MRI relaxivity of nanoparticles in contact with the cells [20], [174].

4.4 Evaluation of nanoparticles and magnetoliposomes for biomedical applications

Some biomedical applications are presented in this chapter, such as the study of magnetic nanoparticles and magnetoliposomes efficiency as negative contrast agents for Magnetic Resonance Imaging (MRI), for magnetic hyperthermia treatment and as vehicles for drug delivery. MRI experiments were carried out with samples in water for different iron concentrations, followed by phantom evaluation and finally *in-vivo* in mice models, injecting free nanoparticles and magnetoliposomes through the tail vein. Magnetic hyperthermia was also studied first for samples in water with different field frequencies, both free nanoparticles and magnetoliposomes and then, taking into account the previous results, the best combination was tested *in-vitro* in HeLa (human cervical cancer) and MDA-MB-231 (human breast cancer) cells. The viability tests were initially conducted in HeLa cell line for both free nanoparticles and magnetoliposomes finding the optimal iron concentration, time and procedure in general to perform the tests. Drug release was monitored as a function of time, temperature, applied magnetic field and dialysis for samples in water and also tested in MDA-MB-231 cells. It should be emphasized that drug delivery using magnetoliposomes allows combining the magnetic heating to control the drug release and the use of MRI to follow the treatment and biodistribution (or degradation) of the magnetic nanoparticles.

4.4.1 Nanotoxicity limits

For the viability study, HeLa cell line (human cervical cancer cells) was chosen because it is very common in nanotoxicity evaluations providing a good basis for comparison with bibliographic data [180], [181], [182], [183], [169]. These analysis are mandatory before evaluating the material for bioapplications. Tests are done in a standard model to bare solid results (ISO 10993-5:2009(E)).

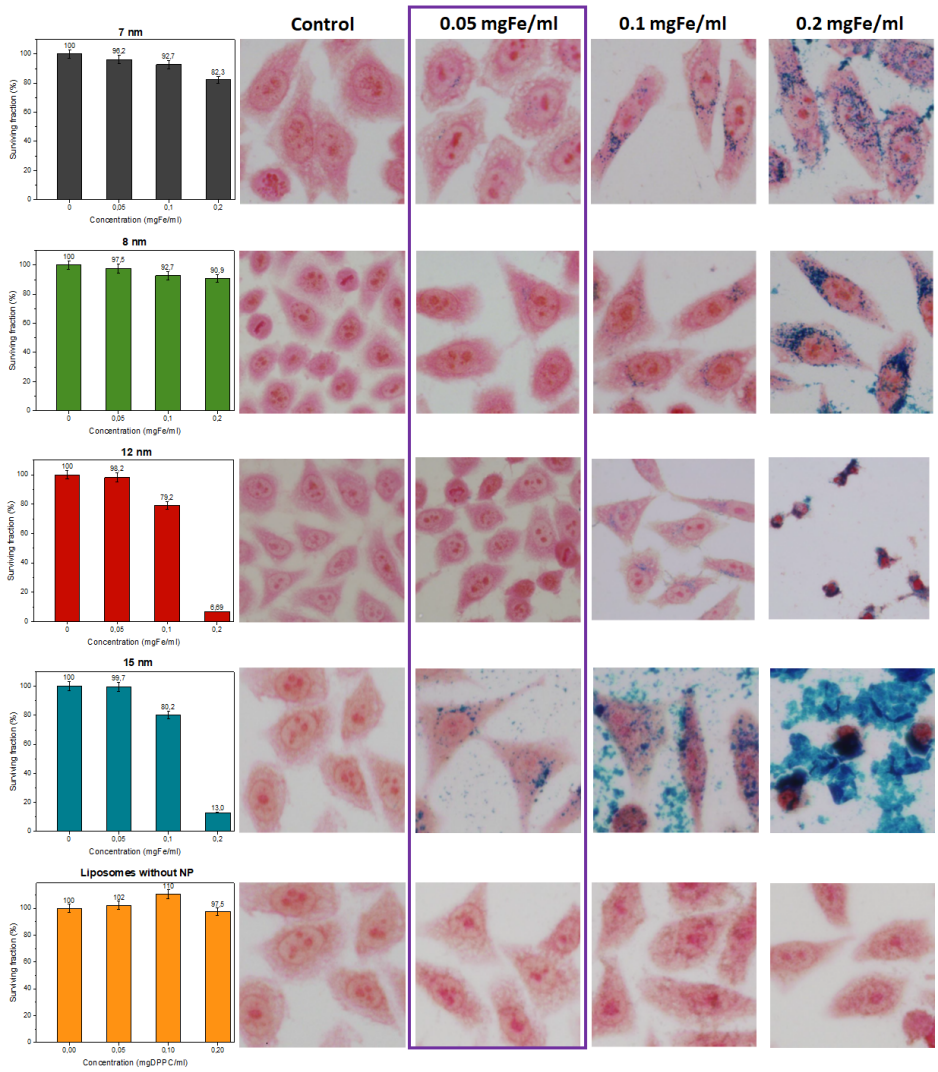

Figure 4.36: HeLa cells incubated for 24 h with different core sizes magnetic nanoparticles (from 7 to 15 nm) and visualized by optical microscopy, for different iron concentrations. Cells stained with Prussian blue reaction for iron oxide detection. Toxicity evaluation by MTT assay. Optimal iron concentration stablished as 0.05 $mgFe/ml$.

Cells were incubated with different iron concentrations (from 0.05 up to 0.2 mgFe/ml) for different nanoparticle core sizes, from 7 up to 15 nm, coated by DMSA and also liposomes without nanoparticles, to use as a control. All data can be seen in figure 4.36, with its respective surviving fraction and microscope images showing cells dyed

with Prussian Blue to highlight the internalization of the nanoparticles. The ideal concentration was defined as 0.05 mgFe/ml by the viability study, where more than 95 % of the cells survived the nanoparticle exposure and some nanoparticles were indeed internalized, given the blue color present in the microscopy images. Smaller nanoparticles are less toxic than larger ones, and bare liposomes do not present toxicity when tested within the first 10 days of the synthesis. After that some toxicity is observed due to lipid degradation, as previously reported [105].

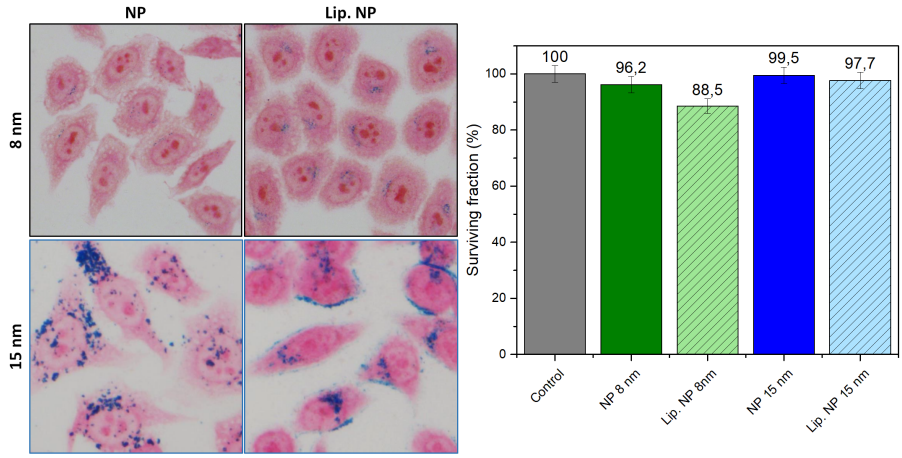

Figure 4.37: Optical microscopy for HeLa cells incubated for 24 h with NP (8 or 15 nm) and with magnetoliposomes. Cells stained with Prussian blue reaction for iron oxide detection. Toxicity evaluation by MTT assay with concentration of 0.05 mgFe/ml.

To follow up the tests with HeLa cells two core sizes were chosen, 8 and 15 nm, both encapsulated in the liposomes, in order to evidence the differences due to magnetoliposome formation. In figure 4.37 it can be seen microscopy images of HeLa cells incubated for 24 h with NP and magnetoliposomes, at a concentration of 0.05 mgFe/ml, with both 8 and 15 nm core sizes. Cells were stained with prussian blue where is evident the nanoparticles internalization. Through incubation of cells with DMSA coated nanoparticle loaded liposomes it was observed that these nanoparticles were able to enter and accumulate at the cytoplasm with 100 % efficiency, in other words, all cells were marked with nanoparticles. The magnetoliposome actually increases intracellular

absorption when compared to isolated nanoparticles, without altering cell viability as can also be seen in figure 4.37.

It is known that cellular uptake is influenced by the nanoparticles size, shape, chemical composition and surface coating, as mentioned in chapter 2 [118]. The internalization of negatively charged nanoparticles has been previously observed even though positively charged nanoparticles are most effective, which could also lead to higher toxicity levels [116]. Negatively coated (DMSA) 11 nm core size iron oxide nanoparticles were tested with six different mammalian cell lines and entered into all, being distributed in vesicles in cytoplasm but with different iron loading [184]. Iron oxide nanoparticles (positively charged) with 10 nm in HeLa cells were found intracellularly, mainly in endosomes, especially, in several large multivesicular structures, identified as late endolysosomes [185]. At a concentration of 0.5 mgFe/ml, HeLa cytoplasm is found to be full of nanoparticles (negatively charged) aggregated around the nucleus (but never inside the nucleus) [169], [186]. Also magnetoliposomes in spite of their bigger size were capable of binding to and being internalized by HeLa cells. After 60 minutes it was bound to the cell surface and after 180 minutes they were internalized [187]. In other cell lines as human breast adenocarcinoma (MCF-7) magnetoliposomes containing 9 nm iron oxide nanoparticles (in the lumen), showed intracellular vesicles (namely endosomes) filled with nanoparticles in more extent when compared to free nanoparticles [46].

4.4.2 MRI relaxation properties in-vitro and in-vivo

As seen in chapter 2 iron oxide nanoparticles are used in clinical practice as a T_2 contrast agent. Nanoparticles are magnetically saturated when the magnetic field used for MRI scanners is applied, perturbing the water proton relaxation which leads to a shortening of T_2 signal. The relaxivity (r) is defined as the slope of the relaxation rate in s^{-1} ($1/T_1$ or $1/T_2$) versus the iron concentration in mM, which gives a direct measurement of the nanoparticle efficiency. High val-

ues of r_2/r_1 are characteristic of T_2 contrast agents, where the organs appear darker in the image. Low values of r_2/r_1 define T_1 contrast agents, where images are clearer and brighter [4]. In this section it is presented the results obtained for the nanoparticles and magnetoliposomes efficiency as MRI contrast agents (nanoparticles with different core sizes as in chapter 4.1 and chapter 4.2). MRI relaxation times (T_1 and T_2) were measured at different iron concentrations from 0 to 0.07 mMFe to obtain the relaxivity value (r_1 and r_2), as seen in figure 4.38, for more details on the equipment consult chapter 3. The maximum r_1 value (20.9 $mM^{-1}s^{-1}$) was found for a TD (thermal decomposition) sample, while the maximum r_2 value (222 $mM^{-1}s^{-1}$) was found for a MW (microwave) sample. Samples obtained by TD with the largest particle size (TdO15) present extremely low r_1, and consequently much higher r_2/r_1 ratio probably given its larger hydrodynamic size (figure 4.9C). Otherwise, samples synthesized by MW have similar r_1 values but sample MwA8 presents more than double r_2 value, indicating higher efficiency as negative contrast agent. In the literature, the maximum experimental value reported for r_2 is around 500 $mM^{-1}s^{-1}$ for iron oxide nanoparticles, while the theoretical maximum value is 750 $mM^{-1}s^{-1}$ (for 55 nm iron oxide cores), not yet reached [188]. Higher values are achieved when working with a composition of zinc and manganese ferrite or dense magnetite clusters [189]. Commercial products using magnetic nanoparticles for pathology diagnosis in the liver and spleen, as *Feridex*®, produced by Berlex Laboratories and *Resovist*®, produced by Bayer Healthcare have r_1 and r_2 values between 24 and 150 $mM^{-1}s^{-1}$ and r_2/r_1 of around 4-6 [190]. Comparing the relation between r_2 and r_1 for the samples presented in this work, it can be observed that samples MwA8 and TdO15 have good possibilities to become T_2 contrast agents, with a quotient of 28 and 72, respectively (see table 4.4).

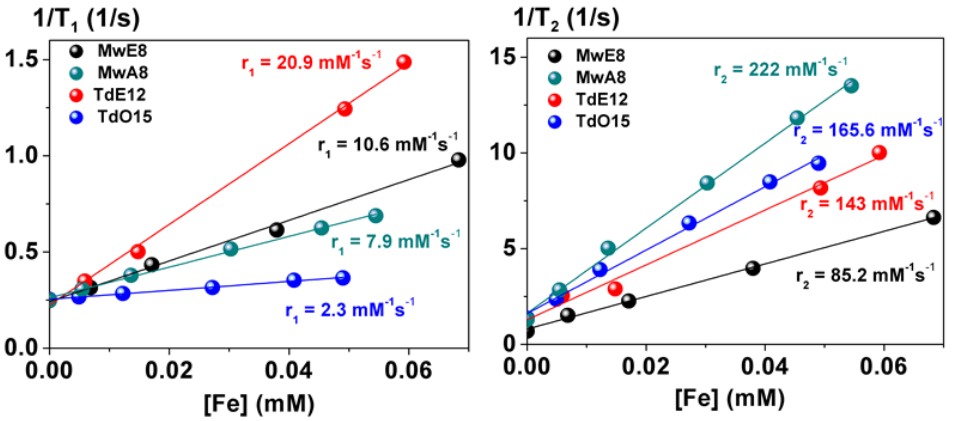

Figure 4.38: MRI T_1 and T_2 relaxation times as a function of the Fe concentration for DMSA coated magnetite nanoparticle suspensions obtained by microwave (MW) and thermal decomposition (TD) using different solvents. Adapted from [145].

Table 4.4: Relaxivity values r_1 and r_2 for free nanoparticles with different core sizes.

	r_1 $(mM^{-1}s^{-1})$	r_2 $(mM^{-1}s^{-1})$	r_2/r_1
MwE8	10.6	85.2	8
MwA8	7.9	222	28
TdE12	20.9	143	6.8
TdO15	2.3	165.6	72

r_2 = MRI transversal relaxivity; r_1 = MRI longitudinal relaxivity.

Given the results from the free nanoparticles presented above, the two best possibilities to work as MRI contrast agents are MwA8 that now will be referred as just "8 nm" and TdO15 that will be referred as "15 nm", to facilitate the reading. These nanoparticles are coated by DMSA or oleic acid and are attached to the surface of the liposome or inside the lipid bilayer, respectively as showed in TEM image 4.16. Similarly to the results of free nanoparticles the relaxation times for magnetoliposomes were measured at concentrations from 0 to 0.07 mMFe and the obtained data can be seen in figure 4.39. The maximum r_1 value (11 $mM^{-1}s^{-1}$) was found for 8 nm nanoparticles coated by DMSA attached outside the liposomes surface, given that T_1 sig-

nal require immediate contact with the water molecules due to the inherent mechanism of spin–lattice relaxation [191]. The maximum r_2 value (381 $mM^{-1}s^{-1}$) was found for 15 nm nanoparticles also coated by DMSA and attached to the liposome, given its bigger hydrodynamic size and the large moment per particle [192], where the intrinsic mechanism of spin–spin relaxation produces this effect. For the samples with oleic acid coating, the water molecules can hardly come into contact with the magnetic core because of the hydrophobic nature of the layer, leading to very low r_1 values. The ratio r_2/r_1 for all the samples is presented in table 4.5. The high quotient values, indicates that the suspension could be high efficient T_2 contrast agents.

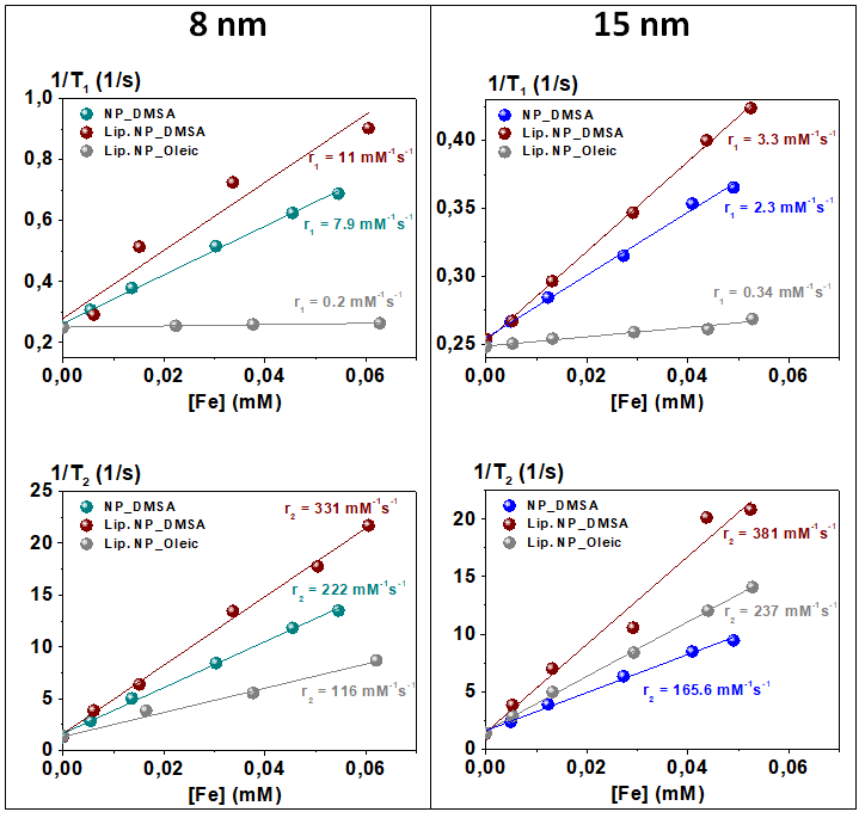

Figure 4.39: MRI T_1 and T_2 relaxation times as a function of the Fe concentration for DMSA coated magnetite nanoparticles (Green for 8 nm and blue for 15 nm), magnetoliposomes with nanoparticles coated by DMSA (red curves) and magnetoliposomes with nanoparticles coated by oleic acid (gray curves), all using 8 and 15 nm core sizes of nanoparticles.

Comparing with other works, 7 to 10 nm NP present r_2 values between 70 and 140 $mM^{-1}s^{-1}$ [188], [149], [193], while 15 nm NP have r_2 values between 140 to 210 $mM^{-1}s^{-1}$ [188], [194]. For magnetoliposomes with small nanoparticles r_2 values vary between 60 and 150 $mM^{-1}s^{-1}$ [195], [196], [56], while for larger nanoparticles r_2 values are up to 232 $mM^{-1}s^{-1}$, where $r_2/r_1 = 35$ [197]. The r_2/r_1 values for our magnetoliposome samples are higher than the reported ones indicating a better efficiency as T_2 contrast agents.

Table 4.5: Relaxivity values r_1 and r_2 for nanoparticles and magnetoliposomes.

	r_1 $(mM^{-1}s^{-1})$	r_2 $(mM^{-1}s^{-1})$	r_2/r_1
NP_DMSA (8 nm)	7.9	222	28
Lip. NP_DMSA (8 nm)	11	331	30
Lip. NP_Oleic (8 nm)	0.2	116	580
NP_DMSA (15 nm)	2.3	165.6	72
Lip. NP_DMSA (15 nm)	3.3	381	115
Lip. NP_Oleic (15 nm)	0.34	237	697

r_2 = MRI transversal relaxivity; r_1 = MRI longitudinal relaxivity.

Liposomes with nanoparticles coated by oleic acid tend to precipitate faster than the other configurations due to low surface charge, destabilizing the system. This is also the case of liposomes with 15 nm nanoparticles coated by DMSA with surface charge comparable to free nanoparticles, magnetic interaction between liposomes aggregates them, forming clusters and finally precipitating. This effect is a serious problem when working with *in-vivo* tests, where the obstruction of veins must be avoided. Given this fact the next tests on MRI will be conducted only on the 8 nm nanoparticles coated by DMSA, both free and encapsulated in the liposome.

From the results of relaxivity values measured in a 1.5 T relaxometer at 37 ^oC, it was checked the capacity of these systems as negative contrast agent for MRI, in a standard test called Phantom. To do this, images were taken for 8 nm nanoparticles at different concentrations of iron and magnetoliposomes with the same nanoparticles, where the re-

sult can be seen in figure 4.40. After performing a T_2 sequence a great negative contrast was achieved that increased with iron concentration. It can be seen a slight enhance signal for the magnetoliposomes in comparison with the free nanoparticles (darker circles), in agreement with the data shown in table 4.5.

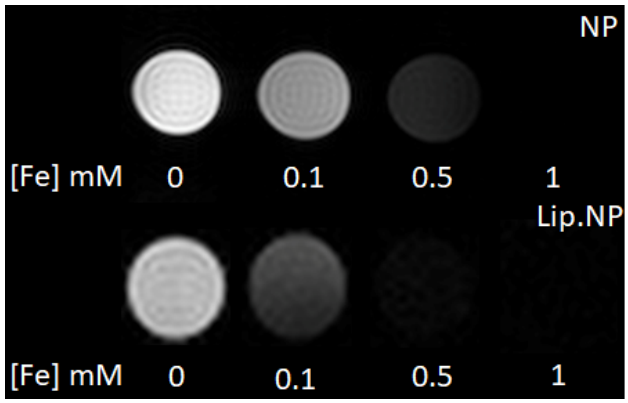

Figure 4.40: Phantom images of T_2 contrast in MRI for NP (8 nm) and magnetoliposomes with different iron concentrations.

The next step was to test the NP and magnetoliposomes *in-vivo*, taking MRI images of rats after injecting them through the tail vein. An accumulation of free nanoparticles was observed in the liver after only 5 minutes post-injection (figure 4.41), due to their darkening, typical for the presence of nanoparticles as evidenced by the phantom image 4.40. These measurements were obtained in a 7 T MRI from 0 to 60 minutes after injection. Usually iron oxide nanoparticles are used in a clinical MRI to determine liver diseases because they are selectively absorbed by Kupffer cells in the liver, spleen and bone marrow [198]. Typical dark images in T_2 contrast due to iron oxide nanoparticles are commonly seen in the literature for murine analysis [199].

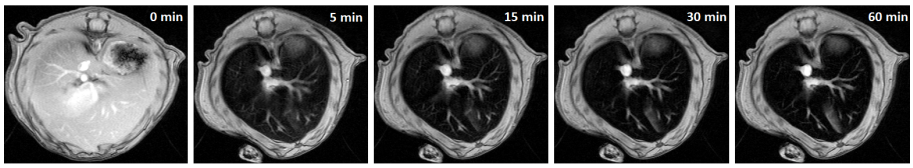

Figure 4.41: Magnetic resonance axial images of the evolution of the T_2 contrast of a mouse liver at increasing times after intravenous injection of magnetic nanoparticles with 8 nm core.

However, when injecting magnetoliposomes in rats some difficulties were detected. Problems of stability due to the larger hydrodynamic size, higher mass in relation to the surface charge, the stability is reduced in comparison with free nanoparticles. Also, for the tests *in-vitro* water was used as the solute, while working with a mouse it is mandatory to make the mixture 5 % in mannitol prior to the injection. As a consequence some clusters are formed inside the syringe, distorting the iron concentration actually injected into the murine blood system. This can be seen in figure 4.42 where only a slight dark contrast change is observed due to the accumulation of these magnetoliposomes in the liver, 60 minutes post-injection. This appears to be contradictory with respect to the measurements presented in figure 4.40, which indicate the structures of magnetoliposomes with greater potential as negative contrast agents. To clarify this issue further studies should be performed to stabilize the magnetoliposomes long enough to perform the MRI measurements, as for example by coating with PEG [195], [196].

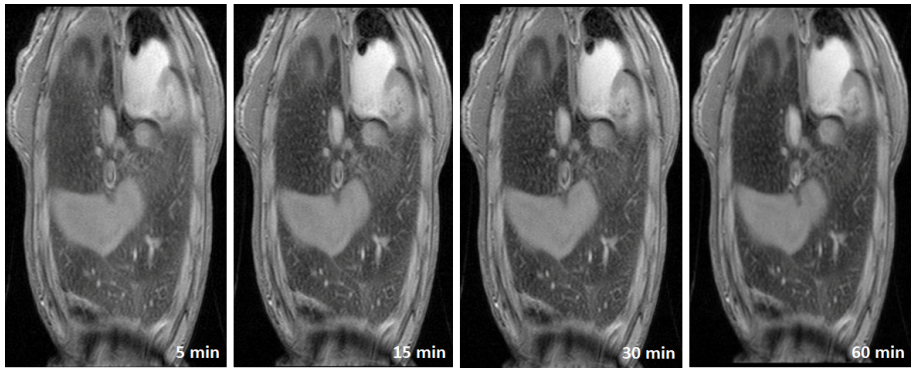

Figure 4.42: Magnetic resonance coronal images T_2 contrast of a mouse liver at increasing times after intravenous injection of magnetoliposomes with 8 nm core nanoparticles.

Other aspects such as circulation time and elimination pathways are important parameters when designing tracers for image and for a possible therapeutic use and they should be also analyzed when the modification of the magnetoliposome surface is successful, making it suitable for *in-vivo* tests .

4.4.3 Magnetic hyperthermia efficiency

To achieve the temperature increase of body tissue, described in chapter 2, as the specific case of magnetic hyperthermia, one important parameter is the choice of appropriate nanoparticles. The idea is to achieve maximum efficiency with minimal side effects, in other words, administer the minimum amount of nanoparticles able to increase the temperature of the cells inducing their death. To do so all the nanoparticles presented in this thesis were tested for their Specific Absorption Rate (SAR), more details on the measurements can be found in chapter 3.

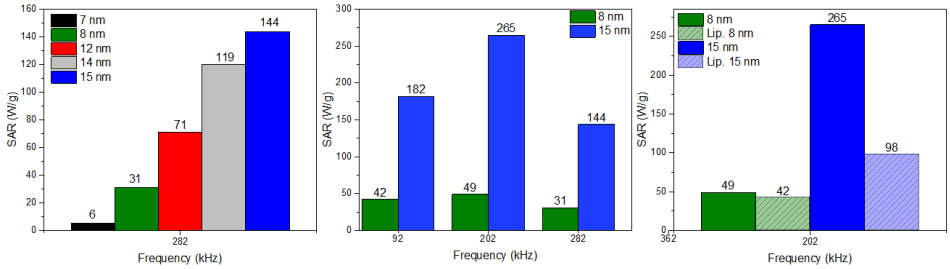

Figure 4.43: A) SAR values for NP coated by DMSA measured at 282 kHz and 21 mT, with core sizes of 7 nm (red), 8 nm (green), 12 nm (red), 14 nm (gray) and 15 nm (blue). B) SAR values for NP of 8 and 15 nm at 92, 202 and 282 kHz. C) SAR values for nanoparticles of 8 and 15 nm at 202 kHz and 30 mT and its respective magnetoliposomes. All samples were measured at concentration of 1.5 mgFe/ml.

In figure 4.43 A, five different core sizes are presented, from 7 up to 15 nm. Given the alternating magnetic field generator available in the lab, three configurations were tested; 92 kHz (65 mT = 52 kAm^{-1}), 202 kHz (30 mT = 24 kAm^{-1}) and 282 kHz (21 mT = 17 kAm^{-1}). Just one configuration is presented since the others are analogous, given the constancy of the product $H \times f$. In all cases the heating capacity is critically dependent on the core size being greater as the core size increases.

Given this result, two core sizes were chosen to follow up with the tests, 8 nm and 15 nm to evidence the difference in heat efficiency (the same core sizes already tested for cell viability). SAR values for both

nanoparticles at different field conditions can be seen also in figure 4.43 B, where the best configuration is clearly 202 kHz giving the highest SAR values for both sizes, 49 W/gFe for 8 nm nanoparticle and 265 W/gFe for 15 nm nanoparticle. Theoretical prediction of the LRT was tested for an AC excitation field of $H = 36.5\ kAm^{-1}$ and $f = 341\ kHz$, being observed that the optimum size showing maximum SAR was around 22 nm (around 500 W/gFe), for iron oxide nanoparticles [71]. The larger the core size greater its efficiency to generate heat, for a determined field condition, as already known from the literature [200] [192]. Comparing with bibliographic data iron oxide nanoparticles of small core size nanoparticles achieved SAR values around 37 W/gFe for high frequencies [201] and around 15 W/gFe for low frequencies [185], [202]. Larger nanoparticles gives SAR values around 150 W/gFe [203] up to 900 W/gFe (one of the top values reported in the literature due to coprecipitation synthesis with no coating, leading to highly aggregated system) [204]. Much larger nanoparticles around 40 nm, called magnetosomes, produced from the bacteria achieved SAR = 960 W/gFe [205], it should be noted that these bacterial magnetosomes are not superparamagnetic. Nanoparticles synthesized in this thesis present similar SAR values to the reported data in literature, when compared to alike core sizes and field configurations.

The comparison of SAR values for iron oxide nanoparticles is very complex, given that the magnetic nanoparticles have different sizes, shapes, crystallinity and also the field and frequency conditions change depending on the available equipment. The maximum SAR value is given when $\omega\tau = 1$, where $\omega = 2\pi f$ and τ is the effective relaxation time of the system (chapter 2.3.2), meaning that the increase of relaxation time does not always yield an increase in SAR. Also the frequency of the applied magnetic field must be correlated [206] [126]. The optimum core size for the maximum SAR values varies with the amplitude of the applied magnetic field (taking into account the Brezovich criterion for safety application in bio systems) [207].

Taking advantage of this knowledge on the best configuration for hyperthermia in this work, those two core size nanoparticles were encapsulated by the liposome forming the structures described in chapter 4.2. Its SAR values were compared with their respective free nanopar-

ticles (figure 4.43 C). For 8 nm NP there is a slight difference in heat efficiency after the encapsulation with the liposome, which was already expected given the AC results shown in figure 4.24, evidencing that small nanoparticles only exhibit Néel relaxation, regardless being or not physically connected to the liposome. Contrarily, for 15 nm nanoparticles SAR efficiency drops extensively, which reflects that nanoparticles have both Néel and Brownian relaxation (4.24). So when physically attached to the liposome, only the NP portion that relaxes by Néel mechanism will contribute to the heating, since it's nonviable for the whole magnetoliposome to physically rotate, given its high hydrodynamic size. A reduction of 63 % is then related to the immobilization of the nanoparticles in the liposomes. In the literature it can be found results for 15 nm core size nanoparticles where SAR values dropped by 67 % when the particle rotation was suppressed by dispersing them in a hydrogel [208]. Magnetoliposomes encapsulating 7 and 9 nm iron oxide nanoparticles show SAR values of 164 W/g and 438 W/g respectively, using 700 kHz and 27 kAm^{-1} [46].

Taking into account the results for free nanoparticles shown above, some tests were conducted with HeLa cells under an alternating magnetic field, applying the best nanoparticles, in this case 15 nm core, with the configuration of 202 kHz and 30 mT (24 kAm^{-1}), which gave the best SAR values. The results can be seen in figure 4.44, where HeLa cells were incubated at different Fe concentrations for 15 nm nanoparticles coated with DMSA, both 0.05 and 0.1 mgFe/ml. The alternate magnetic field was applied for 1 hour and compared with the control group (without the field). In the case of 0.05 mgFe/ml there is a reduction of 6 % in cells viability after the application of the field, while when the concentration is doubled (0.1 mgFe/ml) the reduction in the viability is of 11 %. In the bright field microscope images it is possible to observe some cells with a characteristic shape that might be indicative of apoptotis. Further studies will be necessary to corroborate it. Black arrows indicate such cells, in spite of no significant reduction in viability. In the literature, it can be found HeLa cells incubated with 6 nm core size iron oxide nanoparticles subjected to an AMF (80 kHz and 12 mT) for 30 min, that leads to apoptotic cell death, representing 8 % of all cell death [209]. Also for HeLa cells incubated with 10

nm iron oxide nanoparticles with AMF (20 kHz and 15 mT) for 20 min showed cell death, some of them showing disrupted membranes, indicating death by necrosis [210]. Besides, it was recently reported cell death after magnetic hyperthermia treatment without perceptible temperature rise [211], [212], [213]. This could be related to an increase in cell lysosomal permeability, caused by mechanical rotation or vibration of nanoparticles, which correlates with increased production of reactive oxygen species [178].

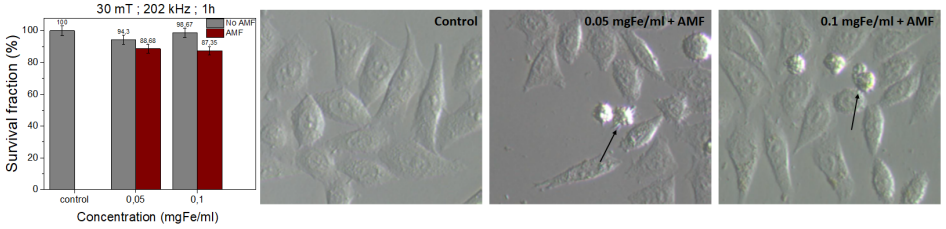

Figure 4.44: Survival measured indirectily as mitochondrial activity of HeLa cells incubated with different concentrations of 15 nm NP coated with DMSA, with and without applied field for 1h (30 mT; 202 kHz). Arrows indicate potential apoptotic cells.

4.4.4 Drug delivery control under AMF

Doxorubicin is used as a single agent in breast cancer therapy, with a recommended dose of 60 mg/m^2 (body surface area dose), administered intravenously with a 21-day treatment cycle, with a total of four cycles [130]. Its distribution half-life is of approximately 5 min and the terminal half-life is 24–48 hours. As any other chemotherapeutic agent DOX presents several adverse effects where the most serious is cardiotoxicity. To reduce the dosage and increase the circulating time liposomes were introduced as nanocarriers for the DOX, being the first formulation approved by the FDA on 1995 (Doxil®). This formulation consist on DOX-loaded liposomal bilayer with a size of 80–90 nm and coated by PEG. The dose considered safe and effective was reduced to 20 mg/m^2, also reducing the risk of cardiac events [130]. An interesting fact is that liposomes are the only type of nanocarriers that have been approved for DOX by any of the regulatory agencies, so far. Some

formulations that reached phase II/III of clinical trials have shown promising results, even when compared to conventional therapy, which led to an increase in the number of researches and papers published in this area (until 2010 there was less than 900 papers published with DOX loaded liposomes, while in 2019 this number has already doubled, according to Web of Science). In this thesis DOX was chosen given the fact that this combination with liposomes have been reported many times, assisting in the comparison of results. In this part of the chapter it will be studied the DOX release from magnetoliposomes both in water as inside cells, with and without the application of an alternate magnetic field. Nanoparticles coated by DMSA (8 nm) were chosen since they are hydrophilic and do not occupy the internal volume of the liposome, which will be totally occupied by DOX.

The DOX release from liposomes and magnetoliposomes (with NP coated by DMSA) in water was monitored by spectrophotometry, since DOX has a peak in absorbance at around 500 nm. The leakage has been measured as a function of time, dialysis, temperature and applied magnetic field (202 kHz and 30 mT). The control sample is measured as soon as the liposomes are synthesized, generating an encapsulation efficacy of more than 85 % (also obverved by [31]). Over that value, after just one hour post-synthesis 20 % more was released, which will not change even after 48 h, suggesting that the drug is in equilibrium with the medium (figure 4.45). Important note is that no difference in the DOX encapsulation efficiency was observed between liposomes with and without nanoparticles (coated by DMSA), also no difference in the release rate with time was observed. Now by doing dialysis of the liposomes and magnetoliposomes the release reaches more than 95 % in 48 h, since doxorrubicin will freely diffuse across the membrane and obtain equilibrium across the entire solution volume, in this case of about 500 ml of water each 5 ml of sample which is then changed at least 3 times a day (also observed by [214] over 24 h). The lipid bilayer is not totally rigid due to lack of cholesterol in the mixture [105]. The lack of cholesterol is intentional, since the purpose of this thesis was to incorporate magnetic nanoparticles in the bilayer and study its effect, comparing with other spatial distributions (as nanoparticles attached to the surface or inside the aqueous part). For that the bilayer must

be flexible. To conduct studies focused in drug release it is suggested to add cholesterol in a 1:1 ratio with DPPC [215].

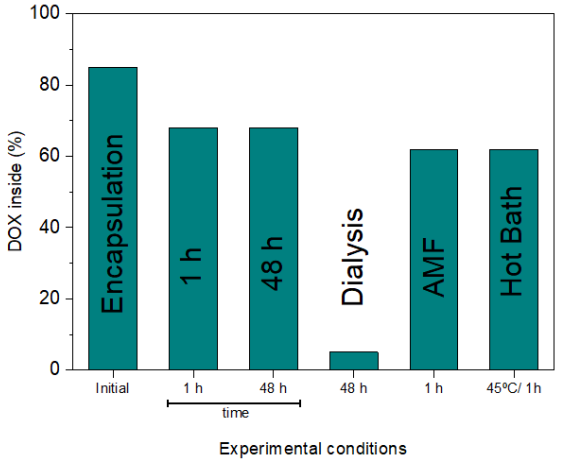

Figure 4.45: Experimental conditions for the DOX release from magnetoliposomes, with times up to 48 hours, dialysis through 48 hours, AMF applied for 1 hour and hot bath at 45 ^oC also applied for 1 hour.

Applying an alternate magnetic field to the magnetoliposomes with 202 kHz (30 mT) for 1 hour more than 27 % of doxorrubicin was released, the same result is obtained if the liposomes are maintained at 45 ^oC for 1 hour, suggesting that the leading factor is the temperature, not mattering the source, as long as it reaches the transition temperature of the bilayer (figure 4.21), also seen by [216]. No change in the results were observed after 24 h once the applied field was switched off nor after the hot bath (figure 4.45). In the literature magnetoliposomes released around 5 to 20 % of DOX passively while when applied to an AMF the release goes up to 60 %. Specifically, magnetoliposomes passively released only 5 % of DOX after 1 hour [50], while for 24 hours the DOX release reached almost 20 % [32], when maintaned at 43 ^oC for 1 hour the DOX release was of 37 % [31]. On the other hand, magnetoliposomes under AMF released more than 60 % of DOX [50] (for 1.5 hours), [32] (for 30 minutes), also DOX was massively released when magnetoliposomes were heated to 42 ^oC in a few minutes under AMF [40]. Magnetoliposomes liberated 10 nM of DOX by passive release after 1 hour, while being subjected to 30 minutes under radio frequency and waiting 1 hour released more than 45 nM of DOX

[214]. Doxorubicin is not the only cargo that can be encapsulated (as seen from chapter 1) but also magnetoliposomes loaded with calcein presented a 25 % release after AMF application for 2 hours [217].

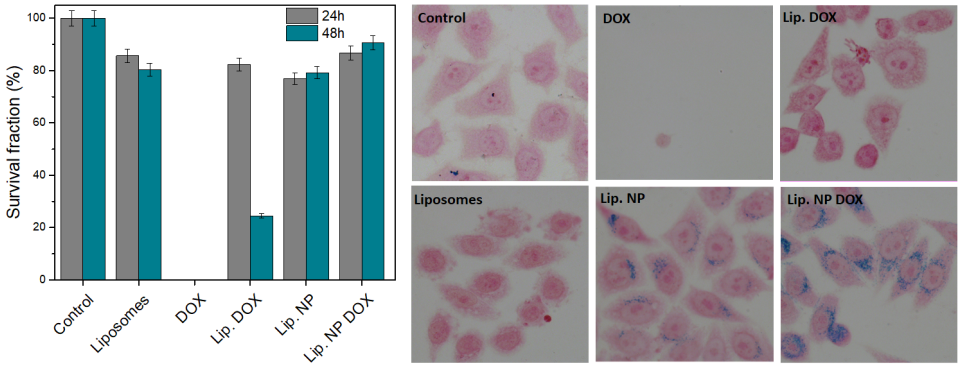

Figure 4.46: Survival evaluation by MTT assay after 24 or 48 h for HeLa cells incubated with liposomes with NP encapsulated (8 nm), liposomes with DOX encapsulated and finally liposomes with both NP and DOX encapsulated. Also liposomes and free DOX used as controls to compare. DOX used at concentration of 5 μM and NP used at 0.05 mgFe/ml. Microscope images from 24 h after incubation. Cells stained with Prussian blue reaction for iron oxide detection (right images).

Knowing the behavior of drug release from liposomes in water the research was passed forward to the release in cell cultures. The first cell culture chosen was HeLa cells given that previous viability studies were conducted to evaluate the optimal core size and iron concentrations needed to perform the experiments. The tests started with the smallest nanoparticles (8 nm), 5 μM of DOX and 0.05 mgFe/ml of NP. For these quantities an interesting result appears as the slow liberation of DOX from the liposome, requiring a longer incubation time (more than 48 hours) to observe cell death when compared to free DOX (also seen by [216]). The survival of HeLa cells incubated with encapsulated DOX goes from 80 % (in 24 h) to less than 20 % over 48 h (figure 4.46). HeLa cells incubated with liposomes loaded with NP and DOX have good cell survival (over 80 %) and NP are internalized as seen in the microscopy (blue dots). Nanoparticles were able to enter and accumulate in the cytoplasm since they are attached on the liposome surface while the DOX needs more time (more than 48 h) to diffuse through the lipid bilayer to the cell cytoplasm.

Based on previous tests it was observed that the quantity of free DOX was excessive, killing all the cells, not allowing the real evaluation of toxicity with time. Therefore, the concentration was reduced to 1 μM for future tests. It was also observed that more time was needed to evaluate the liberation of DOX from the liposome and its respective effect (more than 48 hours). Also as the final ambition in this work is the feasibility of the drug release from the magnetoliposome with magnetic hyperthermia, larger NP (15 nm) were used to follow up the tests given the results from SAR shown previously (figure 4.43).

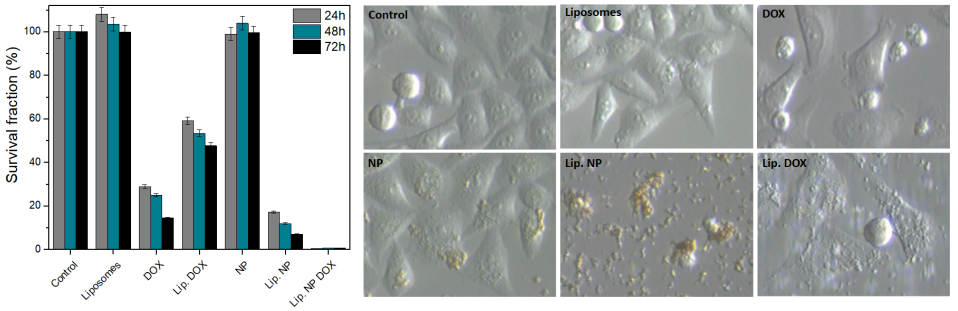

Figure 4.47: Tocicity on HeLa cells treated with 15 nm NP for 24, 48 and 72 h, evaluated by MTT assay. Cells incubated with liposomes, free DOX, NP, liposomes with encapsulated NP, liposomes with encapsulated DOX and finally liposomes with both NP and DOX encapsulated. DOX used at concentration of 1 μM and NP used at 0.05 mgFe/ml. Bright field microscope images from 24 h after incubation (right).

By reducing the DOX concentration to 1 μM a better evaluation of the effect on HeLa cells was possible, the drug has prolonged effect with time, decreasing the survival fraction up to 10 % in 72 hours (figure 4.47). DOX encapsulated in liposomes also showed an increased viability when compared to free drug and also a low release rate. The cell survival when incubated with samples Lip.NP was exceptionally lower than 20% due to a new attempt to sterilize the samples with UV light, which induced free radical formation, causing high toxicity [218], being a discarded method. In the literature HeLa cells were incubated with DOX loaded 14 nm iron oxide nanoparticles, where DOX was observed in the cytoplasm and nucleus treated cells after 2 and 8 hours of incubation respectively, while for the free DOX entered the cell nucleus after only 2 hours of incubation [216].

Once the parameters such as doses, times and alternating field conditions have been optimized for Hela cells (a reference line for viability tests *in vitro* [219] [181] [182] [183]), the study was expanded to other cell line like MDA-MB-231, widely used for nanoparticle viability tests. In this case the study was focused on the evaluation of the synergistic effect of the DOX and the alternating magnetic field using as nanovectors the magnetoliposomes developed in this thesis.

MDA-MB-231 cell cultures were exposed for 24 hours to either nanoparticles, magnetoliposomes, DOX or a combination of these three treatments, with constant iron concentration of 0.1 mgFe/ml and 0.4 μM of DOX (the dosage was reduced in correspondence to the DOX sensitivity of this new cell line). The excess nanoparticles / liposomes were removed after these 24 hours, so only the ones internalized or attached to the cell surface were retained and can be seen in microscope images below. For more details in the preparation and quantities go to chapter 3. Viability of these cells was conducted by staining with calcein and EthD-1 to perform a Live/Dead test (chapter 3). Figure 4.48 shows the control image of MDA-MB-231 cells, were live cells appear in green and dead cells appear in red, showing also the transmittance image to observe cell morphology. These control cells have a density of 142627 $cells/cm^2$ (Table 4.6). As the cell viability is calculated by the ratio between $[live/(live+dead)$ * 100] in control cells gives more than 90 %, since these cells are subjected to culture media replacement that remove floating dead cells (given that is an adherent cell line) and are washed away. Density values are displayed in table 4.6 to easy access.

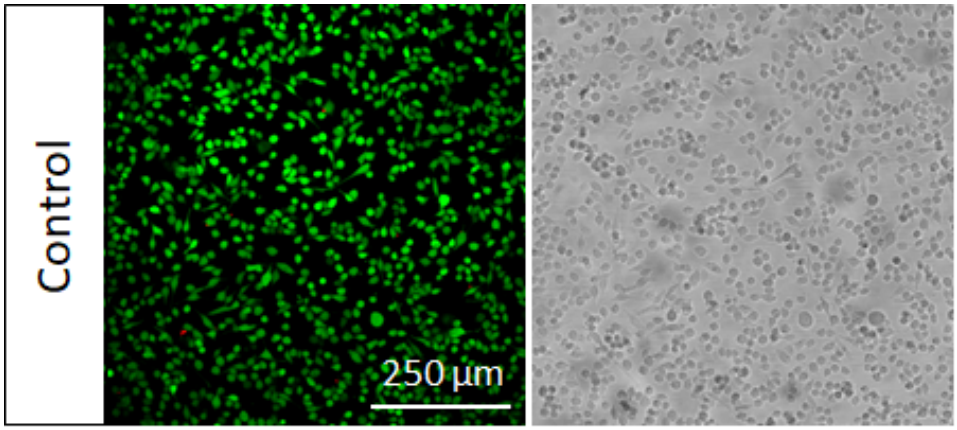

Figure 4.48: Viability studies by confocal laser scanning microscopy of MDA-MB-231 cells as control, without any treatment. A bright field image is shown to better appreciate cell morphology (right). Live cells appear in green while dead cells appear in red (left image).

MDA-MB-231 cells were exposed to nanoparticles (15 nm coated by DMSA), liposomes, magnetoliposomes, free DOX, DOX encapsulated in liposomes and the finally the combination of magnetoliposomes with DOX. Viability studies can be seen in figure 4.49, reminding that the green cells are alive and the red ones are dead. The treatment with magnetic nanoparticles of 15 nm gives a normalized survival ($TreatedCellDensity/ControlCellDensity$ $\times 100$) of 73 %. When the treatment is performed with liposomes a normalized survival of 63 % is obtained. Given that there are two main parameters fixed in the experiment (iron and DOX concentration) it is quite hard to maintain unchanged the third one, lipids concentration. It was already discussed at the beginning of this section that liposomes present some toxicity depending on the quantity and on the degradation due to time. Comparing with free DOX, there is a huge drop of survival, representing a 3 % normalized survival. For the magnetoliposomes there is an increased survival with respect to free nanoparticles, representing 80 % of normalized survival. Also comparing the DOX encapsulated in liposomes there is a huge increase with a 51 % normalized survival. Combining magnetoliposomes with DOX gives rise a normalized survival of 40 %. Bibliographic data support the decrease in cell number compared to control when MDA-MB-231 cells are treated with free DOX [204].

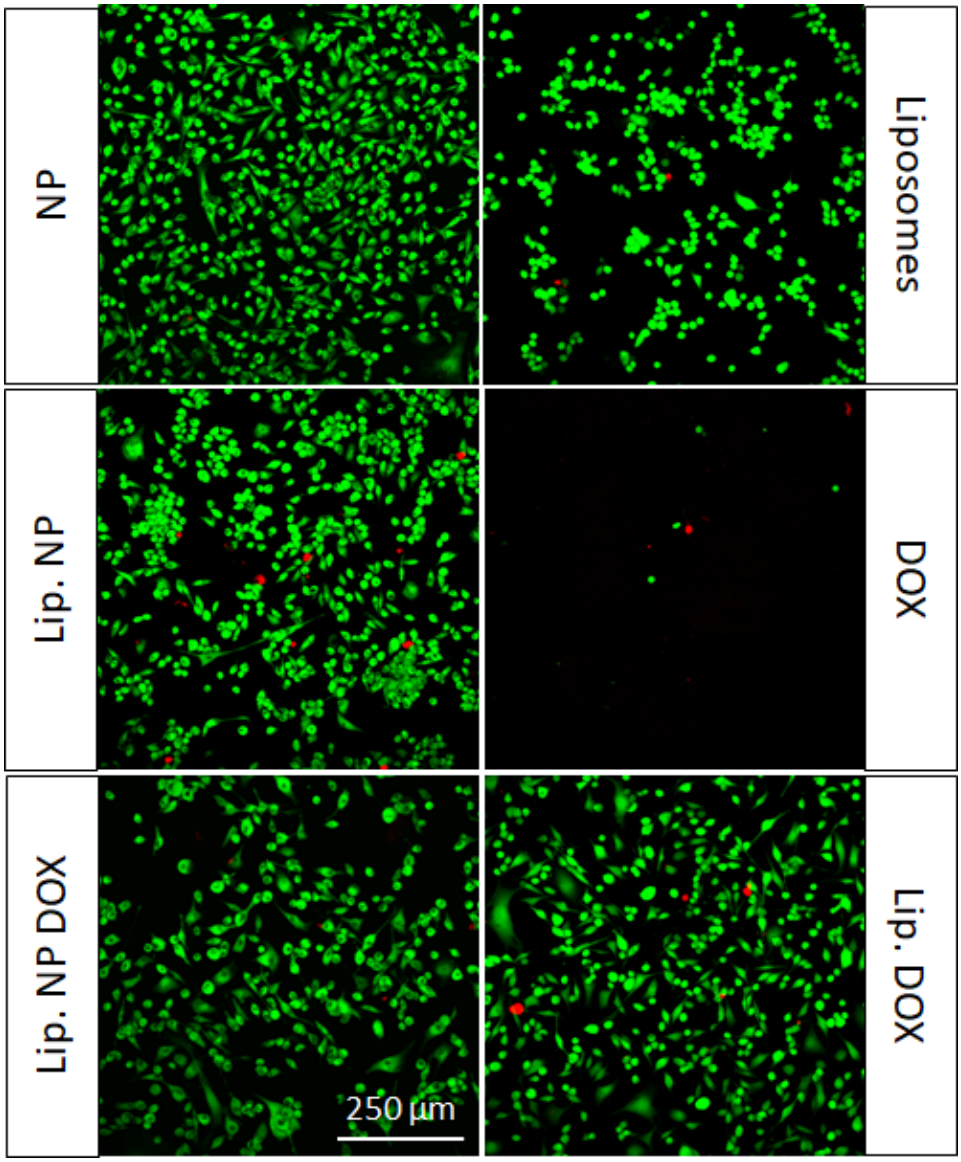

Figure 4.49: Viability studies by confocal laser scanning microscopy of MDA-MB-231 cells after exposure to different treatments as nanoparticles, liposomes, magnetoliposomes, DOX, liposomes with DOX encapsulated and also magnetoliposomes with DOX. Concentrations of 0.1 mgFe/ml and 0.4 μM DOX were kept constant. Live cells appear in green while dead cells appear in red. Scale bars represent 250 μm in all images.

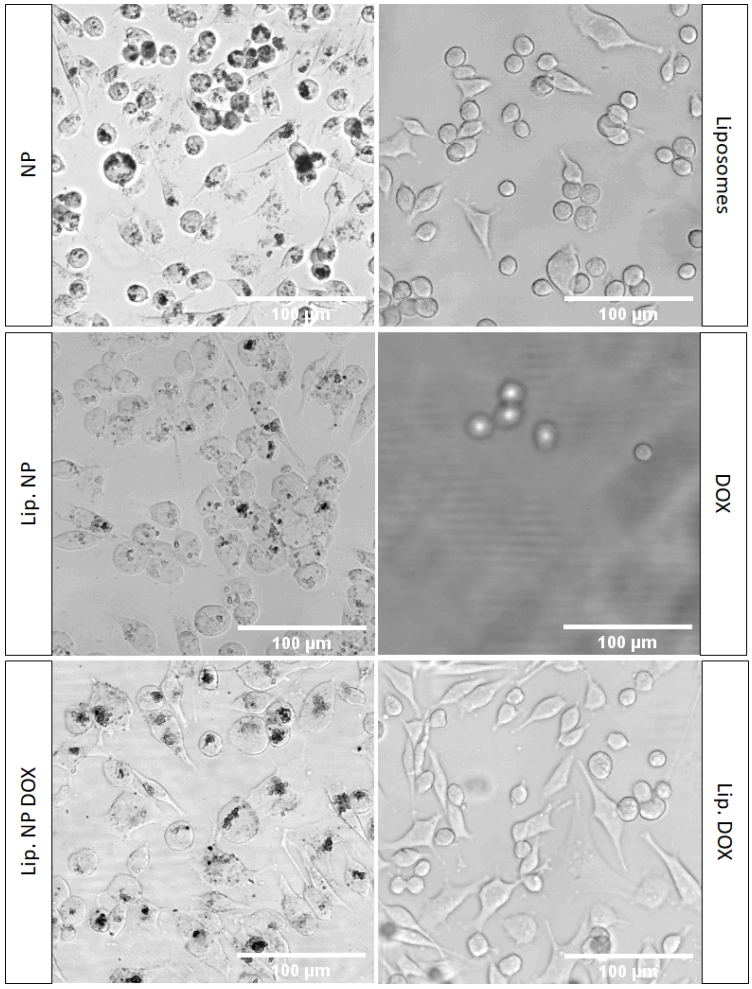

Figure 4.50: Representative bright field microscopy images of MDA-MB-231 cells cultures after 24 hours of exposure to different treatments, as nanoparticles, liposomes, magnetoliposomes, DOX, liposomes with DOX encapsulated and magnetoliposomes with DOX. Concentrations of 0.1 mgFe/ml and 0.4 μM DOX were kept constant. Evident intracellular uptake of nanoparticles was observed.

Figure 4.50 is composed of representative transmission microscopy images of the MDA-MB-231 cells with the treatments, where is easily spotted the internalization of nanoparticles in the images from the left, seen as black dots inside the cell membrane. Previous works on MDA-MB-231 cells incubated with 12 nm nanoparticles coated by DMSA for 24 hours also showed a substantial fraction of internalized nanoparticles accumulated in the lysosomal compartment of cells [204]. SH-SY5Y

cells incubated with magnetoliposomes (5 nm NP) and DOX presented a survival of around 70 % over 24 hours incubation time, when treated with free DOX the cell viability was less than 60 % over the same period of time, showing a delay effect of DOX encapsulated in liposomes [32].

The next step is to apply an alternate magnetic field (AMF) to the cells with magnetic nanoparticles to check if the principal hypothesis of this thesis is correct and there is an the effect in cell behavior (morphology and viability).

MDA-MB-231 cells as control were placed in a coil, with the configuration of 202 kHz and 30 mT (24 kAm^{-1}) (configuration that gave the best SAR values for 15 nm core nanoparticles) to observe if the magnetic field causes some effect both in viability as in morphology, giving a density of 261050 $cells/cm^2$ which will be used to normalize the survival for the other treatments (figure 4.51).

When cells are treated with nanoparticles and AMF for 1 hour the normalized survival is of 56 %. Treating cells with magnetoliposomes gives rise to a really similar effect caused by free nanoparticles, representing also 56 % normalized survival. Combining all the treatments, meaning, magnetoliposomes with DOX and AMF reduces the normalized survival to 3 %. Density values can be found in table 4.6. Bibliographic data supports the decrease in cell density, MDA-MB-231 cells treated with 12 nm nanoparticles in combination with DOX and magnetic hypertermia (H = 15.4 kAm^{-1} = 19 mT, f = 435 kHz) triggered the treatment, reducing in more than 75 % the cell viability when compared to the treatment without AMF, also showing that free DOX was equally cytotoxic with and without hyperthermia to MDA-MB-231 breast cancer cells (less than 5 % viability), besides for concentrations up to 0.1 mgFe/ml the free NP did not trigger cytotoxicity [204]. Also MDA-MB-231 cells incubated with 12 nm NP under AMF (H = 6 kAm^{-1} = 7.5 mT and f = 386 kHz) induced cell death, where the efficacy of cell death increased with extending duration of AMF exposure. Specifically, for 5 minutes of exposure there was around 40 % cell death while for 30 minutes was more than 90 % of cell death. Alternatively, conventional hyperthermia (water bath at 46 ^oC) for 30 min killed less than 10 % of cells [220].

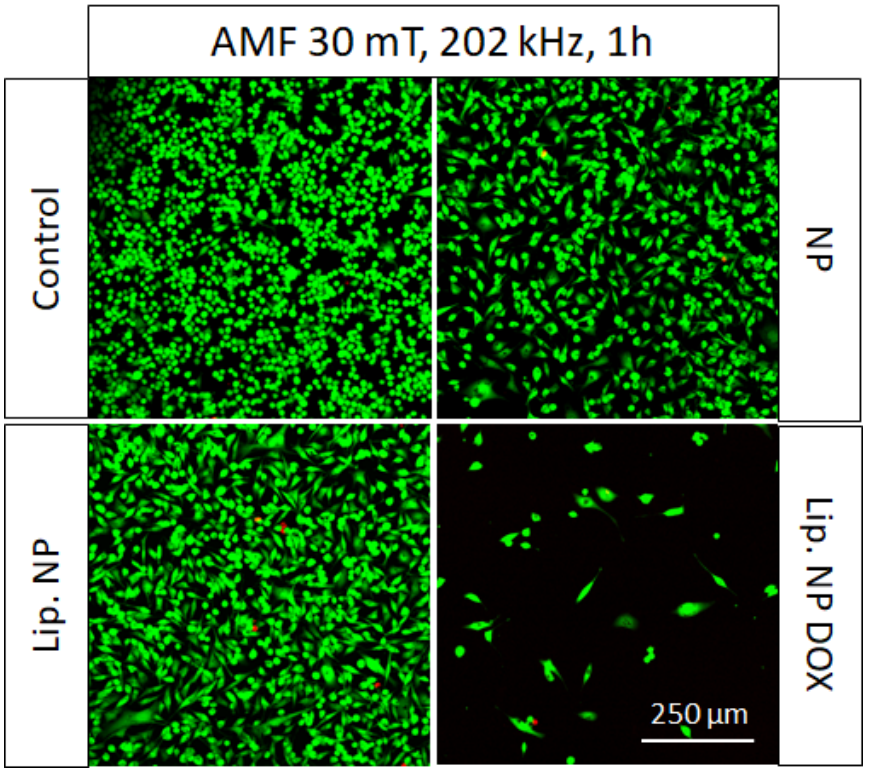

Figure 4.51: Viability studies by confocal laser scanning microscopy of MDA-MB-231 cells cultures with different treatments after exposure to the applied magnetic field of 30 mT and 202 kHz for 1 hour. Concentrations of 0.1 mgFe/ml and 0.4 μM DOX were kept constant. Live cells appear in green while dead cells appear in red. Scale bars represent 250 μm in all images.

Observing the bright field microscopy images (figure 4.52) it can be clearly spotted the internalization of nanoparticles (except in control sample) as black dots inside the cells. In the literature magnetoliposomes (10 nm NP) with DOX were tested with HeLa and KB cells where magnetic hyperthermia (290 kHz and 15 mT) synergistically increased the cytotoxicity, reducing from 70 % to 35 % the cell viability after aplication of AMF [31]. Huh-7 (hepatocellular carcinoma cell line) incubated with magnetoliposomes (5 nm NP) and DOX (2 μM) for 24 hours presented a reduction of 24 % in viability while when placed under radio frequency (170 kHz) for 30 minutes reduced the cell viability up to 40 % after 8h and significant cell death ($>$ 90 %) was observed after 24 h [214].

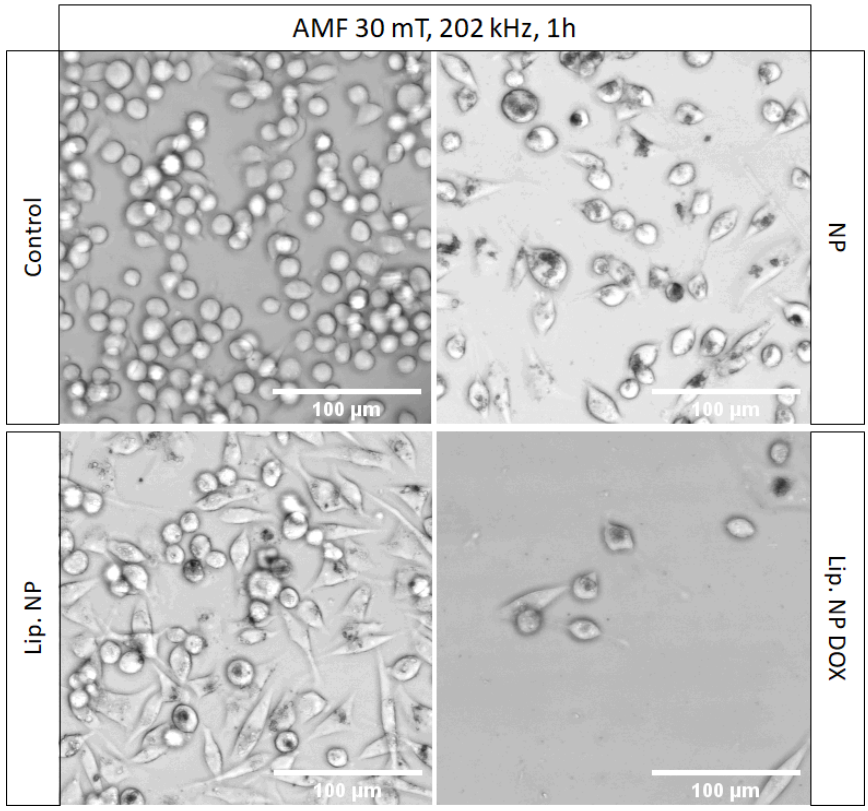

Figure 4.52: Representative microscopy images illustrating intracellular uptake of nanoparticles and magnetoliposomes, also magnetoliposomes with DOX encapsulated, by MDA-MB-231 cells after exposure to the applied magnetic field of 30 mT and 202 kHz for 1 hour. Concentrations of 0.1 mgFe/ml and 0.4 μM DOX were kept constant. Evident intracellular uptake of nanoparticles was observed.

Table 4.6: Values for cell viability, density and normalized survival of MDA-MB-231 cells exposed to different treatments for 24 hours, and the application of an applied alternate magnetic field for 1 hour.

Samples	**no AMF**			**with AMF**		
	Viability (%)	Density ($cells/cm^2$)	Normalized Survival (%)	Viability (%)	Density ($cells/cm^2$)	Normalized Survival (%)
Control	97	142627	100	99	261050	100
Liposomes	95	89730	63	-	-	-
DOX	55	4874	3	-	-	-
Lip. DOX	99	72892	51	-	-	-
NP	97	104630	73	99	145978	56
Lip. NP	98	114656	80	99	145397	56
Lip. NP DOX	98	56829	40	93	7893	3

Finally, the last parameter that should draw attention and that rarely was taken into account is the magnetic field itself. Placing an individual plate inside a coil gives rise to a completely different behavior across the cell culture media due to inhomogeneities in field intensity. Hyperthermia equipments are composed of finite solenoid presenting a non uniform field. Cells are very sensitive to even small changes, displaying different survival depending on the location in the plate. Cell survival diminishes in the areas close to the center of the field and increases close to the borders. Cells exposed to magnetoliposomes with DOX, for example, increase density from 7893 $cells/cm^2$ in the center to 90893 $cells/cm^2$ in the borders, representing a change from 3% to 35% in normalized survival. The magnetic field homogeneity is an important parameter to take into account for future applications *in vivo*.

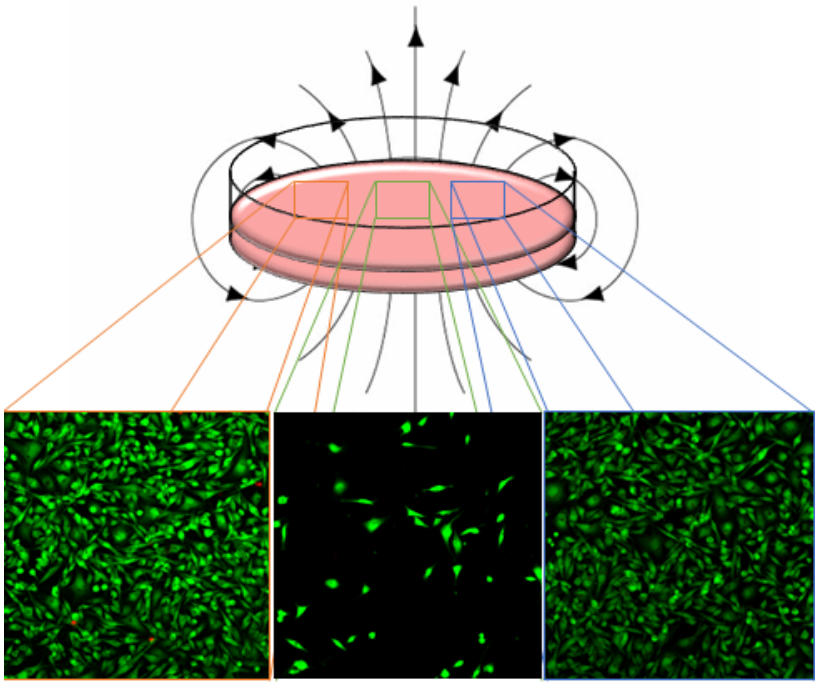

Figure 4.53: Viability of MDA-MB-231 cells after exposure to magnetoliposomes with DOX and AMF for 1 hour, depending on the location in the individual plate, decreasing towards the center of the magnetic field and increasing towards the borders of the plate. Live cells appear as green while dead cells appear as red.

Figure 4.54 summarizes the normalized survival of MDA-MB-231 cells after different treatments and after applying an alternate magnetic field. An important point is a drop in survival of around 20 % when cells are treated with either nanoparticles or magnetoliposomes after the exposure to the AMF. Also cell survival of magnetoliposomes with DOX after exposure to an AMF is the same as the free DOX, resulting in only 3%. Liposomes with NP protect cells from DOX toxicity without the AMF, this result corresponds to a control of the drug release by applying a noninvasive external magnetic field. The proposed formulation composed of iron oxide nanoparticles, liposomes and DOX have high potential for translation to clinical practice, since the isolated components have been previously approved by the FDA, needing some effort to control the synergistic effects of the whole formulation and also to modify the liposomes surface so that they are colloidally stable for longer times.

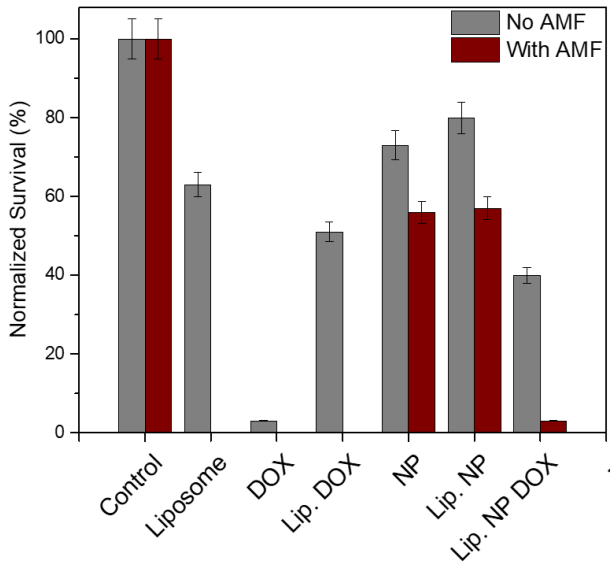

Figure 4.54: Normalized survival of MDA-MB-231 cells after 24h of exposure to different treatments (gray bars), as liposomes, free DOX, DOX encapsulated in liposomes, magnetic nanoparticles (15 nm), magnetoliposomes and magnetoliposomes with DOX. Concentrations of 0.1 mgFe/ml and 0.4 μM DOX were kept constant. Effect of the normalized survival of MDA-MB-231 cells after application of an alternate magnetic field with 202 kHz and 30 mT for 1 hour (red bars).

4.4.5 Partial conclusions

Magnetic nanoparticles prepared by microwave and thermal decomposition, transferred to water by ligand exchange with DMSA showed low toxicity for HeLa cells at 0.05 mgFe/ml and 24 hours after incubation. Cell survival is above 95 %, presenting nanoparticles internalization in the cytoplasm confirmed by Prussian Blue stain. Liposomes are not toxic within the first 10 days of synthesis up to 0.2 mgDPPC/ml. After this time the lipid degradation starts to show signs of toxicity. Magnetoliposomes loaded with DMSA coated nanoparticles increase the intracellular absorption when compared to free nanoparticles, accumulating in the cytoplasm with 100 % efficiency, without an alteration in cell viability.

Iron oxide nanoparticles and magnetoliposomes present high values of r_2 relaxivity indicating a potential as negative (T_2) contrast agents for MRI. Nanoparticles with 8 nm core size were tested *in-vivo*, both free or encapsulated in liposomes, showing an accumulation in the murine's liver after only 5 minutes post-injection, exhibiting a characteristic darkening in MRI images.

Hyperthermia treatment combining magnetoliposomes and DOX was first set up for HeLa cells adjusting the conditions to get some effect in the cell viability. When combining magnetoliposomes with DOX in HeLa cells interesting results arised, as the slow liberation of DOX from the liposomes, requiring longer observation times (more than 48 hours), since DOX need more time to diffuse through the liposome bilayer. Nanoparticles are able to enter in the cytoplasm given its spatial distribution (attached to the liposome surface) maintaining a good cell viability.

Drug release control using the alternating magnetic field was adjusted for MDA-MB-231 cells. Applying an AMF for 1 hour triggered the drug release from the magnetoliposome reaching the same cell death rate as free DOX (3 % survival), suggesting a controlled release by applying a noninvasive external magnetic field. This result may lead to a reduction in the dosage required to achieve the same efficiency, also reducing DOX side effects.

Chapter 5

Conclusions

Microwave assisted synthesis of magnetic iron oxide nanoparticles have been studied, determining the key parameters that control nucleation and growth processes, and therefore, particle size and uniformity. In comparison to conventional heating where nanocrystals tend to nucleate on the vessel walls first given its inhomogeneous heating profile, microwave produces efficient internal heating promoting nucleation everywhere and reducing the growth possibilities of the numerous nuclei generated. The optimal heating ramp was set at 3.75 $^oC/min$, the best iron concentration was set as 4 mgFe/ml, and best (oleic/Fe) molar ratio was set as 5 giving rise to the most uniform nanoparticles, which is limited to a maximum of 8 nm.

Magnetic nanoparticles have been incorporated to liposomes leading to magnetoliposomes, that presents different spatial distribution of the nanoparticles depending on the nanoparticle coating. Nanoparticles can be attached to the liposome surface (DMSA), inside the lipid bilayer (Oleic acid) or encapsulated in its aqueous volume (APS). Colloidal properties of the magnetoliposomes depends on the surface charge of nanoparticles and liposomes, and the lipid bilayer melt transition is shifted to lower temperatures by the nanoparticles incorporation (from 41.6 ^oC up to 38 ^oC).

Aggregation processes of magnetic nanoparticles have been ana-

lyzed in three systems with different spatial distribution, i.e. free iron oxide nanoparticles positively (APS) and negatively (DMSA) coated, magnetoliposomes with nanoparticles on the surface and inside the aqueous core, and cells with nanoparticles attached at the membrane or uptaken. By DC measurements the blocking temperature of the cells incubated with nanoparticles, regardless of the location in which they are, the incubation time, the cell line or the nanoparticle coating, is greater than the blocking temperature of the free nanoparticles and the magnetoliposomes, indicating that the simple fact of being in contact with the cells makes the nanoparticles aggregate in a non-controlled way. AC susceptometry measurements demonstrate that the biological environment significantly influences also the dynamic magnetic response of the nanoparticles, which may explain the heating inefficiency of nanoparticles when in contact with cells.

Two nanoparticles core sizes (8 and 15 nm) were tested to evidence the difference in heat efficiency for hyperthermia treatments, where the best configuration is with 202 kHz + 30 mT giving the highest SAR values for both sizes, 49 W/gFe for 8 nm NP and 265 W/gFe for 15 nm NP. After encapsulation in the liposomes there is a there is reduction in heat efficiency mainly for larger particles going down to around 100 W/gFe, due to their inmobilization.

Cell viability tests of the nanoparticles were performed first with HeLa cells to evaluate the ideal Fe concentration and incubation times which allowed a cell survival above 90 %, resulting in 0.05 mgFe/ml for 24 and 48 hours. Liposomes were not considered toxic up to 0.2 mgDPPC/ml, yet presenting toxicity after 10 days of synthesis due to phospholipid degradation with time. Finally free doxorubicin was tested with a concentration of 1 μM which allowed the toxicity evaluation with times up to 72 hours. Magnetoliposomes increased the nanoparticle intracellular uptake when compared to free nanoparticles, accumulating in the cytoplasm with 100 % efficiency, without an alteration in cell viability.

A great negative (T_2) contrast for MRI was achieved for magnetic nanoparticles coated by DMSA. A slight enhance signal was observed for the magnetoliposomes in comparison with the free nanoparticles.

In-vivo tests with 8 nm core sizes nanoparticles showed an accumulation in the murine's liver after only 5 minutes post-injection.

Magnetic hyperthermia treatment combining magnetoliposomes and DOX was first set up for HeLa cells adjusting the conditions to get some effect in the cell viability. DOX need more time to diffuse passively through the liposome bilayer, requiring longer observation times (more than 48 hours) to see a decrease in cell viability. MDA-MB-231 cells incubated with 15 nm nanoparticles and magnetoliposomes reduced in 20 % its survival after exposure to an alternating magnetic field for 1 hour. Drug release control using AMF for 1 hour was adjusted for MDA-MB-231 cells incubated with magnetoliposomes and DOX, presenting the same survival as free DOX (only 3 % survival), suggesting a controlled drug release by a noninvasive external magnetic field.

Chapter 6

Conclusiones

Se ha estudiado la síntesis de nanopartículas magnéticas de óxido de hierro por microondas, y se ha determinando el papel de parámetros clave en los procesos de nucleación y crecimiento, que determinan el tamaño y la uniformidad de las partículas. En comparación con el calentamiento convencional, donde las nanoparticulas tienden a nuclear en las paredes del recipiente, el microondas produce un calentamiento interno homogéneo y eficaz que promueve la nucleación en todas partes y reduce las posibilidades de crecimiento de los numerosos núcleos generados. La rampa de calentamiento óptima se estableció en 3.75 $^oC/min$, la mejor concentración de hierro se estableció en 4 mgFe/ml, y la mejor relación molar (oleico/Fe) se estableció en 5 dando lugar a nanopartículas uniformes, con un tamaño máximo de 8 nm.

Las nanopartículas magnéticas se han incorporado a los liposomas, formando magnetoliposomas, que presentan una distribución espacial diferente de las nanopartículas en función de su recubrimiento. Las nanopartículas se pueden unir a la superficie del liposoma (DMSA), dentro de la bicapa lipídica (ácido oleico) o encapsularse en su volumen acuoso (APS). Las propiedades coloidales de los magnetoliposomas dependen de la carga superficial de las nanopartículas y de los liposomas, y además, la temperatura de fusión de la bicapa lipídica se desplaza a temperaturas más bajas mediante la incorporación de las nanopartículas (desde 41.6 ^oC hasta 38 ^oC).

Los procesos de agregación de nanopartículas magnéticas se han analizado en tres sistemas con diferente distribución espacial, es decir, nanopartículas de óxido de hierro libre recubiertas positivamente (APS) y negativamente (DMSA), magnetoliposomas con nanopartículas en la superficie y en el interior del volumen acuoso, y células con nanopartículas unidas en la membrana o dentro del citoplasma. Las medidas DC muestran que la temperatura de bloqueo de las células incubadas con nanopartículas, independientemente de la ubicación en la que se encuentren, el tiempo de incubación, la línea celular o el recubrimiento de nanopartículas, es mayor que la temperatura de bloqueo de las nanopartículas libres y los magnetoliposomas, lo que indica que el simple hecho de estar en contacto con las células hace que las nanopartículas se agreguen de forma no controlada. Las medidas de susceptometría AC confirman que el entorno biológico influye significativamente también en la respuesta magnética dinámica de las nanopartículas, lo que puede explicar la ineficiencia de calentamiento de las nanopartículas cuando están en contacto con las células.

Se probaron dos tamaños de núcleo de nanopartículas (8 y 15 nm) para evidenciar la diferencia en la eficiencia del calor para los tratamientos de hipertermia, donde la mejor configuración del campo es 202 kHz + 30 mT que proporcionan los valores más altos de SAR para ambos tamaños de nanoparticulas, 49 W/gFe para 8 nm NP y 265 W/gFe para 15 nm. Después de la encapsulación en los liposomas, hay una reducción en la eficiencia del calor principalmente para partículas más grandes que disminuye hasta alrededor de 100 W/gFe, debido a su inmovilización.

Las pruebas de viabilidad celular de las nanopartículas se realizaron primero con células HeLa para determinar la concentración ideal de Fe y los tiempos de incubación que permitieron una supervivencia celular superior a 90 %, dando como resultado 0,05 mgFe/ml durante 24 y 48 horas. Los liposomas no mostraron toxicidad hasta 0.2 mgDPPC/ml, pero presentaron una toxicidad después de 10 días de síntesis debido a la degradación de fosfolípidos con el tiempo. Finalmente, se ajustó la concentración de doxorubicina libre a um máximo de 1 μM, lo que permitió la evaluación de la toxicidad con tiempos de hasta 72 horas. Los magnetoliposomas aumentaron la internalización celular de

las nanopartículas en comparación con las nanopartículas libres, acumulándose en el citoplasma con una eficacia del 100 %, sin alteración en la viabilidad celular.

Se logró un gran contraste negativo (T_2) en MRI para nanopartículas magnéticas recubiertas con DMSA. Se observó un aumento moderado de la señal para los magnetoliposomas en comparación con las nanopartículas libres. Las pruebas *in-vivo* con nanopartículas de tamaño de núcleo de 8 nm mostraron una acumulación en el hígado del ratón después de sólo 5 minutos de la inyección.

El tratamiento de hipertermia magnética que combina magnetoliposomas y DOX se estudió primero con las células HeLa, ajustando las condiciones para obtener algún efecto en la viabilidad celular. La DOX necesita más tiempo para difundirse pasivamente a través de la bicapa del liposoma, lo que requiere tiempos de observación más prolongados (más de 48 horas) para ver una disminución en la viabilidad celular. Las células MDA-MB-231 incubadas con nanopartículas de 15 nm y magnetoliposomas redujeron en 20 % su supervivencia después de la exposición a un campo magnético alterno durante 1 hora. Cuándo se aplicó el AMF durante 1 hora, las células MDA-MB-231 incubadas con magnetoliposomas y DOX, presentaron la misma supervivencia que cuándo se utiliza la DOX libre (sólo 3 % de viabilidad). Esto sugiere que se ha conseguido una liberación controlada del fármaco por un campo magnético externo no invasivo.

Appendix A

List of Publications

• Maria Eugenia Fortes Brollo, Sabino Veintemillas-Verdaguer, Cesar Menor Salván, and Maria del Puerto Morales, "Key Parameters on the Microwave Assisted Synthesis of Magnetic Nanoparticles for MRI Contrast Agents", Contrast Media and Molecular Imaging, Article ID 8902424, 13 pages, 2017.

• Helena Gavilán, Elena H. Sánchez, Maria Eugenia Fortes Brollo, Laura Asín, Kimmie K. Moerner, Cathrine Frandsen, Francisco J. Lázaro, Carlos J. Serna, Sabino Veintemillas-Verdaguer, M. Puerto Morales, and Lucía Gutiérrez, "Formation Mechanism of Maghemite Nanoflowers Synthesized by a Polyol-Mediated Process", ACS Omega, 2, 7172-7184, 2017.

• Maria Eugenia Fortes Brollo, Patricia Hernandez Flores, Lucia Gutierrez, Christer Johansson, Domingo Francisco Barber and Maria del Puerto Morales, "Magnetic properties of nanoparticles as a function of their spatial distribution on liposomes and cells", Phys. Chem. Chem. Phys.,20, 17829-17838, 2018.

• Helena Gavilán, Maria Eugenia Fortes Brollo, Lucía Gutiérrez, Sabino Veintemillas-Verdaguer and María del Puerto Morales, "Controlling the size and shape of uniform magnetic iron oxide nanoparticles for biomedical applications", Chapter 1 of book "Clinical Applications

of Magnetic Nanoparticles", ISBN 9781138051553, CRC Press, 3-23, 2018.

• Alejandro G.Roca, Lucía Gutiérrez, Helena Gavilán, Maria Eugênia Fortes Brollo, Sabino Veintemillas-Verdaguer and María del Puerto Morales, "Design Strategies for Shape-Controlled Magnetic Iron Oxide Nanoparticles", Advanced Drug Delivery Reviews, 2019, In Press.

• Raquel Mejías, Patricia Hernández Flores, Marina Talelli, José L. Tajada-Herráiz, Maria Eugenia Fortes Brollo, Yadileiny Portilla, María del Puerto Morales and Domingo F. Barber, "Cell-promoted nanoparticle aggregation decreases nanoparticle-induced hyperthermia under an alternating magnetic field independently of nanoparticle coating, core size and subcellular localization", ACS Applied Materials and Interfaces, 11(1), 340-355, 2019.

Bibliography

[1] B. D. Cullity and C. D. Graham, "Introduction to magnetic materials," *John Wiley and Sons, Inc.*, 2009.

[2] C. R. Kagan, L. E. Fernandez, Y. Gogotsi, P. T. Hammond, M. C. Hersam, A. E. Nel, R. M. Penner, C. G. Willson, and P. S. Weiss, "Nano day: Celebrating the next decade of nanoscience and nanotechnology," *ACS Nano*, vol. 10, no. 10, pp. 9093–9103, 2016.

[3] T. K. Jain, M. K. Reddy, M. A. Morales, D. L. Leslie-Pelecky, and V. Labhasetwar, "Biodistribution, clearance, and biocompatibility of iron oxide magnetic nanoparticles in rats," *Molecular Pharmaceutics*, vol. 5, no. 2, pp. 316–327, 2008.

[4] J. Estelrich, M. J. Sánchez-Martín, and M. A. Busquets, "Nanoparticles in magnetic resonance imaging: from simple to dual contrast agents," *International journal of nanomedicine*, vol. 10, p. 1727, 2015.

[5] C. R. UK, "Worldwide cancer statistics," 2018.

[6] M. R. Preiss and G. D. Bothun, "Stimuli-responsive liposome-nanoparticle assemblies," *Expert Opinion on Drug Delivery*, vol. 8, no. 8, pp. 1025–1040, 2011.

[7] J. I. Hare, T. Lammers, M. B. Ashford, S. Puri, G. Storm, and S. T. Barry, "Challenges and strategies in anti-cancer

nanomedicine development: An industry perspective," *Advanced Drug Delivery Reviews*, vol. 108, pp. 25–38, 2017. Editor's Collection 2016.

[8] Q. A. Pankhurst, J. Connolly, S. K. Jones, and J. Dobson, "Applications of magnetic nanoparticles in biomedicine," *Journal of Physics D: Applied Physics*, vol. 36, no. 13, p. R167, 2003.

[9] Q. A. Pankhurst, N. T. K. Thanh, S. K. Jones, and J. Dobson, "Progress in applications of magnetic nanoparticles in biomedicine," *Journal of Physics D: Applied Physics*, vol. 42, no. 22, p. 224001, 2009.

[10] L. Zhang, W.-F. Dong, and H.-B. Sun, "Multifunctional superparamagnetic iron oxide nanoparticles: design, synthesis and biomedical photonic applications," *Nanoscale*, vol. 5, pp. 7664–7684, 2013.

[11] A. Gupta, R. S. Kane, and D.-A. Borca-Tasciuc, "Local temperature measurement in the vicinity of electromagnetically heated magnetite and gold nanoparticles," *Journal of Applied Physics*, vol. 108, no. 6, p. 064901, 2010.

[12] J. Kudr, Y. Haddad, L. Richtera, Z. Heger, M. Cernak, V. Adam, and O. Zitka, "Magnetic nanoparticles: From design and synthesis to real world applications," *Nanomaterials*, vol. 7, no. 9, 2017.

[13] D. Mertz, O. Sandre, and S. Bégin-Colin, "Drug releasing nanoplatforms activated by alternating magnetic fields," *Biochimica et Biophysica Acta (BBA) - General Subjects*, vol. 1861, no. 6, pp. 1617–1641, 2017. Recent Advances in Bionanomaterials.

[14] R. A. Revia and M. Zhang, "Magnetite nanoparticles for cancer diagnosis, treatment, and treatment monitoring: recent advances," *Materials Today*, vol. 19, no. 3, pp. 157–168, 2016.

[15] Y. X. J. Wáng, J.-M. Idée, and C. Corot, "Scientific and industrial challenges of developing nanoparticle-based theranostics and multiple-modality contrast agents for clinical application," *Nanoscale*, vol. 7, pp. 16146–16150, 2015.

[16] A. Ali, H. Zafar, M. Zia, I. ul Haq, A. R. Phull, J. S. Ali, and A. Hussain, "Synthesis, characterization, applications, and challenges of iron oxide nanoparticles," *Nanotechnology, Science and Applications*, 2016.

[17] V. Mailänder and K. Landfester, "Interaction of nanoparticles with cells," *Biomacromolecules*, vol. 10, no. 9, pp. 2379–2400, 2009.

[18] F. Mazuel, A. Espinosa, N. Luciani, M. Reffay, R. Le Borgne, L. Motte, K. Desboeufs, A. Michel, T. Pellegrino, Y. Lalatonne, and C. Wilhelm, "Massive intracellular biodegradation of iron oxide nanoparticles evidenced magnetically at single-endosome and tissue levels," *ACS Nano*, vol. 10, no. 8, pp. 7627–7638, 2016.

[19] S. J. Soenen, U. Himmelreich, N. Nuytten, and M. D. Cuyper, "Cytotoxic effects of iron oxide nanoparticles and implications for safety in cell labelling," *Biomaterials*, vol. 32, no. 1, pp. 195 – 205, 2011.

[20] R. D. Corato, A. Espinosa, L. Lartigue, M. Tharaud, S. Chat, T. Pellegrino, C. Ménager, F. Gazeau, and C. Wilhelm, "Magnetic hyperthermia efficiency in the cellular environment for different nanoparticle designs," *Biomaterials*, vol. 35, no. 24, pp. 6400–6411, 2014.

[21] D. Bobo, K. J. Robinson, J. Islam, K. J. Thurecht, and S. R. Corrie, "Nanoparticle-based medicines: A review of fda-approved materials and clinical trials to date," *Pharmaceutical Research*, vol. 33, pp. 2373–2387, Oct 2016.

[22] M. Kendall and I. Lynch, "Long-term monitoring for nanomedicine implants and drugs," *Nature Nanotechnology*, 2016.

[23] Y.-X. J. Wang, "Superparamagnetic iron oxide based mri contrast agents: Current status of clinical application," *Quantitative Imaging in Medicine and Surgery*, vol. 1, no. 1, 2011.

[24] U. Bulbake, S. Doppalapudi, N. Kommineni, and W. Khan, "Liposomal formulations in clinical use: An updated review," *Pharmaceutics*, 2017.

[25] A. Bangham and R. Horne, "Negative staining of phospholipids and their structural modification by surface-active agents as observed in the electron microscope," *Journal of Molecular Biology*, 1964.

[26] G. Gregoriadis, "Drug entrapment in liposomes," *FEBS Letters*, vol. 36, no. 3, pp. 292–296, 1973.

[27] E. Reimhult, "Nanoparticle-triggered release from lipid membrane vesicles," *New Biotechnology*, vol. 32, no. 6, pp. 665–672, 2015. European Congress of Biotechnology - ECB 16.

[28] Y. Malam, M. Loizidou, and A. M. Seifalian, "Liposomes and nanoparticles: nanosized vehicles for drug delivery in cancer," *Trends in Pharmacological Sciences*, vol. 30, no. 11, pp. 592–599, 2009.

[29] M. Agrawal, Ajazuddin, D. K. Tripathi, S. Saraf, S. Saraf, S. G. Antimisiaris, S. Mourtas, M. Hammarlund-Udenaes, and A. Alexander, "Recent advancements in liposomes targeting strategies to cross blood-brain barrier (bbb) for the treatment of alzheimer's disease," *Journal of Controlled Release*, vol. 260, pp. 61–77, 2017.

[30] M. D. Cuyper and M. Joniau, "Magnetoliposomes," *European Biophysics Journal*, vol. 15, pp. 311–319, Feb 1988.

[31] P. Pradhan, J. Giri, F. Rieken, C. Koch, O. Mykhaylyk, M. Döblinger, R. Banerjee, D. Bahadur, and C. Plank, "Targeted temperature sensitive magnetic liposomes for thermochemotherapy," *Journal of Controlled Release*, vol. 142, no. 1, pp. 108–121, 2010.

[32] H. Guo, W. Chen, X. Sun, Y.-N. Liu, J. Li, and J. Wang, "Theranostic magnetoliposomes coated by carboxymethyl dextran with controlled release by low-frequency alternating magnetic field,"

Carbohydrate Polymers, vol. 118, no. Supplement C, pp. 209–217, 2015.

[33] S. S. Lucky, K. C. Soo, and Y. Zhang, "Nanoparticles in photodynamic therapy," *Chemical Reviews*, vol. 115, no. 4, pp. 1990–2042, 2015.

[34] B. S. Pattni, V. V. Chupin, and V. P. Torchilin, "New developments in liposomal drug delivery," *Chemical Reviews*, vol. 115, no. 19, pp. 10938–10966, 2015.

[35] A. Samad, Y. Sultana, and M. Aqil, "Liposomal drug delivery systems: An update review," *Current Drug Delivery*, vol. 4, no. 4, pp. 297–305, 2007.

[36] M. Marciello, J. Pellico, I. Fernandez-Barahona, F. Herranz, J. Ruiz-Cabello, and M. Filice, "Recent advances in the preparation and application of multifunctional iron oxide and liposome-based nanosystems for multimodal diagnosis and therapy," *Interface Focus*, vol. 6, no. 6, 2016.

[37] H. Basoglu, M. D. Bilgin, and M. M. Demir, "Protoporphyrin ix-loaded magnetoliposomes as a potential drug delivery system for photodynamic therapy: Fabrication, characterization and in vitro study," *Photodiagnosis and Photodynamic Therapy*, vol. 13, no. Supplement C, pp. 81–90, 2016.

[38] G. D. Bothun and M. R. Preiss, "Bilayer heating in magnetite nanoparticle–liposome dispersions via fluorescence anisotropy," *Journal of Colloid and Interface Science*, vol. 357, no. 1, pp. 70–74, 2011.

[39] Y. Chen, A. Bose, and G. D. Bothun, "Controlled release from bilayer-decorated magnetoliposomes via electromagnetic heating," *ACS Nano*, vol. 4, no. 6, pp. 3215–3221, 2010.

[40] M. Babincová, P. Cicmanec, V. Altanerová, C. Altaner, and P. Babinec, "Ac-magnetic field controlled drug release from magnetoliposomes: design of a method for site-specific chemotherapy," *Bioelectrochemistry*, vol. 55, pp. 17–19, January 2002.

[41] H. R. Samadikhah, A. Majidi, M. Nikkhah, and S. Hosseinkhani, "Preparation, characterization, and efficient transfection of cationic liposomes and nanomagnetic cationic liposomes," *International Journal of Nanomedicine*, 2011.

[42] C. Hao, J. Li, W. Mu, L. Zhu, J. Yang, H. Liu, B. Li, S. Chen, and R. Sun, "Adsorption behavior of magnetite nanoparticles into the dppc model membranes," *Applied Surface Science*, vol. 362, no. Supplement C, pp. 121 – 125, 2016.

[43] E. M. Curtis, A. H. Bahrami, T. R. Weikl, and C. K. Hall, "Modeling nanoparticle wrapping or translocation in bilayer membranes," *Nanoscale*, vol. 7, pp. 14505–14514, 2015.

[44] R. V. Ferreira, T. M. da Mata Martins, A. M. Goes, J. D. Fabris, L. C. D. Cavalcante, L. E. F. Outon, and R. Z. Domingues, "Thermosensitive gemcitabine-magnetoliposomes for combined hyperthermia and chemotherapy," *Nanotechnology*, vol. 27, no. 8, p. 085105, 2016.

[45] E. Amstad, J. Kohlbrecher, E. Müller, T. Schweizer, M. Textor, and E. Reimhult, "Triggered release from liposomes through magnetic actuation of iron oxide nanoparticle containing membranes," *Nano Letters*, vol. 11, no. 4, pp. 1664–1670, 2011.

[46] G. Béalle, R. D. Corato, J. Kolosnjaj-Tabi, V. Dupuis, O. Clément, F. Gazeau, C. Wilhelm, and C. Ménager, "Ultra magnetic liposomes for mr imaging, targeting, and hyperthermia," *Langmuir*, vol. 28, no. 32, pp. 11834–11842, 2012.

[47] R. D. Corato, G. Béalle, J. Kolosnjaj-Tabi, A. Espinosa, O. Clément, A. K. A. Silva, C. Ménager, and C. Wilhelm, "Combining magnetic hyperthermia and photodynamic therapy for tumor ablation with photoresponsive magnetic liposomes," *ACS Nano*, vol. 9, no. 3, pp. 2904–2916, 2015.

[48] V. V. Ginzburg and S. Balijepalli, "Modeling the thermodynamics of the interaction of nanoparticles with cell membranes," *Nano Letters*, vol. 7, no. 12, pp. 3716–3722, 2007.

[49] B. Du, S. Han, H. Li, F. Zhao, X. Su, X. Cao, and Z. Zhang, "Multi-functional liposomes showing radiofrequency-triggered release and magnetic resonance imaging for tumor multi-mechanism therapy," *Nanoscale*, vol. 7, pp. 5411–5426, 2015.

[50] A. Joniec, S. Sek, and P. Krysinski, "Magnetoliposomes as potential carriers of doxorubicin to tumours," *Chemistry–A European Journal*, vol. 22, no. 49, pp. 17715–17724, 2016.

[51] Y. Namiki, T. Namiki, and H. Yoshida, "A novel magnetic crystal–lipid nanostructure for magnetically guided in vivo gene delivery," *Nature Nanotechnology*, 2009.

[52] C. J. Meledandri, T. Ninjbadgar, and D. F. Brougham, "Size-controlled magnetoliposomes with tunable magnetic resonance relaxation enhancements," *J. Mater. Chem.*, vol. 21, pp. 214–222, 2011.

[53] E. R. Cintra, F. S. Ferreira, J. L. S. Junior, J. C. Campello, L. M. Socolovsky, E. M. Lima, and A. F. Bakuzis, "Nanoparticle agglomerates in magnetoliposomes," *Nanotechnology*, vol. 20, no. 4, p. 045103, 2009.

[54] T. Kubo, T. Sugita, S. Shimose, Y. Nitta, Y. Ikuta, and T. Murakami, "Targeted delivery of anticancer drugs with intravenously administered magnetic liposomes in osteosarcoma-bearing hamsters," *International Journal of Oncology*, 2000.

[55] G. Mikhaylov, U. Mikac, A. A. Magaeva, and V. I. Itin, "Ferri-liposomes as an mri-visible drug-delivery system for targeting tumours and their microenvironment," *Nature Nanotechnology*, 2011.

[56] M.-S. Martina, J.-P. Fortin, C. Ménager, O. Clément, G. Barratt, C. Grabielle-Madelmont, F. Gazeau, V. Cabuil, and S. Lesieur, "Generation of superparamagnetic liposomes revealed as highly efficient mri contrast agents for in vivo imaging," *Journal of the American Chemical Society*, vol. 127, no. 30, pp. 10676–10685, 2005.

[57] S. Nappini, T. A. Kayal, D. Berti, B. Nordèn, and P. Baglioni, "Magnetically triggered release from giant unilamellar vesicles: Visualization by means of confocal microscopy," *The Journal of Physical Chemistry Letters*, vol. 2, no. 7, pp. 713–718, 2011.

[58] D. D. Von Hoff, M. W. Layard, P. Basa, H. L. Davis, A. L. Von Hoff, M. Rozencweig, and F. M. Muggia, "Risk factors for doxorubicin-lnduced congestive heart failure," *Annals of Internal Medicine*, vol. 91, no. 5, pp. 710–717, 1979.

[59] R. M. Cornell and U. Schwertmann, "The iron oxides: Structure, properties, reactions, occurences and uses," *Wiley-VCH*, pp. 1–705, 2004.

[60] A. Winkleman, K. L. Gudiksen, D. Ryan, G. M. Whitesides, D. Greenfield, and M. Prentiss, "A magnetic trap for living cells suspended in a paramagnetic buffer," *Applied Physics Letters*, vol. 85, no. 12, pp. 2411–2413, 2004.

[61] A. Yamagishi, "Biological systems in high magnetic field," *Journal of Magnetism and Magnetic Materials*, 1990.

[62] K. L. Bren, R. Eisenberg, and H. B. Gray, "Discovery of the magnetic behavior of hemoglobin: A beginning of bioinorganic chemistry," *Proceedings of the National Academy of Sciences*, vol. 112, no. 43, pp. 13123–13127, 2015.

[63] S. Laurent, D. Forge, M. Port, A. Roch, C. Robic, L. Vander Elst, and R. N. Muller, "Magnetic iron oxide nanoparticles: Synthesis, stabilization, vectorization, physicochemical characterizations, and biological applications," *Chemical Reviews*, vol. 108, no. 6, pp. 2064–2110, 2008.

[64] S. Oyarzún, A. Tamion, F. Tournus, V. Dupuis, and M. Hillenkamp, "Size effects in the magnetic anisotropy of embedded cobalt nanoparticles: from shape to surface," *Scientific Reports*, 2015.

[65] N. Training, "Magnetic nanoparticles: Standardisation and biomedical applications," *e-Learning course*, 2016.

[66] K. M. Krishnan, "Biomedical nanomagnetics: A spin through possibilities in imaging, diagnostics, and therapy," *IEEE Transactions on Magnetics*, vol. 46, pp. 2523–2558, July 2010.

[67] C. P. Bean and J. D. Livingston, "Superparamagnetism," *Journal of Applied Physics*, vol. 30, no. 4, pp. S120–S129, 1959.

[68] M. Knobel, W. Nunes, L. Socolovsky, E. De Biasi, J. Vargas, and J. Denardin, "Superparamagnetism and other magnetic features in granular materials: A review on ideal and real systems," *Journal of Nanoscience and Nanotechnology*, vol. 8, pp. 2836–2857, 6 2008.

[69] P. de la Presa, Y. Luengo, M. Multigner, R. Costo, M. P. Morales, G. Rivero, and A. Hernando, "Study of heating efficiency as a function of concentration, size, and applied field in fe2o3 nanoparticles," *The Journal of Physical Chemistry C*, vol. 116, no. 48, pp. 25602–25610, 2012.

[70] L. Gutiérrez, F. J. Lázaro, A. R. Abadía, M. S. Romero, C. Quintana, M. P. Morales, C. Patiño, and R. Arranz, "Bioinorganic transformations of liver iron deposits observed by tissue magnetic characterisation in a rat model," *Journal of Inorganic Biochemistry*, vol. 100, no. 11, pp. 1790–1799, 2006.

[71] E. C. Vreeland, J. Watt, G. B. Schober, B. G. Hance, M. J. Austin, A. D. Price, B. D. Fellows, T. C. Monson, N. S. Hudak, L. Maldonado-Camargo, A. C. Bohorquez, C. Rinaldi, and D. L. Huber, "Enhanced nanoparticle size control by extending lamer's mechanism," *Chemistry of Materials*, 2015.

[72] V. K. Lamer and R. H. Dinega, "Theory, production and mechanism of formation of monodispersed hydrosols," *Journal of the American Chemical Society*, 1950.

[73] V. K. LaMer, "Nucleation in phase transitions.," *Industrial and Engineering Chemistry*, vol. 44, no. 6, pp. 1270–1277, 1952.

[74] N. T. K. Thanh, N. Maclean, and S. Mahiddine, "Mechanisms of nucleation and growth of nanoparticles in solution," *Chemical Reviews*, vol. 114, no. 15, pp. 7610–7630, 2014.

[75] N. R. Jana, Y. Chen, and X. Peng, "Size- and shape-controlled magnetic (cr, mn, fe, co, ni) oxide nanocrystals via a simple and general approach," *Chemistry of Materials*, vol. 16, no. 20, pp. 3931–3935, 2004.

[76] T. Sugimoto, "Monodispersed particles," *Elsevier Science*, 2001.

[77] S. Sun and H. Zeng, "Size-controlled synthesis of magnetite nanoparticles," *Journal of the American Chemical Society*, vol. 124, no. 28, pp. 8204–8205, 2002.

[78] C. Moya, X. Batlle, and A. Labarta, "The effect of oleic acid on the synthesis of fe3-xo4 nanoparticles over a wide size range," *Phys. Chem. Chem. Phys.*, vol. 17, pp. 27373–27379, 2015.

[79] W. Baaziz, B. P. Pichon, S. Fleutot, Y. Liu, C. Lefevre, J.-M. Greneche, M. Toumi, T. Mhiri, and S. Begin-Colin, "Magnetic iron oxide nanoparticles: Reproducible tuning of the size and nanosized-dependent composition, defects, and spin canting," *The Journal of Physical Chemistry C*, vol. 118, no. 7, pp. 3795–3810, 2014.

[80] M. V. Kovalenko, M. I. Bodnarchuk, R. T. Lechner, G. Hesser, F. Schaffler, and W. Heiss, "Fatty acid salts as stabilizers in size and shape controlled nanocrystal synthesis, the case of inverse spinel iron oxide," *Journal of the American Chemical Society*, 2007.

[81] D. Kim, N. Lee, M. Park, B. H. Kim, K. An, and T. Hyeon, "Synthesis of uniform ferrimagnetic magnetite nanocubes," *Journal of the American Chemical Society*, vol. 131, no. 2, pp. 454–455, 2009.

[82] A. G. Roca, L. Gutiérrez, H. Gavilán, M. E. F. Brollo, S. Veintemillas-Verdaguer, and M. del Puerto Morales, "Design strategies for shape-controlled magnetic iron oxide nanoparticles," *Advanced Drug Delivery Reviews*, 2018.

[83] S. He, H. Zhang, Y. Liu, F. Sun, X. Yu, X. Li, L. Zhang, L. Wang, K. Mao, G. Wang, Y. Lin, Z. Han, R. Sabirianov, and H. Zeng,

"Maximizing specific loss power for magnetic hyperthermia by hard–soft mixed ferrites," *Small*, vol. 14, no. 29, p. 1800135, 2018.

[84] M. Baghbanzadeh, L. Carbone, and P. D. C. C. O. Kappe, "Microwave-assisted synthesis of colloidal inorganic nanocrystals," *Angewandte Chemie International Edition*, vol. 50, no. 48, pp. 11312–11359, 2011.

[85] R. Gedye, F. Smith, K. Westaway, H. Ali, L. Baldisera, L. Laberge, and J. Rousell, "The use of microwave oven for rapid organic synthesis," *Tetrahedron Letters*, 1986.

[86] R. J. Giguere, T. L. Bray, and S. M. Duncan, "Application of commercial microwave ovens to organic synthesis," *Tetrahedron Letters*, 1986.

[87] B. L. Hayes, "Microwave synthesis: Chemistry at the speed of light," *CEM*, 2002.

[88] J. S. Schanche, "Microwave synthesis solutions from personal chemistry," *Molecular Diversity*, vol. 7, pp. 291–298, Jun 2003.

[89] C. O. Kappe, D. Dallinger, and S. S. Murphree, "Practical microwave synthesis for organic chemists," *WILEY-VCH*, 2009.

[90] S. Komarneni, "Nanophase materials by hydrothermal, microwave-hydrothermal and microwave-solvothermal methods," *Current Science*, vol. 85, no. 12, pp. 1730–1734, 2003.

[91] M. Tsuji, M. Hashimoto, Y. Nishizawa, M. Kubokawa, and T. Tsuji, "Microwave-assisted synthesis of metallic nanostructures in solution," *Chemistry – A European Journal*, vol. 11, no. 2, pp. 440–452, 2005.

[92] Y. Tetsushi, W. Yuji, S. Takao, M. Hirotaro, G. Masaki, H. Shingo, and Y. Shozo, "Microwave-assisted preparation of silver nanoparticles," *Chemistry Letters*, vol. 33, no. 2, pp. 158–159, 2004.

[93] M. Tsuji, N. Miyamae, S. Lim, K. Kimura, X. Zhang, S. Hikino, and M. Nishio, "Crystal structures and growth mechanisms of au@ag core-shell nanoparticles prepared by the microwave-polyol method," *Crystal Growth and Design*, vol. 6, no. 8, pp. 1801–1807, 2006.

[94] M. Niederberger and N. Pinna, "Metal oxide nanoparticles in organic solvents," *Springer-Verlag London*, 2009.

[95] I. Bilecka, I. Djerdj, and M. Niederberger, "One-minute synthesis of crystalline binary and ternary metal oxide nanoparticles," *Chem. Commun.*, pp. 886–888, 2008.

[96] H. Hu, H. Yang, P. Huang, D. Cui, Y. Peng, J. Zhang, F. Lu, J. Lian, and D. Shi, "Unique role of ionic liquid in microwave-assisted synthesis of monodisperse magnetite nanoparticles," *Chem. Commun.*, vol. 46, pp. 3866–3868, 2010.

[97] Z. Ai, K. Deng, Q. Wan, L. Zhang, and S. Lee, "Facile microwave-assisted synthesis and magnetic and gas sensing properties of $fe3o4$ nanoroses," *The Journal of Physical Chemistry C*, vol. 114, no. 14, pp. 6237–6242, 2010.

[98] J. Pellico, A. V. Lechuga-Vieco, E. Almarza, A. Hidalgo, C. Mesa-Nuñez, I. Fernández-Barahona, J. A. Quintana, J. Bueren, J. A. Enríquez, J. Ruiz-Cabello, and F. Herranz, "In vivo imaging of lung inflammation with neutrophil-specific 68ga nano-radiotracer," *Scientific Reportsvolume*, 2017.

[99] K. Westaway and R. Gedye, "The question of specific activation of organic reactions by microwaves," *Journal of Microwave Power and Electromagnetic Energy*, vol. 30, no. 4, pp. 219–230, 1995.

[100] F. Langa, P. de la Cruz, A. de la Hoz, A. Díaz-Ortiz, and E. Díez-Barra, "Microwave irradiation: more than just a method for accelerating reactions," *Contemp. Org. Synth.*, vol. 4, pp. 373–386, 1997.

[101] L. Perreux and A. Loupy, "A tentative rationalization of microwave effects in organic synthesis according to the reaction

medium, and mechanistic considerations," *Tetrahedron*, vol. 57, no. 45, pp. 9199 – 9223, 2001.

[102] N. Kuhnert, "Microwave-assisted reactions in organic synthesis—are there any nonthermal microwave effects?," *Angewandte Chemie International Edition*, vol. 41, no. 11, pp. 1863–1866, 2002.

[103] S. Santra and P. R. Andreana, "A one-pot, microwave-influenced synthesis of diverse small molecules by multicomponent reaction cascades," *Organic Letters*, vol. 9, no. 24, pp. 5035–5038, 2007.

[104] D. Obermayer and C. O. Kappe, "On the importance of simultaneous infrared/fiber-optic temperature monitoring in the microwave-assisted synthesis of ionic liquids," *Org. Biomol. Chem.*, vol. 8, pp. 114–121, 2010.

[105] D. Lasic, "Liposomes: From physics to applications," *Elsevier Science Ltd*, 1993.

[106] T. Heimburg, "A model for the lipid pretransition: Coupling of ripple formation with the chain-melting transition," *Biophysical Journal*, vol. 78, no. 3, pp. 1154–1165, 2000.

[107] H. S. Wi, K. Lee, and H. K. Pak, "Interfacial energy consideration in the organization of a quantum dot–lipid mixed system," *Journal of Physics: Condensed Matter*, vol. 20, no. 49, p. 494211, 2008.

[108] S. K. Jat and R. R. Bhattacharjee, "Colloidal magnetic nanoparticles coated with self-dissolving mixed fatty acid bilayer: A novel host–guest material for controlled release applications," *Colloids and Surfaces A: Physicochemical and Engineering Aspects*, vol. 529, pp. 160–168, 2017.

[109] J. A. Kulkarni, Y. Y. C. Tam, S. Chen, Y. K. Tam, J. Zaifman, P. R. Cullis, and S. Biswas, "Rapid synthesis of lipid nanoparticles containing hydrophobic inorganic nanoparticles," *Nanoscale*, vol. 9, pp. 13600–13609, 2017.

[110] S.-H. Park, S.-G. Oh, J.-Y. Mun, and S.-S. Han, "Effects of silver nanoparticles on the fluidity of bilayer in phospholipid liposome," *Colloids and Surfaces B: Biointerfaces*, vol. 44, no. 2, pp. 117–122, 2005.

[111] S.-H. Park, S.-G. Oh, J.-Y. Mun, and S.-S. Han, "Loading of gold nanoparticles inside the dppc bilayers of liposome and their effects on membrane fluidities," *Colloids and Surfaces B: Biointerfaces*, vol. 48, no. 2, pp. 112–118, 2006.

[112] G. D. Bothun, "Hydrophobic silver nanoparticles trapped in lipid bilayers: Size distribution, bilayer phase behavior, and optical properties," *Journal of Nanobiotechnology*, vol. 6, p. 13, Nov 2008.

[113] M. S. E., "Nanoparticle therapeutics: a personal perspective," *Wiley Interdisciplinary Reviews: Nanomedicine and Nanobiotechnology*, vol. 1, no. 3, pp. 264–271, 2009.

[114] U. Sakulkhu, M. Mahmoudi, L. Maurizi, G. Coullerez, M. Hofmann-Amtenbrink, M. Vries, M. Motazacker, F. Rezaee, and H. Hofmann, "Significance of surface charge and shell material of superparamagnetic iron oxide nanoparticle (spion) based core/shell nanoparticles on the composition of the protein corona," *Biomater. Sci.*, vol. 3, pp. 265–278, 2015.

[115] G. Stepien, M. Moros, M. Pérez-Hernández, M. Monge, L. Gutiérrez, R. M. Fratila, M. d. las Heras, S. Menao Guillén, J. J. Puente Lanzarote, C. Solans, J. Pardo, and J. M. de la Fuente, "Effect of surface chemistry and associated protein corona on the long-term biodegradation of iron oxide nanoparticles in vivo," *ACS Applied Materials and Interfaces*, vol. 10, no. 5, pp. 4548–4560, 2018.

[116] A. E. Nel, L. Mädler, D. Velegol, T. Xia, E. M. V. Hoek, P. Somasundaran, F. Klaessig, V. Castranova, and M. Thompson, "Understanding biophysicochemical interactions at the nano–bio interface," *Nature Materials*, 2009.

[117] H. T. R. Wiogo, M. Lim, V. Bulmus, L. Gutiérrez, R. C. Woodward, and R. Amal, "Insight into serum protein interactions

with functionalized magnetic nanoparticles in biological media," *Langmuir*, vol. 28, no. 9, pp. 4346–4356, 2012.

[118] A. Verma and F. Stellacci, "Effect of surface properties on nanoparticle–cell interactions," *Small*, vol. 6, no. 1, pp. 12–21, 2010.

[119] Y. Luengo, S. Nardecchia, M. P. Morales, and M. C. Serrano, "Different cell responses induced by exposure to maghemite nanoparticles," *Nanoscale*, vol. 5, pp. 11428–11437, 2013.

[120] P. P. Fu, Q. Xia, H.-M. Hwang, P. C. Ray, and H. Yu, "Mechanisms of nanotoxicity: Generation of reactive oxygen species," *Journal of Food and Drug Analysis*, vol. 22, no. 1, pp. 64–75, 2014. Nanomaterials - Toxicology and Medical Applications.

[121] H. Hillaireau and P. Couvreur, "Nanocarriers' entry into the cell: relevance to drug delivery," *Cellular and Molecular Life Sciences*, vol. 66, no. 17, pp. 2873–2896, 2009.

[122] R. Agarwal, I. Iezhitsa, P. Agarwal, N. A. A. Nasir, N. Razali, R. Alyautdin, and N. M. Ismail, "Liposomes in topical ophthalmic drug delivery: an update," *Drug Delivery*, vol. 23, no. 4, pp. 1075–1091, 2016.

[123] G. Bozzuto and A. Molinari, "Liposomes as nanomedical devices," *International Journal of Nanomedicine*, 2015.

[124] D. Kanduc, A. Mittelman, R. Serpico, E. Sinigaglia, A. A. Sinha, C. Natale, R. Santacroce, M. G. Di Corcia, A. Lucchese, L. Dini, P. Pani, S. Santacroce, S. Simone, R. Bucci, and E. Farber, "Cell death: Apoptosis versus necrosis," *International Journal of Oncology*, 2002.

[125] R. Rosensweig, "Heating magnetic fluid with alternating magnetic field," *Journal of Magnetism and Magnetic Materials*, vol. 252, pp. 370–374, 2002. Proceedings of the 9th International Conference on Magnetic Fluids.

[126] I. Obaidat, B. Issa, and Y. Haik, "Magnetic properties of magnetic nanoparticles for efficient hyperthermia," *Nanomaterials*, vol. 5, p. 63–89, Jan 2015.

[127] M. L. Immordino, F. Dosio, and L. Cattel, "Stealth liposomes: review of the basic science, rationale, and clinical applications, existing and potential," *International Journal of Nanomedicine*, 2006.

[128] S. Kralj, T. Potrc, P. Kocbek, S. Marchesan, and D. Makovec, "Design and fabrication of magnetically responsive nanocarriers for drug delivery," *Current Medicinal Chemistry*, vol. 24, no. 5, pp. 454–469, 2017.

[129] L. Sercombe, T. Veerati, F. Moheimani, S. Y. Wu, A. K. Sood, and S. Hua, "Advances and challenges of liposome assisted drug delivery," *Frontiers in pharmacology*, 2015.

[130] M. Cagel, E. Grotz, E. Bernabeu, M. A. Moretton, and D. A. Chiappetta, "Doxorubicin: nanotechnological overviews from bench to bedside," *Drug Discovery Today*, vol. 22, no. 2, pp. 270–281, 2017.

[131] J. Park, K. An, Y. Hwang, J.-G. Park, H.-J. Noh, J.-Y. Kim, J.-H. Park, N.-M. Hwang, and T. Hyeon, "Ultra-large-scale syntheses of monodisperse nanocrystals," *Nature Materials*, 2004.

[132] A. G. Roca, M. P. Morales, K. O'Grady, and C. J. Serna, "Structural and magnetic properties of uniform magnetite nanoparticles prepared by high temperature decomposition of organic precursors," *Nanotechnology*, vol. 17, no. 11, p. 2783, 2006.

[133] G. Salas, C. Casado, F. J. Teran, R. Miranda, C. J. Serna, and M. P. Morales, "Controlled synthesis of uniform magnetite nanocrystals with high-quality properties for biomedical applications," *J. Mater. Chem.*, vol. 22, pp. 21065–21075, 2012.

[134] N. Fauconnier, J. Pons, J. Roger, and A. Bee, "Thiolation of maghemite nanoparticles by dimercaptosuccinic acid," *Journal of Colloid and Interface Science*, vol. 194, no. 2, pp. 427–433, 1997.

[135] F. Szoka and D. Papahadjopoulos, "Procedure for preparation of liposomes with large internal aqueous space and high capture by

reverse-phase evaporation," *Proceedings of the National Academy of Sciences*, vol. 75, no. 9, pp. 4194–4198, 1978.

[136] A. Akbarzadeh, R. Rezaei-Sadabady, S. Davaran, S. W. Joo, N. Zarghami, Y. Hanifehpour, M. Samiei, M. Kouhi, and K. Nejati-Koshki, "Liposome: classification, preparation, and applications," *Nanoscale Research Letters*, vol. 8, p. 102, Feb 2013.

[137] S. C. de Araújo Lopes, C. dos Santos Giuberti, T. G. R. Rocha, D. dos Santos Ferreira, E. A. Leite, and M. C. Oliveira, "Liposomes as carriers of anticancer drugs," *IntechOpen*, 2013.

[138] T. Allen, "Particle size measurement," *Springer Netherlands*, 1997.

[139] J. M. Rojas, H. Gavilán, V. del Dedo, E. Lorente-Sorolla, L. Sanz-Ortega, G. B. da Silva, R. Costo, S. Perez-Yagüe, M. Talelli, M. Marciello, M. P. Morales, D. F. Barber, and L. Gutiérrez, "Time-course assessment of the aggregation and metabolization of magnetic nanoparticles," *Acta Biomaterialia*, vol. 58, pp. 181–195, 2017.

[140] B. Cullity and S. Stock, "Elements of x-ray diffraction," *Pearson*, 2001.

[141] G. Mie, "Contributions to the optics of turbid media, particularly of colloidal metal solutions," 1976.

[142] J. Pellico, A. V. Lechuga-Vieco, M. Benito, J. M. Garcia-Segura, V. Fuster, J. Ruiz-Cabello, and F. Herranz, "Microwave-driven synthesis of bisphosphonate nanoparticles allows in vivo visualisation of atherosclerotic plaque," *RSC Adv.*, vol. 5, pp. 1661–1665, 2015.

[143] D. Burdinski and C. Bohlender, "Synthesis and use of iron oleate," *Patent US*, 2013.

[144] A. K. Peacock, S. I. Cauet, A. Taylor, P. Murray, S. R. Williams, J. V. M. Weaver, D. J. Adams, and M. J.

Rosseinsky, "Poly[2-(methacryloyloxy)ethylphosphorylcholine]-coated iron oxide nanoparticles: synthesis, colloidal stability and evaluation for stem cell labelling," *Chem. Commun.*, vol. 48, pp. 9373–9375, 2012.

[145] M. E. F. Brollo, S. Veintemillas-Verdaguer, C. M. Salván, and M. del Puerto Morales, "Key parameters on the microwave assisted synthesis of magnetic nanoparticles for mri contrast agents," *Contrast Media and Molecular Imaging*, 2017.

[146] L. M. Bronstein, X. Huang, J. Retrum, A. Schmucker, M. Pink, B. D. Stein, and B. Dragnea, "Influence of iron oleate complex structure on iron oxide nanoparticle formation," *Chemistry of Materials*, vol. 19, no. 15, pp. 3624–3632, 2007.

[147] V. Robert and G. Lemercier, "A combined experimental and theoretical study of carboxylate coordination modes: A structural probe," *Journal of the American Chemical Society*, vol. 128, no. 4, pp. 1183–1187, 2006.

[148] W. W. Yu, J. C. Falkner, C. T. Yavuz, and V. L. Colvin, "Synthesis of monodisperse iron oxide nanocrystals by thermal decomposition of iron carboxylate salts," *Chem. Commun.*, pp. 2306–2307, 2004.

[149] E. Carenza, V. Barceló, A. Morancho, J. Montaner, A. Rosell, and A. Roig, "Rapid synthesis of water-dispersible superparamagnetic iron oxide nanoparticles by a microwave-assisted route for safe labeling of endothelial progenitor cells," *Acta Biomaterialia*, vol. 10, no. 8, pp. 3775–3785, 2014.

[150] L. Gonzalez-Moragas, S.-M. Yu, N. Murillo-Cremaes, A. Laromaine, and A. Roig, "Scale-up synthesis of iron oxide nanoparticles by microwave-assisted thermal decomposition," *Chemical Engineering Journal*, vol. 281, no. Supplement C, pp. 87–95, 2015.

[151] O. Pascu, E. Carenza, M. Gich, S. Estradé, F. Peiró, G. Herranz, and A. Roig, "Surface reactivity of iron oxide nanoparticles by microwave-assisted synthesis; comparison with the ther-

mal decomposition route," *The Journal of Physical Chemistry C*, vol. 116, no. 28, pp. 15108–15116, 2012.

[152] H. Sharifi Dehsari, A. Halda Ribeiro, B. Ersöz, W. Tremel, G. Jakob, and K. Asadi, "Effect of precursor concentration on size evolution of iron oxide nanoparticles," *CrystEngComm*, vol. 19, pp. 6694–6702, 2017.

[153] S. Sun, H. Zeng, D. B. Robinson, S. Raoux, P. M. Rice, S. X. Wang, and G. Li, "Monodisperse mfe2o4 (m = fe, co, mn) nanoparticles," *Journal of the American Chemical Society*, vol. 126, no. 1, pp. 273–279, 2004.

[154] Y. Yin and A. P. Alivisatos, "Colloidal nanocrystal synthesis and the organic–inorganic interface," *Nature*, 2004.

[155] K. Rana and S. Rana, "Microwave reactors: A brief review on its fundamental aspects and applications," *Open Access Library Journal*, 2014.

[156] B. Gillot, F. Jemmali, and A. Rousset, "Infrared studies on the behavior in oxygen of cobalt-substituted magnetites: Comparison with zinc-substituted magnetites," *Journal of Solid State Chemistry*, vol. 50, no. 2, pp. 138–145, 1983.

[157] A. Ruiz, P. C. Morais, R. Bentes de Azevedo, Z. G. M. Lacava, A. Villanueva, and M. del Puerto Morales, "Magnetic nanoparticles coated with dimercaptosuccinic acid: development, characterization, and application in biomedicine," *Journal of Nanoparticle Research*, vol. 16, p. 2589, Oct 2014.

[158] M. Blanco-Mantecón and K. O'Grady, "Interaction and size effects in magnetic nanoparticles," *Journal of Magnetism and Magnetic Materials*, vol. 296, no. 2, pp. 124–133, 2006.

[159] F. Ahrentorp, A. P. Astalan, C. Jonasson, J. Blomgren, B. Qi, O. T. Mefford, M. Yan, J. Courtois, J. Berret, J. Fresnais, O. Sandre, S. Dutz, R. Müller, and C. Johansson, "Sensitive high frequency ac susceptometry in magnetic nanoparticle applications," *AIP Conference Proceedings*, vol. 1311, no. 1, pp. 213–223, 2010.

[160] D. Soukup, S. Moise, E. Céspedes, J. Dobson, and N. D. Telling, "In situ measurement of magnetization relaxation of internalized nanoparticles in live cells," *ACS Nano*, vol. 9, no. 1, pp. 231–240, 2015.

[161] F. Ahrentorp, A. Astalan, J. Blomgren, C. Jonasson, E. Wetterskog, P. Svedlindh, A. Lak, F. Ludwig, L. J. van IJzendoorn, F. Westphal, C. Grüttner, N. Gehrke, S. Gustafsson, E. Olsson, and C. Johansson, "Effective particle magnetic moment of multicore particles," *Journal of Magnetism and Magnetic Materials*, vol. 380, pp. 221 – 226, 2015.

[162] T. Inoue, S. ichi Yanagihara, Y. Misono, and M. Suzuki, "Effect of fatty acids on phase behavior of hydrated dipalmitoylphosphatidylcholine bilayer: saturated versus unsaturated fatty acids," *Chemistry and Physics of Lipids*, vol. 109, no. 2, pp. 117–133, 2001.

[163] M. E. F. Brollo, P. Hernandez Flores, L. Gutierrez, C. Johansson, D. F. Barber, and M. d. P. Morales, "Magnetic properties of nanoparticles as a function of their spatial distribution on liposomes and cells," *Phys. Chem. Chem. Phys.*, vol. 20, pp. 17829–17838, 2018.

[164] T. Nilsson, C. R. Lundin, G. N. P. Adelroth, C. von Ballmoos, and P. Brzezinski, "Lipid-mediated protein-protein interactions modulate respiration-driven atp synthesis," *Scientific Reports*, vol. 6, 2016.

[165] J. W. Bulte, M. de Cuyper, D. Despres, and J. A. Frank, "Preparation, relaxometry, and biokinetics of pegylated magnetoliposomes as mr contrast agent," *Journal of Magnetism and Magnetic Materials*, vol. 194, no. 1, pp. 204–209, 1999.

[166] S. Torquato, T. M. Truskett, and P. G. Debenedetti, "Is random close packing of spheres well defined?," *Phys. Rev. Lett.*, vol. 84, pp. 2064–2067, Mar 2000.

[167] J. C. Domingo, M. Mercadal, J. Petriz, and M. A. D. Madariaga, "Preparation of peg-grafted immunomagnetoliposomes entrapping citrate stabilized magnetite particles and their application

in cd34+ cell sorting," *Journal of Microencapsulation*, vol. 18, no. 1, pp. 41–54, 2001.

[168] M. L. Etheridge, K. R. Hurley, J. Zhang, S. Jeon, H. L. Ring, C. Hogan, C. L. Haynes, M. Garwood, and J. C. Bischof, "Accounting for biological aggregation in heating and imaging of magnetic nanoparticles," *TECHNOLOGY*, vol. 02, no. 03, pp. 214–228, 2014.

[169] A. Villanueva, M. Cañete, A. G. Roca, M. Calero, S. Veintemillas-Verdaguer, C. J. Serna, M. del Puerto Morales, and R. Miranda, "The influence of surface functionalization on the enhanced internalization of magnetic nanoparticles in cancer cells," *Nanotechnology*, vol. 20, no. 11, p. 115103, 2009.

[170] R. Mejías, S. Pérez-Yagüe, L. Gutiérrez, L. I. Cabrera, R. Spada, P. Acedo, C. J. Serna, F. J. Lázaro, Ángeles Villanueva, M. del Puerto Morales, and D. F. Barber, "Dimercaptosuccinic acid-coated magnetite nanoparticles for magnetically guided in vivo delivery of interferon gamma for cancer immunotherapy," *Biomaterials*, vol. 32, no. 11, pp. 2938–2952, 2011.

[171] P. Guardia, A. Riedinger, S. Nitti, G. Pugliese, S. Marras, A. Genovese, M. E. Materia, C. Lefevre, L. Manna, and T. Pellegrino, "One pot synthesis of monodisperse water soluble iron oxide nanocrystals with high values of the specific absorption rate," *J. Mater. Chem. B*, vol. 2, pp. 4426–4434, 2014.

[172] R. Mejías, L. Gutiérrez, G. Salas, S. Pérez-Yagüe, T. M. Zotes, F. J. Lázaro, M. P. Morales, and D. F. Barber, "Long term biotransformation and toxicity of dimercaptosuccinic acid-coated magnetic nanoparticles support their use in biomedical applications," *Journal of Controlled Release*, vol. 171, no. 2, pp. 225–233, 2013.

[173] J. G. Ovejero, D. Cabrera, J. Carrey, T. Valdivielso, G. Salas, and F. J. Teran, "Effects of inter- and intra-aggregate magnetic dipolar interactions on the magnetic heating efficiency of iron oxide nanoparticles," *Phys. Chem. Chem. Phys.*, vol. 18, pp. 10954–10963, 2016.

[174] M. Lévy, C. Wilhelm, M. Devaud, P. Levitz, and F. Gazeau, "How cellular processing of superparamagnetic nanoparticles affects their magnetic behavior and nmr relaxivity," *Contrast Media and Molecular Imaging*, vol. 7, no. 4, pp. 373–383, 2012.

[175] M. Levy, C. Wilhelm, N. Luciani, V. Deveaux, F. Gendron, A. Luciani, M. Devaud, and F. Gazeau, "Nanomagnetism reveals the intracellular clustering of iron oxide nanoparticles in the organism," *Nanoscale*, vol. 3, pp. 4402–4410, 2011.

[176] M. Safi, J. Courtois, M. Seigneuret, H. Conjeaud, and J.-F. Berret, "The effects of aggregation and protein corona on the cellular internalization of iron oxide nanoparticles," *Biomaterials*, vol. 32, no. 35, pp. 9353–9363, 2011.

[177] D. Cabrera, A. Coene, J. Leliaert, E. J. A. Ibanez, L. Dupre, N. D. Telling, and F. J. Teran, "Dynamical magnetic response of iron oxide nanoparticles inside live cells," *ACS Nano*, 2018.

[178] R. Mejías, P. Hernández Flores, M. Talelli, J. L. Tajada-Herráiz, M. E. Brollo, Y. Portilla, M. P. Morales, and D. F. Barber, "Cell-promoted nanoparticle aggregation decreases nanoparticle-induced hyperthermia under an alternating magnetic field independently of nanoparticle coating, core size, and subcellular localization," *ACS Applied Materials and Interfaces*, vol. 11, no. 1, pp. 340–355, 2019.

[179] N. D. Klein, K. R. Hurley, Z. V. Feng, and C. L. Haynes, "Dark field transmission electron microscopy as a tool for identifying inorganic nanoparticles in biological matrices," *Analytical Chemistry*, vol. 87, no. 8, pp. 4356–4362, 2015.

[180] A. Toro-Cordova, M. Flores-Cruz, J. Santoyo-Salazar, E. Carrillo-Nava, R. Jurado, P. Figueroa-Rodriguez, P. Lopez-Sanchez, L. Medina, and P. Garcia-Lopez, "Liposomes loaded with cisplatin and magnetic nanoparticles: Physicochemical characterization, pharmacokinetics, and in-vitro efficacy," *Molecules*, vol. 23, p. 2272, Sep 2018.

[181] A. Casadó, M. Mora, M. L. Sagristá, S. Rello-Varona, P. Acedo, J. C. Stockert, M. Cañete, and A. Villanueva, "Improved selectivity and cytotoxic effects of irinotecan via liposomal delivery: A comparative study on hs68 and hela cells," *European Journal of Pharmaceutical Sciences*, vol. 109, pp. 65–77, 2017.

[182] M. Przybylo, D. Glogocka, J. W. Dobrucki, K. Fraczkowska, H. Podbielska, M. Kopaczynska, T. Borowik, and M. Langner, "The cellular internalization of liposome encapsulated protoporphyrin ix by hela cells," *European Journal of Pharmaceutical Sciences*, vol. 85, pp. 39–46, 2016.

[183] R. Ruiz-González, P. Milán, R. Bresolí-Obach, J. C. Stockert, A. Villanueva, M. Cañete, and S. Nonell1, "Photodynamic synergistic effect of pheophorbide a and doxorubicin in combined treatment against tumoral cells," *Cancers*, 2017.

[184] Y. Liu, Z. Chen, and J. Wang, "Systematic evaluation of biocompatibility of magnetic fe3o4 nanoparticles with six different mammalian cell lines," *Journal of Nanoparticle Research*, vol. 13, no. 1, pp. 199–212, 2011.

[185] F. Sonvico, S. Mornet, S. Vasseur, C. Dubernet, D. Jaillard, J. Degrouard, J. Hoebeke, E. Duguet, P. Colombo, and P. Couvreur, "Folate-conjugated iron oxide nanoparticles for solid tumor targeting as potential specific magnetic hyperthermia mediators: Synthesis, physicochemical characterization, and in vitro experiments," *Bioconjugate Chemistry*, vol. 16, no. 5, pp. 1181–1188, 2005.

[186] M. Calero, L. Gutiérrez, G. Salas, Y. Luengo, A. Lázaro, P. Acedo, M. P. Morales, R. Miranda, and A. Villanueva, "Efficient and safe internalization of magnetic iron oxide nanoparticles: Two fundamental requirements for biomedical applications," *Nanomedicine: Nanotechnology, Biology and Medicine*, vol. 10, no. 4, pp. 733–743, 2014.

[187] G. D. Bothun, A. Lelis, Y. Chen, K. Scully, L. E. Anderson, and M. A. Stoner, "Multicomponent folate-targeted magnetoliposomes: design, characterization, and cellular uptake,"

Nanomedicine: Nanotechnology, Biology and Medicine, vol. 7, no. 6, pp. 797–805, 2011.

[188] Q. L. Vuong, J.-F. Berret, J. Fresnais, Y. Gossuin, and O. Sandre, "A universal scaling law to predict the efficiency of magnetic nanoparticles as mri t2-contrast agents," *Advanced Healthcare Materials*, vol. 1, no. 4, pp. 502–512, 2012.

[189] J.-t. Jang, H. Nah, J.-H. Lee, S. Moon, M. Kim, and J. Cheon, "Critical enhancements of mri contrast and hyperthermic effects by dopant-controlled magnetic nanoparticles," *Angewandte Chemie International Edition*, vol. 48, no. 7, pp. 1234–1238, 2009.

[190] Y.-X. J. Wang, "Superparamagnetic iron oxide based mri contrast agents: Current status of clinical application," *Quantitative Imaging in Medicine and Surgery*, vol. 1, no. 1, 2011.

[191] A. Merbach, L. Helm, and Éva Tóth, "The chemistry of contrast agents in medical magnetic resonance imaging," *John Wiley and Sons, Ltd*, 2013.

[192] D. Yoo, J.-H. Lee, T.-H. Shin, and J. Cheon, "Theranostic magnetic nanoparticles," *Accounts of Chemical Research*, vol. 44, no. 10, pp. 863–874, 2011.

[193] J. Qin, S. Laurent, Y. Jo, A. Roch, M. Mikhaylova, Z. Bhujwalla, R. Müller, and M. Muhammed, "A high-performance magnetic resonance imaging t2 contrast agent," *Advanced Materials*, vol. 19, pp. 1874–1878, 7 2007.

[194] S. Cheong, P. Ferguson, K. W. Feindel, I. F. Hermans, P. T. Callaghan, C. Meyer, A. Slocombe, C.-H. Su, F.-Y. Cheng, C.-S. Yeh, B. Ingham, M. F. Toney, and R. D. Tilley, "Simple synthesis and functionalization of iron nanoparticles for magnetic resonance imaging," *Angewandte Chemie International Edition*, vol. 50, no. 18, pp. 4206–4209, 2011.

[195] A. Skouras, S. Mourtas, E. Markoutsa, M.-C. D. Goltstein, C. Wallon, S. Catoen, and S. G. Antimisiaris, "Magnetolipo-

somes with high uspio entrapping efficiency, stability and magnetic properties," *Nanomedicine: Nanotechnology, Biology and Medicine*, vol. 7, no. 5, pp. 572–579, 2011.

[196] L. Deng, X. Ke, Z. He, D. Yang, H. Gong, Y. Zhang, X. Jing, J. Yao, and J. Chen, "A msln-targeted multifunctional nanoimmunoliposome for mri and targeting therapy in pancreatic cancer," *International journal of nanomedicine*, vol. 7, p. 5053—5065, 2012.

[197] S. German, N. Navolokin, N. Kuznetsova, V. Zuev, O. Inozemtseva, A. Anis'kov, E. Volkova, A. Bucharskaya, G. Maslyakova, R. Fakhrullin, G. Terentyuk, E. Vodovozova, and D. Gorin, "Liposomes loaded with hydrophilic magnetite nanoparticles: Preparation and application as contrast agents for magnetic resonance imaging," *Colloids and Surfaces B: Biointerfaces*, vol. 135, pp. 109–115, 2015.

[198] H. B. Na, I. C. Song, and T. Hyeon, "Inorganic nanoparticles for mri contrast agents," *Advanced Materials*, vol. 21, no. 21, pp. 2133–2148, 2009.

[199] L. Zhu, D. Wang, X. Wei, X. Zhu, J. Li, C. Tu, Y. Su, J. Wu, B. Zhu, and D. Yan, "Multifunctional ph-sensitive superparamagnetic iron-oxide nanocomposites for targeted drug delivery and mr imaging," *Journal of Controlled Release*, vol. 169, no. 3, pp. 228–238, 2013. Second Symposium on Innovative Polymers for Controlled Delivery (SIPCD 2012).

[200] E. C. Abenojar, S. Wickramasinghe, J. Bas-Concepcion, and A. C. S. Samia, "Structural effects on the magnetic hyperthermia properties of iron oxide nanoparticles," *Progress in Natural Science: Materials International*, vol. 26, no. 5, pp. 440–448, 2016. Special Issue for Nano Materials.

[201] J.-P. Fortin, C. Wilhelm, J. Servais, C. Ménager, J.-C. Bacri, and F. Gazeau, "Size-sorted anionic iron oxide nanomagnets as colloidal mediators for magnetic hyperthermia," *Journal of the American Chemical Society*, vol. 129, no. 9, pp. 2628–2635, 2007.

[202] R. Müller, R. Hergt, M. Zeisberger, and W. Gawalek, "Preparation of magnetic nanoparticles with large specific loss power for heating applications," *Journal of Magnetism and Magnetic Materials*, vol. 289, pp. 13–16, 2005. Proceedings of the 10th International Conference on Magnetic Fluids.

[203] A. Jordan, R. Scholz, P. Wust, H. Schirra, T. Schiestel, H. Schmidt, and R. Felix, "Endocytosis of dextran and silan-coated magnetite nanoparticles and the effect of intracellular hyperthermia on human mammary carcinoma cells in vitro," *Journal of Magnetism and Magnetic Materials*, vol. 194, no. 1, pp. 185–196, 1999.

[204] S. Kossatz, J. Grandke, P. Couleaud, A. Latorre, A. Aires, K. Crosbie-Staunton, R. Ludwig, H. Dähring, V. Ettelt, A. Lazaro-Carrillo, M. Calero, M. Sader, J. Courty, Y. Volkov, A. Prina-Mello, A. Villanueva, l. Somoza, A. L. Cortajarena, R. Miranda, and I. Hilger, "Efficient treatment of breast cancer xenografts with multifunctionalized iron oxide nanoparticles combining magnetic hyperthermia and anti-cancer drug delivery," *Breast Cancer Research*, vol. 17, no. 1, p. 66, 2015.

[205] R. Hergt, R. Hiergeist, M. Zeisberger, D. Schüler, U. Heyen, I. Hilger, and W. A. Kaiser, "Magnetic properties of bacterial magnetosomes as potential diagnostic and therapeutic tools," *Journal of Magnetism and Magnetic Materials*, vol. 293, no. 1, pp. 80–86, 2005. Proceedings of the Fifth International Conference on Scientific and Clinical Apllications of Magnetic Carriers.

[206] J. Carrey, B. Mehdaoui, and M. Respaud, "Simple models for dynamic hysteresis loop calculations of magnetic single-domain nanoparticles: Application to magnetic hyperthermia optimization," *Journal of Applied Physics*, vol. 109, no. 8, p. 083921, 2011.

[207] B. Mehdaoui, A. Meffre, J. Carrey, S. Lachaize, L.-M. Lacroix, M. Gougeon, B. Chaudret, and M. Respaud, "Optimal size of nanoparticles for magnetic hyperthermia: A combined theoretical and experimental study," *Advanced Functional Materials*, vol. 21, no. 23, pp. 4573–4581, 2011.

[208] M. Suto, Y. Hirota, H. Mamiya, A. Fujita, R. Kasuya, K. Tohji, and B. Jeyadevan, "Heat dissipation mechanism of magnetite nanoparticles in magnetic fluid hyperthermia," *Journal of Magnetism and Magnetic Materials*, vol. 321, no. 10, pp. 1493–1496, 2009. Proceedings of the Seventh International Conference on the Scientific and Clinical Applications of Magnetic Carriers.

[209] Y. Zheng, C. Tong, B. Wang, Y. Xie, H. Liao, D. Li, and X. Liu, "Development and application of tumor-targeting magnetic nanoparticles fa-stnp@fe2o3 for hyperthermia," *Chinese Science Bulletin*, vol. 54, no. 17, pp. 2998–3004, 2009.

[210] Z. Yang, K. Xu, B. Zhang, B. Xu, X. Zhang, and C. K. Chang, "Photosensitizer decorated iron oxide nanoparticles: bimodal agent for combined hyperthermia and photodynamic therapy," *Proc.SPIE*, vol. 6139, p. 6139, 2006.

[211] L. Asín, G. F. Goya, A. Tres, and M. R. Ibarra, "Induced cell toxicity originates dendritic cell death following magnetic hyperthermia treatment," *Cell Death and Disease*, 2013.

[212] M. Creixell, A. C. Bohórquez, M. Torres-Lugo, and C. Rinaldi, "Egfr-targeted magnetic nanoparticle heaters kill cancer cells without a perceptible temperature rise," *ACS Nano*, vol. 5, no. 9, pp. 7124–7129, 2011.

[213] A. Villanueva, P. de la Presa, J. M. Alonso, T. Rueda, A. Martínez, P. Crespo, M. P. Morales, M. A. Gonzalez-Fernandez, J. Valdés, and G. Rivero, "Hyperthermia hela cell treatment with silica-coated manganese oxide nanoparticles," *The Journal of Physical Chemistry C*, vol. 114, no. 5, pp. 1976–1981, 2010.

[214] Y. Chen, Y. Chen, D. Xiao, A. Bose, R. Deng, and G. D. Bothun, "Low-dose chemotherapy of hepatocellular carcinoma through triggered-release from bilayer-decorated magnetoliposomes," *Colloids and Surfaces B: Biointerfaces*, vol. 116, pp. 452–458, 2014.

[215] A. M. Smondyrev and M. L. Berkowitz, "Structure of dipalmitoylphosphatidylcholine/cholesterol bilayer at low and high

cholesterol concentrations: Molecular dynamics simulation," *Biophysical Journal*, 1999.

[216] C. A. Quinto, P. Mohindra, S. Tong, and G. Bao, "Multifunctional superparamagnetic iron oxide nanoparticles for combined chemotherapy and hyperthermia cancer treatment," *Nanoscale*, vol. 7, pp. 12728–12736, 2015.

[217] D. Qiu and X. An, "Controllable release from magnetoliposomes by magnetic stimulation and thermal stimulation," *Colloids and Surfaces B: Biointerfaces*, vol. 104, pp. 326–329, 2013.

[218] M.-R. Toh and G. N. Chiu, "Liposomes as sterile preparations and limitations of sterilisation techniques in liposomal manufacturing," *Asian Journal of Pharmaceutical Sciences*, vol. 8, no. 2, pp. 88–95, 2013. Special issue on Liposomes.

[219] A. S. Arbab, L. A. Bashaw, B. R. Miller, E. K. Jordan, B. K. Lewis, H. Kalish, and J. A. Frank, "Characterization of biophysical and metabolic properties of cells labeled with superparamagnetic iron oxide nanoparticles and transfection agent for cellular mr imaging," *Radiology*, vol. 229, no. 3, pp. 838–846, 2003.

[220] T. Sadhukha, L. Niu, T. S. Wiedmann, and J. Panyam, "Effective elimination of cancer stem cells by magnetic hyperthermia," *Molecular Pharmaceutics*, vol. 10, no. 4, pp. 1432–1441, 2013.